Journal of Nanomaterials

Nanomaterials for Biotechnology: Synthesis, Properties, and Applications

Lead Guest Editor: Jakub Zdarta
Guest Editors: Teofil Jesionowski and Manuel Pinelo

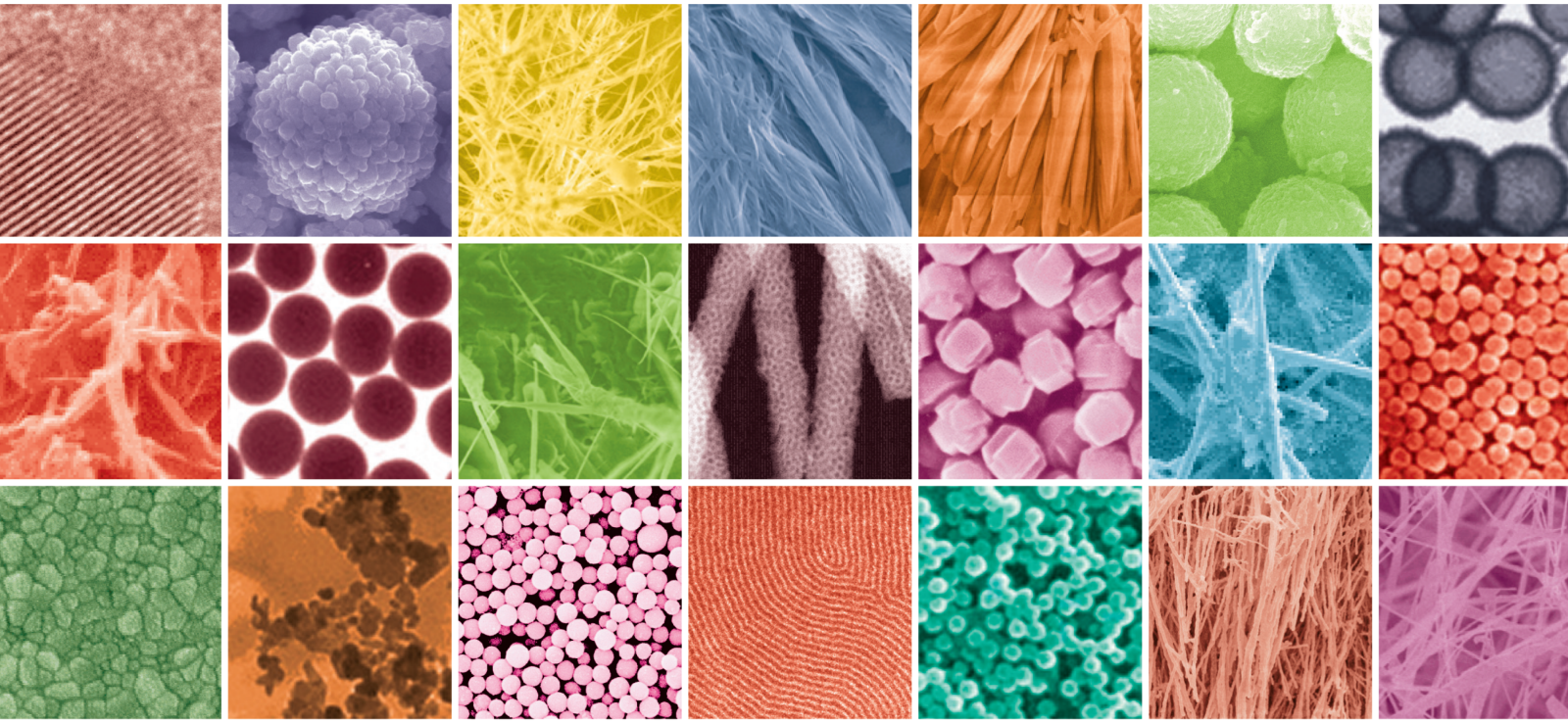

Nanomaterials for Biotechnology: Synthesis, Properties, and Applications

Journal of Nanomaterials

Nanomaterials for Biotechnology: Synthesis, Properties, and Applications

Lead Guest Editor: Jakub Zdarta
Guest Editors: Teofil Jesionowski and Manuel Pinelo

Contents

Hindawi
Journal of Nanomaterials
Volume 2019, Article ID 2464010, 10 pages
https://doi.org/10.1155/2019/2464010

Research Article

A Simple and Reliable Synthesis of Superparamagnetic Magnetite Nanoparticles by Thermal Decomposition of $Fe(acac)_3$

C. Toyos-Rodríguez,[1,2] J. Calleja-García,[1] L. Torres-Sánchez,[1,2] A. López,[1] Ahmed M. Abu-Dief,[3] A. Costa,[4] L. Elbaile,[2] R. D. Crespo,[2] J. S. Garitaonandia,[5] E. Lastra,[1] J. A. García,[2] and F. J. García-Alonso[1]

[1]*Departamento de Química Orgánica e Inorgánica, c/ Julián Clavería, 8, 33006 Oviedo, Spain*
[2]*Departamento de Física, Universidad de Oviedo, c/ Calvo Sotelo s/n, 33007 Oviedo, Spain*
[3]*Chemistry Department, Faculty of Science, Sohag University, 82524-Sohag, Egypt*
[4]*Departamento de Química Analítica y Química Física, c/ Julián Clavería, 8, 33006 Oviedo, Spain*
[5]*Fisika Aplicatua II Saila, Euskal Erriko Universitatea, Alameda Urquijo s/n 48013 Bilbao, Spain*

Correspondence should be addressed to J. A. García; joseagd@uniovi.es

Received 15 January 2019; Revised 22 July 2019; Accepted 12 October 2019; Published 13 November 2019

Academic Editor: Albert Nasibulin

Magnetic nanoparticles have been largely proposed as means of technological tools due to its value in different fields, especially in biomedicine. Herein, we present a robust, highly reproducible and low-cost method to obtain superparamagnetic magnetite nanoparticles (MNP-II) of about 15 ± 5 nm diameter by thermal decomposition of $[Fe(acac)_3]$ in a one-pot, two-step method. In the first step, magnetite nanoparticles (MNP-I) of lower size, 9 ± 4 nm, with a saturation magnetization (M_S) of 65 emu/g and a coercive field (H_c) of 1 Oe are obtained. In the second step, those particles MNP-I act as seeds for the final MNP-II which present a saturation magnetization of 70 emu/g and a coercive field of 12 Oe.

1. Introduction

Magnetic nanoparticles have been of interest and a constant subject of study since the 1970s from the scientific point of view (due to their unique electrical, magnetic, and chemical properties) and from their technological applications in different fields including catalysis [1], data storage devices [2], and environmental remediation [3]. However, the main effort in developing magnetic nanoparticles is due to their application in biomedicine to be used in biosensors, magnetic resonance imaging, drug transport, and treatment of tumors by hyperthermia [4–6].

The size of the magnetic nanoparticles is crucial in biomedicine as it affects cellular uptake, biodistribution, and other pharmacokinetic parameters.

The control of the size of the particles is also fundamental to avoid the effect of the immune system because nanoparticles with a hydrodynamic diameter lower than 5.5 nm are rapidly excreted through the kidney [7], while large nanoparticles (hydrodynamic diameter > 100 nm) are rapidly taken up by the phagocytes and tend to accumulate in the liver and spleen [8, 9]. According to the abovementioned information, the diameter of interest for particles in biomedical applications is between 20 nm and 100 nm, since these particles tend to accumulate into tumors [10, 11].

Among the different magnetic nanoparticles, iron oxide nanoparticles (IONPs) have been extensively studied due to their simple synthesis, low toxicity, affordability, stability under extreme conditions, and polar surface [12].

In addition, the magnetic properties of magnetite nanoparticles depend on their size, being superparamagnetic when they are smaller than 20 nm [13] but increasing their saturation magnetization with their radius [14]. This magnetic behavior is fundamental from the point of view of their application in medicine because if the particles were not superparamagnetic, they would continue attracting each

other after removing the external magnetic field, forming aggregates inside the organism, which would be rapidly taken up by the phagocytes [8] and in addition tend to produce embolism [15].

A large number of synthetic routes have been developed to produce IONPs of different sizes and shapes [16], with the thermal decomposition of iron complexes being one of the most widely used [17], which provides good size controllability and high crystallinity. Park et al. [18] described, in 2004, an excellent method to obtain variable amounts of IONPs of desired and uniform size by heating iron oleate in different solvents. However, the sophistication of the used heating rate device and the convenience of a more stable starting material limit its general acceptance. Due to that, the development of new procedures to prepare magnetite (Fe_3O_4) nanoparticles has been widely studied in the last decade [19, 20]. In particular, there is a permanent interest in preparing, in a simple way, MNP under 20 nm diameter (to avoid ferrimagnetic behavior) but close to this size in order to enhance their saturation magnetization. On the other hand, obtaining a reproducible, low-cost methodology that provides the same results as more expensive ones is desirable.

Benzyl ether has been widely used as solvent for the synthesis of iron oxide nanoparticles starting from iron (III) acetylacetonate using three [21, 22], two [23, 24], or one extra additive [25, 26]. Oleylamine and oleic acid have been proved as good surfactants, with the ratio of oleylamine/oleic acid being an important factor in determining both the size and the shape of the MNP [24].

A robust, one-pot, two-step method is presented here to obtain magnetite nanoparticles, MNP-II, of about 15 ± 5 nm diameter, heating $Fe(acac)_3$ in benzyl ether in the presence of oleic acid and oleylamine by using a noncomplex heating equipment. Moreover, at the end of the first step, that is, after refluxing the initial mixture for 15 minutes, smaller magnetic nanoparticles, MNP-I, of about 9 ± 4 nm diameter with a M_S of 65 emu/g are formed. They could be isolated or eventually be converted into seeds [27] for the final product, if the flask is cooled down to room temperature and then refluxed for two additional hours.

2. Materials and Methods

2.1. Materials. Benzyl ether ($C_{14}H_{14}O$, 98%), oleic acid ($C_{18}H_{34}O_2$, 99.99%), iron (III) acetylacetonate ($C_{15}H_{21}FeO_6$, 97%), toluene (C_7H_8, 99.8%), and ethyl acetate ($C_4H_8O_2$, 99.8%) were obtained from Sigma-Aldrich; 2-propanol (C_3H_8O, 99.99%) and petroleum ether (40°-60°) were supplied by VWR chemicals while oleylamine ($C_{18}H_{37}N$, 80-90%) was purchased from Acros Organics. All the reactions were carried out under inert atmosphere of argon.

2.2. Experimental Procedure. Iron (III) acetylacetonate (1.42 g, 4.0 mmol) was dispersed in a mixture of dibenzyl ether (20 ml), oleylamine (2.8 ml, 2.27 g, 7.21 mmol), and oleic acid (2.7 ml, 2.39 g, 8.46 mmol) previously deoxygenated (bubbling Ar through the mixture for 30 minutes) in a three-necked round-bottom 250 ml flask. The suspension

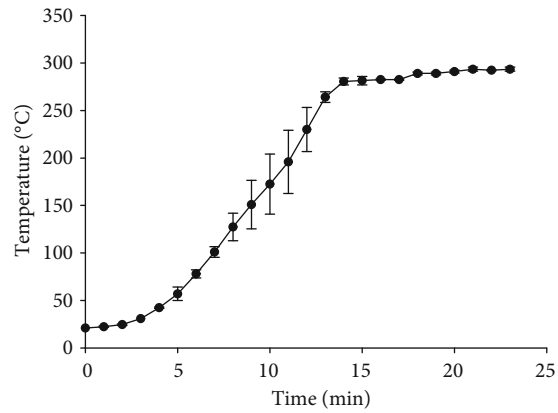

Figure 1: Temperature of the vapor condensed at the thermometer bulb placed in the third neck of the reaction flask along the reaction time.

was heated with vigorous mechanical stirring until the refluxing temperature was reached and then maintained for 15 minutes under the same conditions. Afterwards, the heating mantle was removed and the reaction temperature slowed down to room temperature. At this point, two different routes were followed to obtain two different types of MNP.

2.2.1. Procedure A: Isolation of MNP-I. While the formed black magnetite nanoparticles were retained with an external magnetic disk, the supernatant suspension was removed. Later, the nanoparticles were washed successively with a mixture 1 : 1 (in volume) of 2-propanol and light petroleum ether (4 × 20 ml) and finally dried in vacuum to give 130 mg of MNP-I (14% yield).

2.2.2. Procedure B: Preparation of MNP-II. The mixture was then refluxed for two other hours. Afterwards, the resulting black magnetite nanoparticles were isolated and purified in a similar way giving 270 mg of MNP-II (29% yield).

Both reactions have been carried out by several coauthors more than ten times along a year with comparable results. (Occasionally, the nanoparticles were slightly contaminated with silicone used in the glass stirrer gland that provides a vapor-tight seal between the paddle and the flask. The silicone was effectively eliminated washing the sample with a 2 : 1 (in volume) mixture of ethyl acetate and toluene.)

2.3. Characterization. Fourier transform infrared spectroscopic (FT-IR) measurements were performed on a FT-IR Spectrometer Paragon 1000 from PerkinElmer (USA) using KBr pressed disks.

Scanning electron microscopy images were obtained using a JEOL-6610 with an accelerating voltage of 20 kV.

Transmission electron microscopy images were obtained using either a JEOL JEM 2100F HRTEM (for MNP-I) or a JEOL-2000 EX-II TEM (for MNP-II) on a copper grid, using an accelerating voltage of 200 or 160 kV, respectively. The calculations for the size estimation were obtained with the ImageJ software, by measuring the largest dimension of each particle.

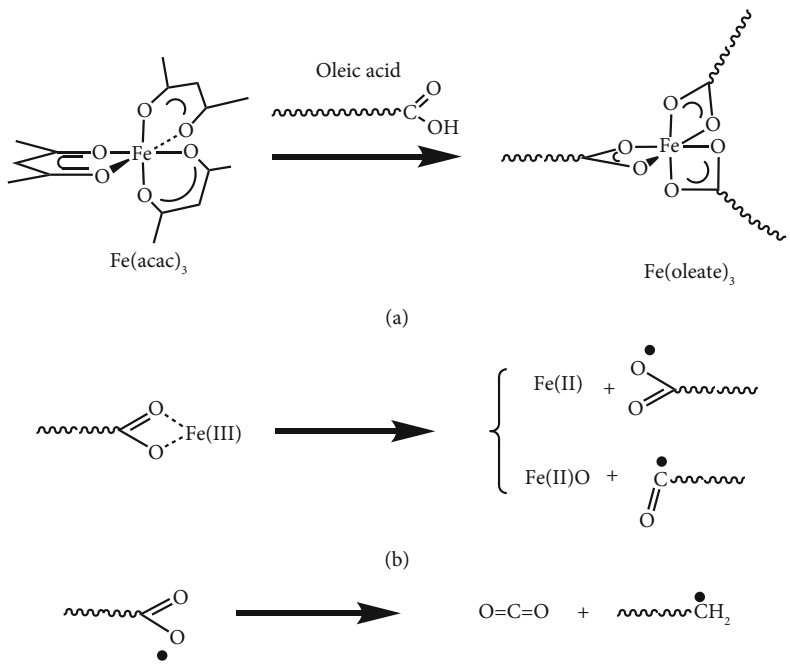

Scheme 1: Reaction mechanisms of the formation of magnetite nanoparticles using as precursors iron (III) acetylacetonate and oleic acid.

X-ray powder diffraction (XRPD) data for the two kinds of particles were collected, at RT, using CuKα1,2 radiation ($\lambda = 1.54056$ Å and 1.54439 Å) in a Bragg-Brentano reflection configuration, on an PHILIPS X' PERT PRO Panalytical diffractometer in a 2θ range of 15–90°, with a step size of 0.03. In order to obtain the instrumental broadening contribution and deconvolution, the line profile function, pure iron (II; III) oxide (Puratronic®) with high crystallinity, has been used as external reference.

Magnetization measurements at room temperature and zero-field-cooled and field-cooled were performed using a PPMS-14T (Physical Property Measurement System). This system allows applying magnetic fields to the samples up to 14 T, by using superconducting coils, at a range of temperatures from 1.9 K to 400 K.

Mössbauer spectroscopy measurements were carried out in transmission geometry using a conventional constant-acceleration spectrometer with 57Co-Rh source. Spectra were collected at different temperatures under high vacuum (10−5 torr) in a commercial Oxford Instruments cryostat. The isomer shift values were taken with respect to an α-Fe calibration foil measured at room temperature. NORMOS program was used for fitting the spectra.

3. Results and Discussion

3.1. Structural Characterization. Decomposition of iron (III) acetylacetonate in boiling benzyl ether under argon atmosphere in the presence of oleic acid and oleylamine provides two types of black superparamagnetic nanoparticles of magnetite MNP-I and MNP-II, depending on the reaction conditions.

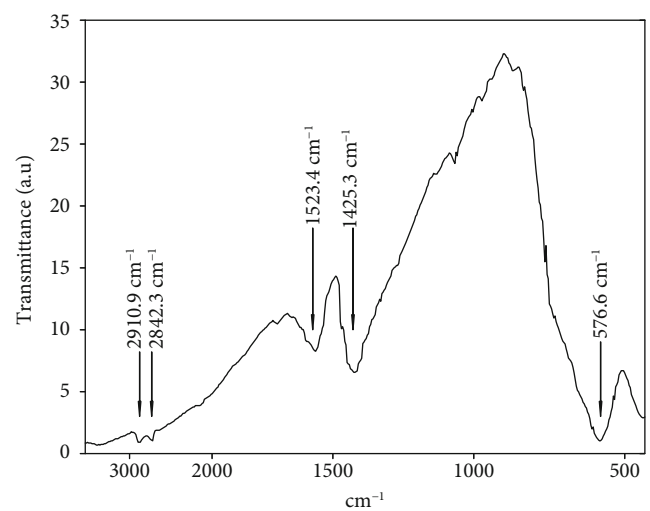

Figure 2: Infrared spectrum of the magnetic nanoparticles of step 1 (MNP-I).

The control of the heating rate seems to be of paramount importance for determining the size of the iron oxide nanoparticles [28]. In our case, the heating rate of the reaction was followed indirectly by the temperature variations of the vapor condensed in the thermometer bulb placed in the third neck of the flask (the other two were occupied by the reflux condenser and the stirring paddle). The resulting curve, shown in Figure 1, is markedly reproducible for all the reactions we have monitored.

The size mechanism control of the heating-up method should be regulated by two processes. The first is the "burst nucleation" when a great number of nuclei are formed. Although after the burst nucleation some particles are greater

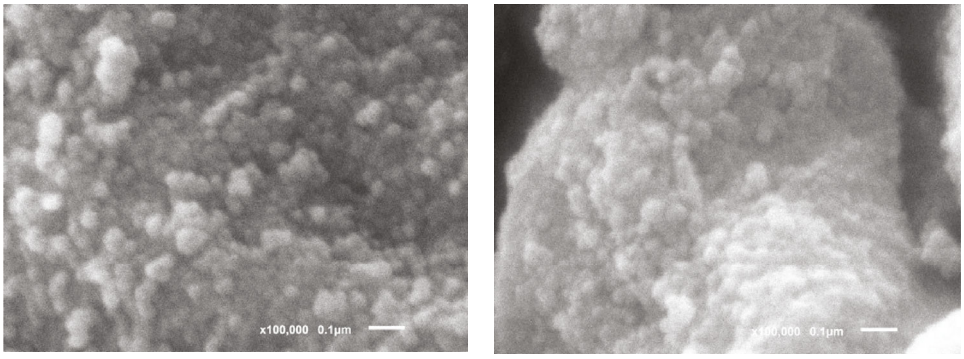

(a) (b)

Figure 3: SEM images of the nanoparticles: (a) MNP-I and (b) MNP-II.

than others, it is not of special concern as in the second process, the "size focusing," small particles grow faster than big particles [29], reaching all the same size.

The first observed stage in the heating ramp is detected at about 117°C, and it is accompanied by the appearance of a white cloud. The existence of this white cloud has been related to the presence of water vapor. Water should be released during the ketonization of oleic acid at elevated temperatures [30]. The second stage is located around 220°C and could be associated to the formation of the magnetite nucleus [31]. The formation of magnetite starting from $Fe(acac)_3$ could follow the currently accepted mechanism. Initially, the acetylacetonate ligand should be replaced by the oleate group (A in Scheme 1) [31]; then, the decomposition of iron oleate would result in the breakage of M-O and MO-C bonds of metal carboxylate and the partial reduction to Fe(II) (B in Scheme 1) [32] and the subsequent decarboxylation and formation of organic radicals (C in Scheme1) [30].

The infrared spectra of MNP-I and MNP-II are the same. Figure 2shows the infrared spectrum of MNP-I. The characteristic absorption bands of the oleate coating are at 2911 cm^{-1}, w, and 2842 cm^{-1}, w (stretching CH), and at 1523 cm^{-1}, w, br, and 1425 cm^{-1}, m, br (antisymmetric and symmetric stretching of the carboxylate group) [33]. The band at 1425 cm^{-1} should also include some contribution of the CH_2 deformation absorption. Besides, there exists another strong, broad band at 577 cm^{-1}, due to magnetite solid-state vibrations. (The occasional presence of small amounts of silicone is detected by the apparition of its characteristic bands at 1258, 1092, 1018, and 797 cm^{-1}.)

The morphology and size distribution of the nanoparticles have been obtained by SEM and TEM. SEM images of the nanoparticles are shown in Figure 3. They give an overall view on a wide area which allows to see that no large particles have been produced [34]. The particles showed a high degree of agglomeration due to dipole-dipole interaction [35].

The diameter of nanoparticles determined by TEM is 9 ± 4 nmfor MNP-I and 15 ± 5 nm for MNP-II. In Figure 4, a micrograph as well as the size distribution of both kinds of nanoparticles is shown.

The X-ray diffraction pattern of MNP-I and MNP-II shows the characteristic diffraction peaks of the magnetite (see Figure 5) with the samples not being totally crystalline as an initial elevation of the patterns was registered. The 2θ diffraction angles and the lattice spacing d (Å) of our sample are collected in Table 1. For comparative purposes, the standard atomic spacing for Fe_3O_4 are also included as well as the respective *hkl* indexes [26, 27].

The estimation of the crystalline size of magnetic nanoparticles has been carried out by using the FullProf program [36]. The effect of instrumental peak broadening was corrected by performing a Le Bail fitting method [37]. During the Le Bail fitting for each sample, instrumental parameters U, V, and W were kept constant, as well as the asymmetric parameters (SL and DL). The Thompson-Cox-Hastings pseudo-Voigt profile function expressed by a weighted sum of Gaussian and Lorentzian was applied to obtain the average apparent crystalline size directly [38]. From this estimation, an average apparent size (Figure 6) of 8 ± 3 nm and 12 ± 2 nm from MNP-I and MNP-II, respectively, is obtained. These results show that the crystallite and nanoparticle sizes are the same, indicating that both kinds of particles are monocrystallines.

3.2. Magnetic Characterization. The room temperature hysteresis loops of the particles obtained in the first step and in the second one step are shown in Figure 7. The magnetic behavior of the particles of the first step differs slightly from that observed in the final particles. The particles of the first step present superparamagnetic behavior with a coercive field of about 1 Oe at room temperature, and they also have a high saturation magnetization of about 65 emu/g. In the case of the final particles, the superparamagnetic behavior is slightly different. The coercive field has increased to a value of about 12 Oe; nevertheless, they are within the limits accepted as superparamagnetic. Also, it can be observed that there is an increase of the saturation magnetization, which in this case results in about 70 emu/g, lower than that of the bulk magnetite (92 emu/g). This decrease is not clear and is still the object of research. Now, different studies attribute this decrease to the surface spin canting [39, 40]. The saturation magnetization of both kinds of particles is really a high value and makes them very promising for their coating and subsequent use.

Magnetization curves of zero-field-cooled (ZFC) and field-cooled (FC) were measured in the temperature range

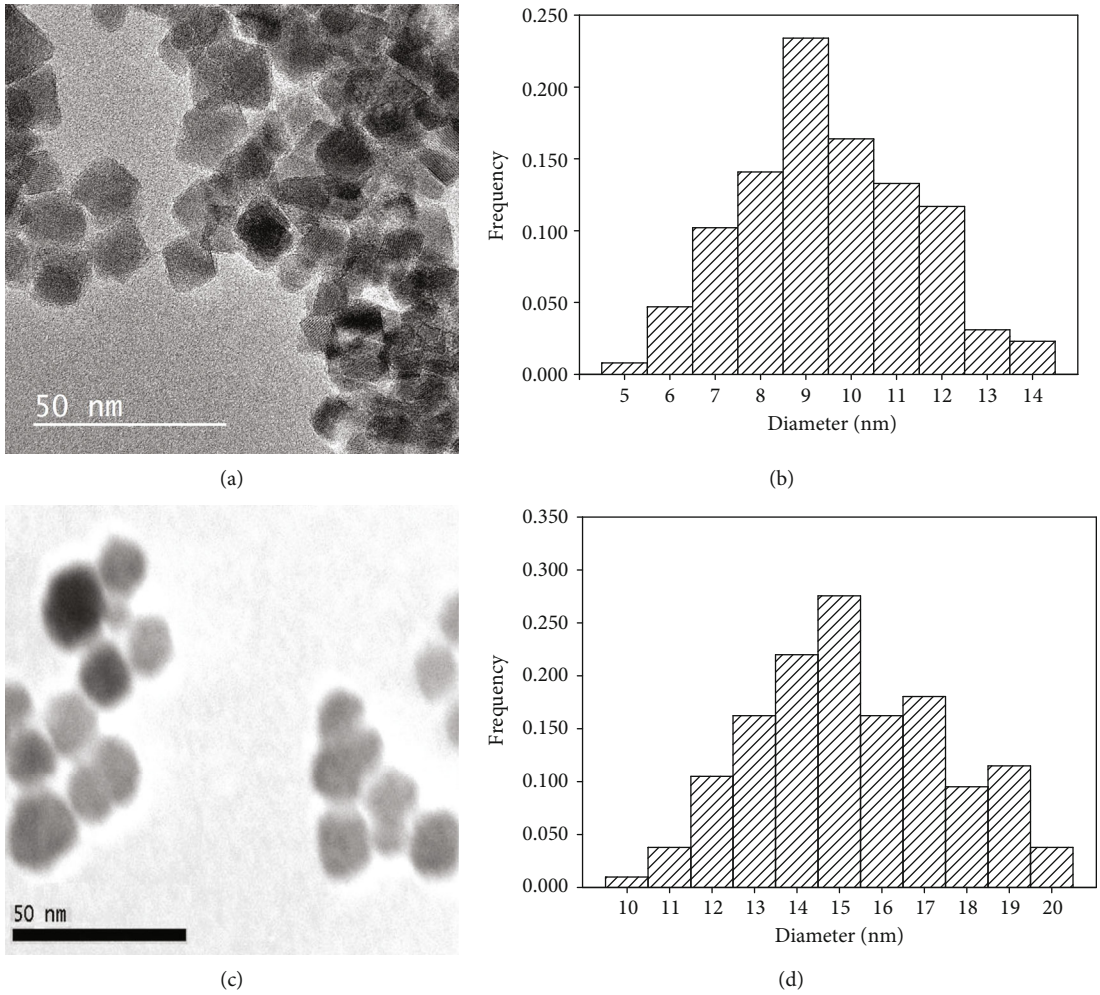

Figure 4: Representative TEM images (a, c) and size distribution (b, d) for MNP-I and MNP-II, respectively.

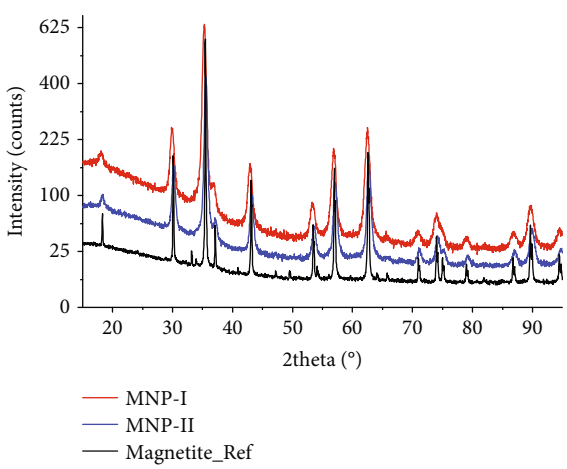

Figure 5: X-ray diffraction (XRD) pattern of MNP-I (red), MNP-II (blue), and reference magnetite (black).

from 5 K to 315 K. The samples were mounted in the PPMS at room temperature and cooled down to 5 K without applied field. After cooling, a dc field of 100 Oe was applied and the temperature was increased to 315 K.

The magnetic behavior of the two kinds of nanoparticles (Figure 8) differs slightly. MNP-I particles show a superparamagnetic behavior at room temperature with a coercive field minor than 1 Oe and saturation magnetization of 65 emu/g. The MNP-II particles present a coercive field of 12 Oe, a saturation magnetization of 70 emu/g, and a $T_B > 300$ K. On the other hand, the two kinds of nanoparticles show a Verwey transition at about 120 K. This anomalous behavior shown in the obtained curves has been studied by Bohra et al. [41], and it was explained by the nonspherical morphology of the samples.

Figure 9 shows the Mössbauer spectra of the studied samples obtained at different temperatures. For a better comparison, all the spectra are normalized to present the same area. The thermal evolution of the spectra strongly depends on the size of the MNPs.

The formal composition of magnetite can be written as $[Fe^{3+}]_A[Fe^{2+}Fe^{3+}]_BO^{2-}{}_4$, where A denotes Fe sites surrounded by oxygen ions forming tetrahedral and B corresponds to the Fe ions inside octahedral formed by the nearest oxygen ions. This structure is clearly reflected in the Mössbauer spectra obtained at 295 K and 150 K. The spectra have been fitted by two sextets presenting hyperfine parameters and a 1 : 2

Table 1: Experimental 2θ values and lattice spacing of MNP-I and MNP-II; Standard lattice spacing and corresponding plane assignation of Fe_3O_4.

MNP-I	2θ (°)	17.6	30.0	35.4	37.0	43.2	53.7	57.1	62.6	71.2	73.9	79.3
	d (Å)	5.04	2.98	2.54	2.43	2.09	1.72	1.61	1.48	1.32	1.28	1.21
MNP-II	2θ (°)	18.3	30.2	35.5	37.1	43.2	53.5	57.1	62.7	71.1	74.2	79.2
	d (Å)	4.84	2.96	2.52	2.42	2.09	1.71	1.61	1.48	1.32	1.28	1.21
Standard values	Fe_3O_4	4.86	2.98	2.53	2.43	2.10	1.71	1.62	1.48	1.33	1.28	1.21
	hkl	111	220	311	222	400	422	511	440	620	533	444

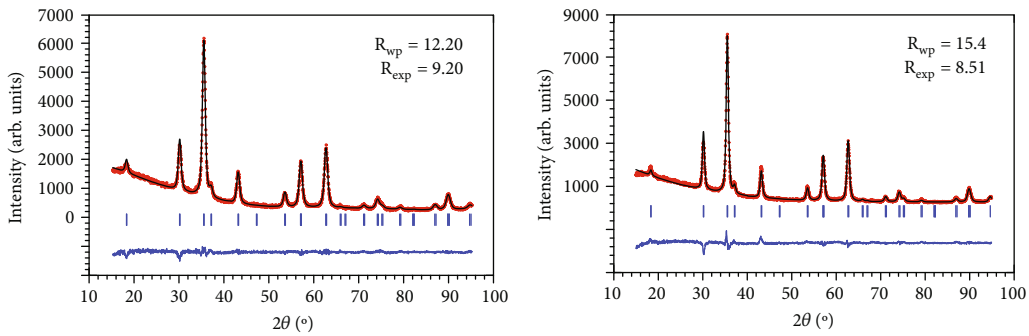

Figure 6: Le Bail fitting (black line) and experimental data (red points) collected from MNP-I (a) and MNP-II (b).

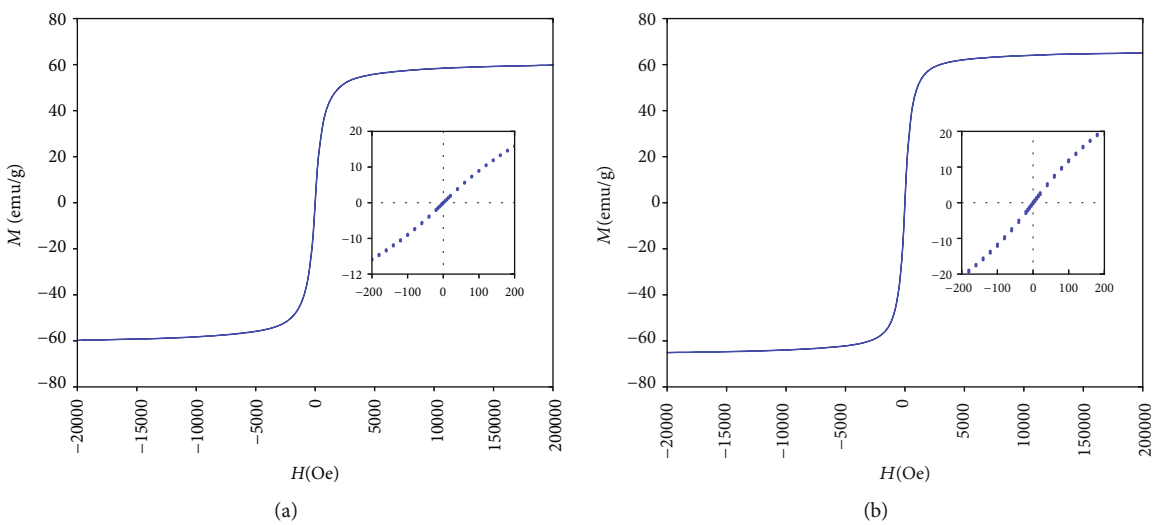

Figure 7: Magnetic hysteresis loops of the particles measured at room temperature: (a) first step and (b) second step. In the inset, an amplification of the low-field region of the hysteresis loops is shown.

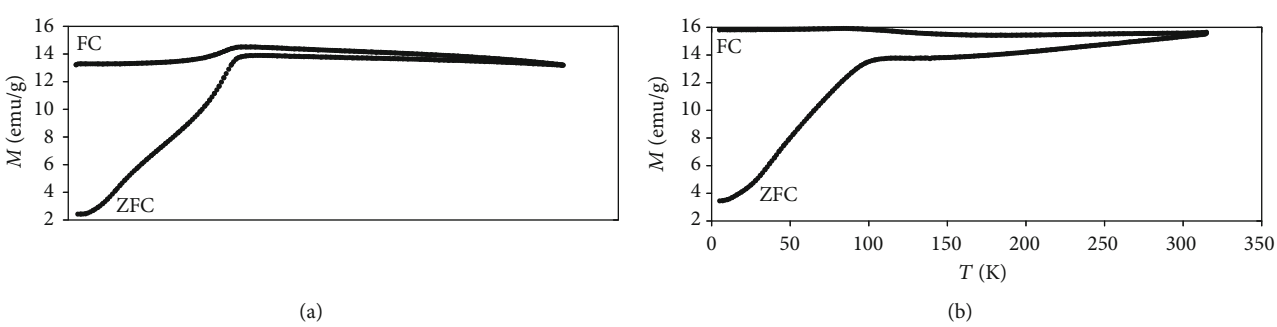

Figure 8: Results of the ZFC and FC magnetization measurements for the samples at an applied field of 100 Oe: (a) NPM-I and (b) NPM-II.

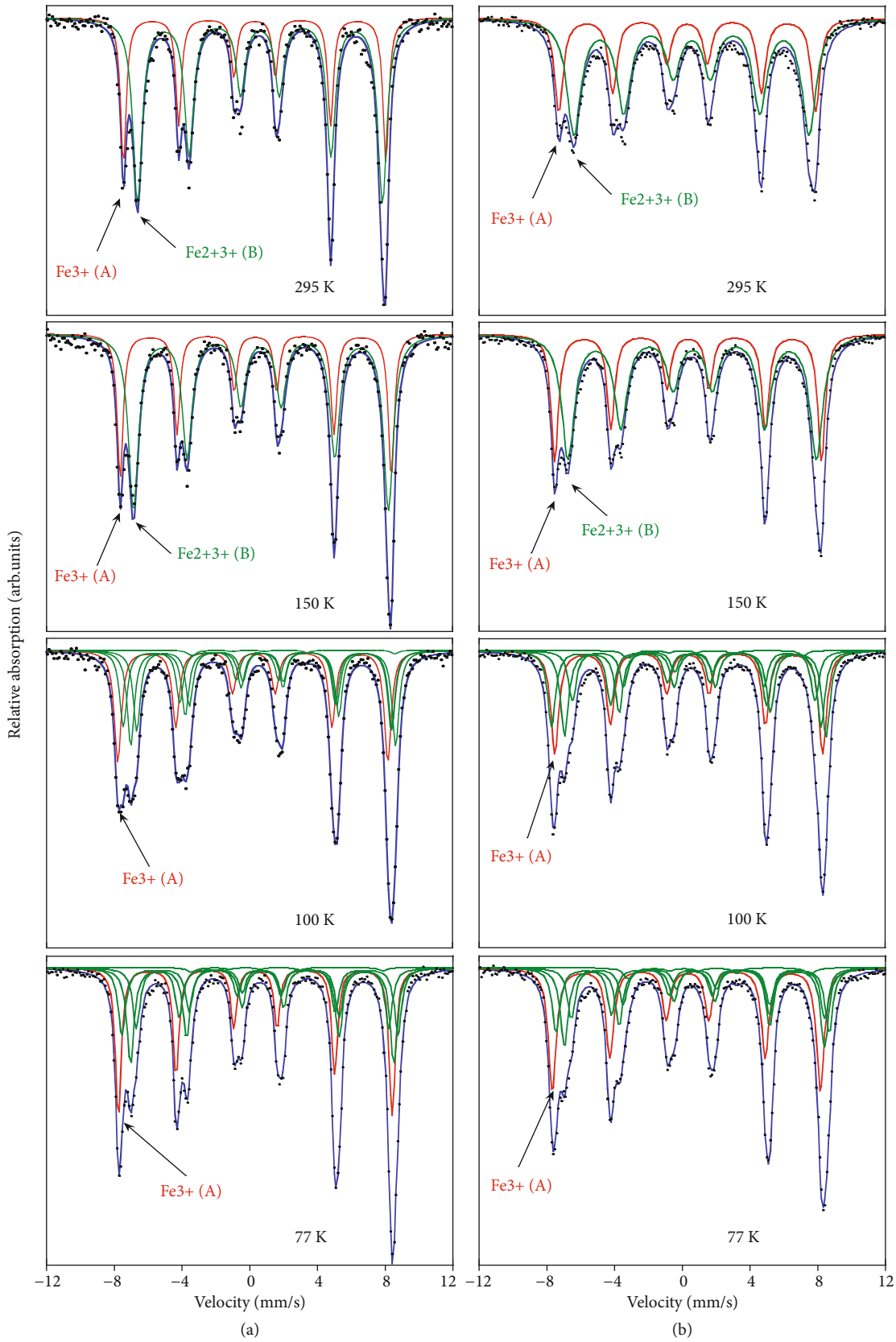

Figure 9: Mössbauer spectra of (a) MNP-I nanoparticles and (b) MNP-II nanoparticles.

Table 2: Isomer shift (IS), quadrupolar splitting (QS), hyperfine field (B_{hf}), and full width at half maximum (WID) values obtained from the fittings of the Mossbauer spectra of the study samples. %Fe denotes the obtained ratio of the resonant areas among Fe^{3+} A sites and the $Fe^{2+/3+}$ B sites of the magnetite.

(a)

T (K)	Position	IS (mm/s)*	MNP-I QS (mm/s)	B_{hf} (T)	WID (mm/s)	%Fe
295	Magnetite Fe^{3+} (A)	0.32 (1)	0.00 (1)	47.0 (1)	0.61 (1)	34 (1)
	Magnetite $Fe^{2+}Fe^{3+}$ (B)	0.59 (1)	-0.02 (1)	43.1 (1)	1.00 (1)	66 (1)
150	Magnetite Fe^{3+} (A)	0.38 (1)	0.00 (1)	48.9 (2)	0.53 (1)	37 (1)
	Magnetite $Fe^{2+}Fe^{3+}$ (B)	0.64 (1)	-0.03 (1)	45.5 (1)	0.90 (1)	63 (1)

(b)

T (K)	Position	IS (mm/s)*	MNP-II QS (mm/s)	B_{hf} (T)	WID (mm/s)	%Fe
295	Magnetite Fe^{3+} (A)	0.30 (1)	0.00 (3)	48.1 (1)	0.41 (1)	34 (1)
	Magnetite $Fe^{2+}Fe^{3+}$ (B)	0.62 (1)	-0.01 (1)	44.9 (1)	0.65 (1)	66 (1)
150	Magnetite Fe^{3+} (A)	0.37 (1)	0.02 (1)	49.7 (1)	0.43 (1)	33 (1)
	Magnetite $Fe^{2+}Fe^{3+}$ (B)	0.69 (1)	0.00 (1)	46.7 (1)	0.70 (1)	67 (1)

resonant area ratio compatible, respectively, to the Fe^{3+} A sites and the $Fe^{2+/3+}$ B sites of the inverse spinel structure of the magnetite above the Verwey transition (T_V). Hyperfine parameters obtained from the fittings can be consulted in Table 2. The spectrum of the MNP-I collected at 295 K is considerably wider, and the hyperfine fields are significantly lower than those corresponding to the MNP-II. This variance is indicative that the MNP-I is close to a superparamagnetic state at room temperature.

In a stoichiometric bulk magnetite, the Verwey phase transition takes place at around 120 K and the inverse cubic (Fd3-m) spinel structure of magnetite reduces its symmetry and transforms into the monoclinic Cc structure. From 150 K, as the temperature decreases, the Mössbauer spectra of the studied samples show a slow evolution, in contrast with the expected sharp transition for a stoichiometric bulk magnetite. It has been observed that for magnetite MNPs, the Verwey phase transition can begin even at higher temperatures, extends in a broad temperature range, and is not completed down to lower temperatures [42]. At nanometric sizes, the relative increase of surface atoms with different chemical and structural topologies induces the formation of charge-ordered surface states which would include changes in the Verwey phase transition temperatures [43, 44], becoming more noticeable as the size of the MNPs lowers.

Below 150 K, the spectra cannot be properly described by a composition of only the spectral components of the stoichiometric Fe^{3+} A and $Fe^{2+/3+}$ B sites of the inverse spinel structure and more contributions would be needed for an appropriate fitting. The transition to the monoclinic structure gives rise to 24 different groups of Fe sites, 8 different groups of crystallographically equivalent A sites, and 16 different groups of crystallographically equivalent B sites. We have followed the fitting assignments described by Řezníček et al. [45] to fit the contribution of the monoclinic magnetite to the Mössbauer spectra of the studied samples. Based on DFT calculations, they get a reliable simulation of the Mössbauer spectrum with a considerable agreement with of the experimental one. Concretely, they reduce the spectrum at temperatures below T_V to four sextets: two contributions representing Fe^{3+} from A position and Fe^{3+} from B-like position, respectively, and two spectra to describe the contribution of two different sets of Fe^{2+} from B-like position. So, the fitting of the Mössbauer spectra of samples below 150 K is composed of five different contributions, those describing the Fe^{3+} A and $Fe^{2+/3+}$ B sites of the inverse spinel structure above T_V and three describing the splitting of the $Fe^{2+/3+}$ B site in different crystallographic positions at lower temperatures. The aim of the analysis of the Mössbauer spectra in this work is not reinterpreting the structure of magnetite MNPs below T_V, and the results of the fittings will not be discussed. However, the description of the thermal evolution of the Mössbauer spectra is in line with a scenario of a broad cubic to monoclinic phase transition. As the temperature decreases, the relative contribution to the spectrum of the components assigned to the monoclinic phase increases at the expenses of the sextets corresponding to the spinel structure, becoming the main one at 77 K. It must be also underlined that the ratio among the resonant areas due to the Fe^{3+} A sites and the $Fe^{2+/3+}$ B sites remains around 1 : 2 which would corroborate the stoichiometry of the magnetite for all the temperatures.

4. Conclusions

A low-cost, easy, and reproducible method to obtain iron oxide superparamagnetic nanoparticles is presented. This method does not need sophisticated equipment and so is easy to reproduce anywhere. It is a low-cost, two-step method that allows the obtaining of two kinds of nanoparticles by thermal decomposition. In the first step, superparamagnetic nanoparticles of 9 ± 4 nm with a saturation

magnetization of 65 emu/g and a coercive field of 1 Oe are obtained; meanwhile, in the second step, the obtained nanoparticles with a size of 15 ± 5 nm present a saturation magnetization of 70 emu/g and a coercive field of 12 Oe.

Data Availability

The data used to support the findings of this study are included within the article.

Conflicts of Interest

The authors declare that they have no conflicts of interest.

Acknowledgments

This work has been carried out within the project CTQ2017-86994-R of the Spanish Ministry of Economy, Industry and Competitiveness, and it was supported by the IUTA/Gijón Council under grants SV-17-Gijón-1-13 and SV-18-GIJÓN-1-14. Special acknowledgment is given to the Oviedo University Scientific and Technological Resources.

References

[1] J. Govan and Y. Gun'ko, "Recent advances in the application of magnetic nanoparticles as a support for homogeneous catalysts," *Nanomaterials*, vol. 4, no. 2, pp. 222–241, 2014.

[2] G. Reiss and A. Hutten, "Applications beyond data storage," *Nature Materials*, vol. 4, no. 10, pp. 725-726, 2005.

[3] S. Chunming, "Environmental implications and applications of engineered nanoscale magnetite and its hybrid nanocomposites: A review of recent literature," *Journal of Hazardous Materials*, vol. 322, pp. 48–84, 2017.

[4] V. F. Cardoso, A. Francesko, C. Ribeiro, M. Bañobre-López, P. Martins, and S. Lanceros-Mendez, "Advances in magnetic nanoparticles for biomedical applications," *Advanced Healthcare Materials*, vol. 7, no. 5, p. 1700845, 2018.

[5] Y. Hu, S. Mignani, J. Majoral, M. Shen, and X. Shi, "Construction of iron oxide nanoparticle-based hybrid platforms for tumor imaging and therapy," *Chemical Society Reviews*, vol. 47, no. 5, pp. 1874–1900, 2018.

[6] J. Mosayebi, M. Kiyasatfar, and S. Laurent, "Synthesis, functionalization, and design of magnetic nanoparticles for theranostic applications," *Advanced Healthcare Materials*, vol. 6, no. 23, p. 1700306, 2017.

[7] H. Choi, W. Liu, P. Misra et al., "Renal clearance of quantum dots," *Nature Biotechnology*, vol. 25, no. 10, pp. 1165–1170, 2007.

[8] A. Tanimoto and S. Kuribayashi, "Application of superparamagnetic iron oxide to imaging of hepatocellular carcinoma," *European Journal of Radiology*, vol. 58, no. 2, pp. 200–216, 2006.

[9] S. M. Moghimi, "Mechanisms of splenic clearance of blood cells and particles: towards development of new splenotropic agents," *Advanced Drug Delivery Reviews*, vol. 17, no. 1, pp. 103–115, 1995.

[10] H. Cabral, Y. Matsumoto, K. Mizuno et al., "Accumulation of sub-100 nm polymeric micelles in poorly permeable tumours depends on size," *Nature Nanotechnology*, vol. 6, no. 12, pp. 815–823, 2011.

[11] S. D. Perrault, C. Walkey, T. Jennings, H. C. Fischer, and W. C. Chan, "Mediating tumor targeting efficiency of nanoparticles through design," *Nano Letters*, vol. 9, no. 5, pp. 1909–1915, 2009.

[12] R. B. Nasir Baig, M. N. Nadagouda, and R. S. Varma, "Magnetically retrievable catalysts for asymmetric synthesis," *Coordination Chemistry Reviews*, vol. 287, pp. 137–156, 2015.

[13] L. Li, Y. Yang, J. Ding, and J. Xue, "Synthesis of magnetite nanooctahedra and their magnetic field-induced two-/three-dimensional superstructure," *Chemistry of Materials*, vol. 22, no. 10, pp. 3183–3191, 2010.

[14] W. Wu, C. Z. Jiang, and V. A. L. Roy, "Designed synthesis and surface engineering strategies of magnetic iron oxide nanoparticles for biomedical applications," *Nanoscale*, vol. 8, no. 47, pp. 19421–19474, 2016.

[15] L. Douziech-Eyrolles, H. Marchais, K. Heme et al., "Nanovectors for anticancer agents based on superparamagnetic iron oxide nanoparticles," *International Journal of Nanomedicine*, vol. 2, no. 4, pp. 541–550, 2007.

[16] S. Laurent, D. Forge, M. Port et al., "Magnetic iron oxide nanoparticles: synthesis, stabilization, vectorization, physicochemical characterizations, and biological applications," *Chemical Reviews*, vol. 108, no. 6, pp. 2064–2110, 2008.

[17] D. Ling and T. Hyeon, "Chemical design of biocompatible iron oxide nanoparticles for medical applications," *Small*, vol. 9, no. 9-10, pp. 1450–1466, 2013.

[18] J. Park, K. An, Y. Hwang et al., "Ultra-large-scale syntheses of monodisperse nanocrystals," *Nature Materials*, vol. 3, no. 12, pp. 891–895, 2004.

[19] D. Kim, N. Lee, M. Park, B. H. Kim, K. An, and T. Hyeon, "Synthesis of uniform ferrimagnetic magnetite nanocubes," *Journal of the American Chemical Society*, vol. 131, no. 2, pp. 454-455, 2009.

[20] R. K. Sharma, S. Dutta, S. Sharma, R. Zboril, R. S. Varma, and M. B. Gawande, "Fe_3O_4 (iron oxide)-supported nanocatalysts: synthesis, characterization and applications in coupling reactions," *Green Chemistry*, vol. 18, no. 11, pp. 3184–3209, 2016.

[21] W. Jiang, K. Lai, K. Liu et al., ""Green" functionalization of magnetic nanoparticles via tea polyphenol for magnetic resonance/fluorescent dual-imaging," *Nanoscale*, vol. 6, no. 3, pp. 1305–1310, 2014.

[22] S. I. C. J. Palma, M. Marciello, A. Carvalho, S. Veintemillas-Verdaguer, M. P. Morales, and A. C. A. Roque, "Effects of phase transfer ligands on monodisperse iron oxide magnetic nanoparticles," *Journal of Colloid and Interface Science*, vol. 437, pp. 147–155, 2015.

[23] N. Lee, Y. Choi, Y. Lee et al., "Water-dispersible ferrimagnetic iron oxide nanocubes with extremely high r_2 relaxivity for highly sensitive in vivo MRI of tumors," *Nano Letters*, vol. 12, no. 6, pp. 3127–3131, 2012.

[24] V. M. Lenart, S. L. Gómez, M. P. Calatayud, and G. R. F. Goya, "Size and shape control of magnetite nanoparticles with a non-selective binding surfactants," 2014, http://arxiv.org/abs/1402.1134.

[25] A. R. Deniz, Z. Çaldıran, Ö. Metin, K. Meral, and S. Aydogan, "The investigation of the electrical properties of Fe_3O_4/ _n_ -Si heterojunctions in a wide temperature range," *Journal of Colloid and Interface Science*, vol. 473, pp. 172–181, 2016.

[26] Y. Lv, Y. Yang, J. Fang et al., "Size dependent magnetic hyperthermia of octahedral Fe3O4nanoparticles," *RSC Advances*, vol. 5, no. 94, pp. 76764–76771, 2015.

[27] S. Sun, H. Zeng, D. B. Robinson et al., "Monodisperse MFe_2O_4 (M=Fe, Co, Mn) nanoparticles," *Journal of the American Chemical Society*, vol. 126, no. 1, pp. 273–279, 2004.

[28] P. Guardia, J. Pérez-Juste, A. Labarta, X. Batlle, and L. M. Liz-Marzán, "Heating rate influence on the synthesis of iron oxide nanoparticles: the case of decanoic acid," *Chemical Communications*, vol. 46, no. 33, pp. 6108–6110, 2010.

[29] T. H. de Keiiser and J. I. Langford, "Use of the Voigt function in a single-line method for the analysis of X-ray diffraction line broadening," *Journal of Applied Crystallography*, vol. 15, no. 3, pp. 308–314, 1982.

[30] S. G. Kwon and T. Hyeon, "Formation Mechanisms of Uniform Nanocrystals via Hot-Injection and Heat-Up Methods," *Small*, vol. 7, no. 19, pp. 2685–2702, 2011.

[31] S. J. Kemp, R. M. Ferguson, A. P. Khandhara, and K. M. Krishnanab, "Monodisperse magnetite nanoparticles with nearly ideal saturation magnetization," *RSC Advances*, vol. 6, no. 81, pp. 77452–77464, 2016.

[32] P. Guardia, N. Pérez, A. Labarta, and X. Batlle, "Controlled synthesis of iron oxide nanoparticles over a wide size range," *Langmuir*, vol. 26, no. 8, pp. 5843–5847, 2010.

[33] C. Fang, N. Bhattarai, C. Sun, and M. Zhang, "Functionalized nanoparticles with long-term stability in biological media," *Small*, vol. 5, no. 14, pp. 1637–1641, 2009.

[34] J. Santoyo, L. Pérez, O. De Abril et al., "Magnetic iron oxide nanoparticles in 10-40 nm range: composition in terms of magnetite/maghemite ratio and effect on the magnetic properties," *Chemistry of Materials*, vol. 23, no. 6, pp. 1379–1386, 2011.

[35] P. B. Shete, R. M. Patil, N. D. Thorat, A. Prasad, R. S. Ningthoujam, and S. J. Ghosh, "Magnetic chitosan nanocomposite for hyperthermia therapy application: preparation, characterization and in vitro experiments," *Applied Surface Science*, vol. 288, pp. 149–157, 2014.

[36] J. Rodríguez-Carvajal, "FullProf: a program from Rietveld refinement and pattern matching analysis," in *Abstract of the Satellite Meeting on Powder Diffraction of the XV Congress of the IUCr*, p. 127, Scientific Research, Toulouse, France, 1990.

[37] A. Le Bail, H. Duroy, and J. L. Fourquet, "Ab-initio structure determination of $LiSbWO_6$ by X-ray powder diffraction," *Materials Research Bulletin*, vol. 23, no. 3, pp. 447–452, 1988.

[38] S. G. Kwon, Y. Piao, J. Park et al., "Kinetics of monodisperse iron oxide nanocrystal formation by "heating-up" process," *Journal of the American Chemical Society*, vol. 129, no. 41, pp. 12571–12584, 2007.

[39] D. H. Han, J. P. Wang, Y. B. Feng, and H. L. Luo, "Influence of size and magnetocrystalline anisotropy on spin canting anomaly in fine ferrimagnetic particles," *Journal of Applied Physics*, vol. 76, no. 10, pp. 6591–6593, 1994.

[40] R. H. Kadama, "Magnetic nanoparticles," *Journal of Magnetism and Magnetic Materials*, vol. 200, no. 1-3, pp. 359–372, 1999.

[41] M. Bohra, N. Agarwal, and V. Singh, "A short review on Verwey transition in nanostructured Fe_3O_4 materials," *Journal of Nanomaterials*, vol. 2019, Article ID 8457383, 18 pages, 2019.

[42] I. Dézsi, C. S. Fetzer, Á. Gombkötő, I. Szűcs, J. Gubicza, and T. Ungár, "Phase transition in nanomagnetite," *Journal of Applied Physiology*, vol. 103, no. 10, article 104312, 2008.

[43] I. V. Shvetz, G. Mariotto, K. Jordan, N. Berdunov, R. Kantor, and S. Murphy, "Long-range charge order on theFe3O4(001)-surface," *Physical Review B*, vol. 70, no. 15, p. 155406, 2004.

[44] D. G. Mitchell, "MR imaging contrast agents — what's in a name?," *Journal of Magnetic Resonance Imaging*, vol. 7, no. 1, pp. 1–4, 1997.

[45] R. Řezníček, V. Chlan, H. Štěpánková et al., "Understanding the Mössbauer spectrum of magnetite below the Verwey transition:Ab initiocalculations, simulation, and experiment," *Physical Review B*, vol. 96, no. 19, p. 195124, 2017.

Hindawi
Journal of Nanomaterials
Volume 2019, Article ID 3835609, 9 pages
https://doi.org/10.1155/2019/3835609

Research Article

Simple Label-Free Electrochemical Immunosensor in a Microchamber for Detecting Newcastle Disease Virus

Luyen Thi Tran,[1] Thinh Quang Tran,[2] Ha Phu Ho,[3] Xuan Thi Chu,[4] and Tuan Anh Mai[2]

[1]*School of Chemical Engineering, Hanoi University of Science and Technology, No. 1 Dai Co Viet Road, Hai Ba Trung District, Hanoi, Vietnam*
[2]*Laboratory for MEMS/NEMS Technology, National Center for Technological Progress, 25 Le Thanh Tong Street, Hoan Kiem District, Hanoi, Vietnam*
[3]*School of Biotechnology and Food Technology, Hanoi University of Science and Technology, No. 1 Dai Co Viet Road, Hai Ba Trung District, Hanoi, Vietnam*
[4]*International Training Institute for Materials Science, Hanoi University of Science and Technology, No. 1 Dai Co Viet Road, Hai Ba Trung District, Hanoi, Vietnam*

Correspondence should be addressed to Tuan Anh Mai; mtuan@itims.edu.vn

Received 7 March 2019; Accepted 7 August 2019; Published 9 October 2019

Guest Editor: Jakub Zdarta

In this study, a simple, label-free, electrochemical immunosensor system, including a three-electrode transducer and a microchamber, was designed, fabricated, and integrated with focus toward the detection of Newcastle disease virus (NDV). The chicken egg yolk antibodies (IgY) against NDV were used as the biological recognition element, replacing purified IgG antibodies that require a complex extraction process and time-consuming. The IgY against NDV was immobilized on the sensor surface using PrA/GA and SAM/NHS approaches. The immunosensor showed high sensitivity with NDV concentrations ranging from 10^6 to 10^2 EID_{50}/mL with good specificity, repeatability, and small standard deviations. Compared to traditional methods, the immunosensor with advantages such as simple fabrication, quick response, direct detection, and possibility for miniaturization by integrating the immunosensor with the microchamber is potential for applications in contamination studies and field measurements.

1. Introduction

Newcastle disease (ND) is one of the most contagious diseases in poultry that has widely spread in South East Asian countries including Vietnam and causes severe economic losses [1, 2]. So far, the conventional qualitative methods such as hemagglutination inhibition (HI) [2], agar gel precipitation [3], and Latex agglutination tests [4] have been introduced for clinical diagnosis of ND. In addition, enzyme-linked immunosorbent assay (ELISA) [2], polymerase chain reaction (PCR) [5, 6], and immunofluorescence test [7] have also been used for the semiquantitative analysis. Although these methods effectively determine NDV in infective samples, they require complicated procedures for sample preparations, sophisticated instruments for assays, and large periods of time for the completion of the assays. Therefore, alternative methods that offer a simple, rapid, and cost-effective analytical strategy and possible on-site and in-field measurements are essential.

Label-free electrochemical immunosensor detects antigens using specific antibodies immobilized on a surface of metallic electrodes [8–11]. This method has been developed with rapid analysis, high sensitivity, and portability purposes [12–15]. In this work, the three-electrode setup including the integrated Au electrodes consisted of a working electrode (WE), a counter electrode (CE) in a chip, and a quasireference Ag/AgCl electrode (qRE) was designed and fabricated. The polydimethylsiloxane- (PDMS-) based microchamber was bonded with the integrated three-electrode setup to facilitate miniaturization of the analytical system, and thus, the volume of the consumed biological sample is reduced. Moreover, this structure also simplifies the microelectrode

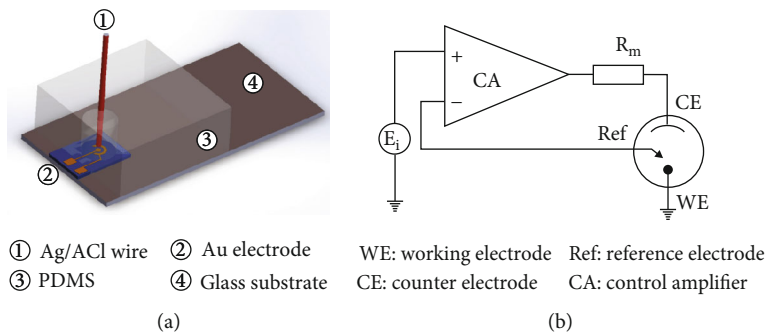

Figure 1: (a) Schematic illustration of the measuring setup and (b) equivalent circuit of the measuring system.

fabrication process in a clean room and, on the other hand, is convenient for electrical connection with a measuring circuit.

In immunosensor development, most of the studies, using monoclonal immunoglobulin G (IgG) antibody from mammalian blood as the biological recognition element, have been focused on antibody immobilization methods to improve the sensitivity, response time, and detection limit [16–18]. However, IgG antibody production and purification require modern techniques, expensive biologicals, long time, and complicated procedures [19, 20]. In our previous work [21], chicken egg yolk immunoglobulin (IgY) antibody was used as an alternative to IgG in immunosensor fabrication. The immobilization using IgY antibody offers advantages with respect to cost-effective and rapid detection of virus in infectious disease outbreaks. In addition, it is less dependent on purified IgG sources with shorter lease time and reduced costs. In this work, chicken egg yolk antibodies (IgY) against ND virus were immobilized on the Au electrodes (WE) using two different methods: (1) the combination protein A/glutaraldehyde (PrA/GA) and (2) the self-assembly modification of thioglycolic acid with the activation by *N*-succinimidyl ester (SAM/NHS). The fabricated immunosensors were used to detect ND virus. The effect of virus incubation time on the output signal of the immunosensors and specificity and sensitivity of the ND virus immunosensors was also investigated. Both immunosensors showed advantages over conventional ones such as simple process, quick response, direct detection, high specificity and sensitivity, and potential miniaturization by integrating with micro reactors.

2. Materials and Methods

2.1. Chemicals. Polydimethylsiloxane (PDMS) Sylgard 184 was obtained from Dow Corning. Staphylococcal protein A (PrA), bovine serum albumin (BSA, 98% purity), phosphate buffer solution (PBS, 0.01 M, pH 7.4), potassium hexacyanoferrate(II) trihydrate ($K_4Fe(CN)_6{\cdot}3H_2O$, 99.5% purity), potassium ferricyanide(III) ($K_3Fe(CN)_6$, 97% purity), potassium chloride (KCl, 99.0% purity), glutaraldehyde solution (25 wt. % in H_2O), thioglycolic acid (TGA, 98.0% purity), *N*,*N*′-dicyclohexylcarbodiimide (DCC, 99.0% purity), *N*-hydroxysuccinimide (NHS, 97% purity), and *N*,*N*-dimethylformamide (DMF, 99.8% purity) were purchased from Sigma-Aldrich. All other reagents were of analytical grade and used without further purification.

Chicken egg yolk antibodies against Newcastle disease virus (IgY, 60 μg/mL) were obtained from Biotech-Vet Co. (Hanoi, Vietnam). Newcastle disease vaccine type M (inactivated NDV, 10^6 embryo infectious dose 50% (EID_{50})/mL) was purchased from Hanvet Co. JSc. (Hanoi, Vietnam). Avian influenza virus vaccines including H5N1 subtype (inactivated AIV/H5N1 virus) and H5N2 subtype (inactivated AIV/H5N2 virus) were supplied by Joint Stock Company Central Veterinary (Hanoi, Vietnam).

2.2. Measuring Setup. The integrated Au electrodes consisted of a 1 mm in diameter working electrode (WE) and a counter electrode (CE) in an $8.5 \times 12.2\,mm^2$ chip. These electrodes were deposited on a SiO_2/Si substrate by cathode sputtering technique. The detailed fabrication process was previously discussed [22]. The (100 μm in diameter) Ag/AgCl wire, used as a quasireference electrode (qRE), was prepared by oxidizing the silver wire [23]. The three-electrode system (including qRE) is integrated with a PDMS-based microchamber in which the qRE is immersed (independently) in a 100 μL open chamber (Figure 1(a)). This structure, on the one hand, reduces the microelectrode fabrication process in a clean room and, on the other hand, is convenient for electrical connection with a measuring circuit (Figure 1(b)). The system is wired with EC301 from Stanford Research Systems.

2.3. IgY Antibody Immobilization. To prepare a clean surface with ready functional groups before immobilizing IgY antibody, the integrated Au electrodes were pretreated in acetone, Piranha solution ($H_2O_2 : H_2SO_4$, 3 : 7), and ethanol. The electrodes were then rinsed with deionized water and nitrogen dried. After that, the Au electrodes were electrochemically activated in 0.5 M H_2SO_4 solution by sweeping the voltage from -0.5 V to +1 V vs. Ag/AgCl (in sat. 3 M KCl) at 50 mV/s until the cyclic voltammetry characteristics were stable.

Right after the surface treatment, chicken egg yolk antibodies (IgY) against ND virus were immobilized on the Au electrodes (WE) by two approaches, namely, protein A/glutaraldehyde (PrA/GA) and self-assembly modification/*N*-succinimidyl active ester (SAM/NHS).

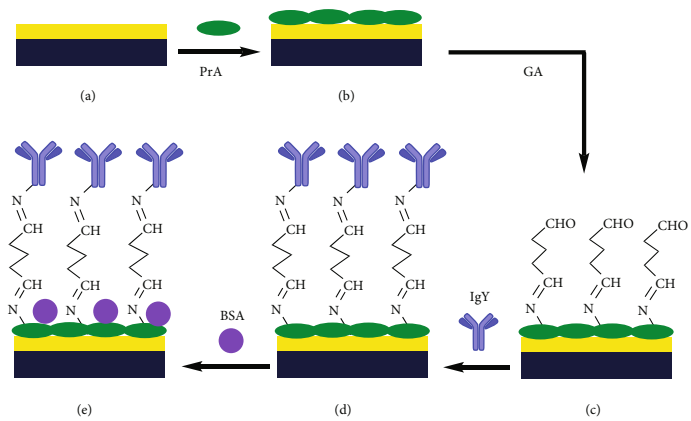

Figure 2: The scheme of antibody immobilization process using PrA/GA.

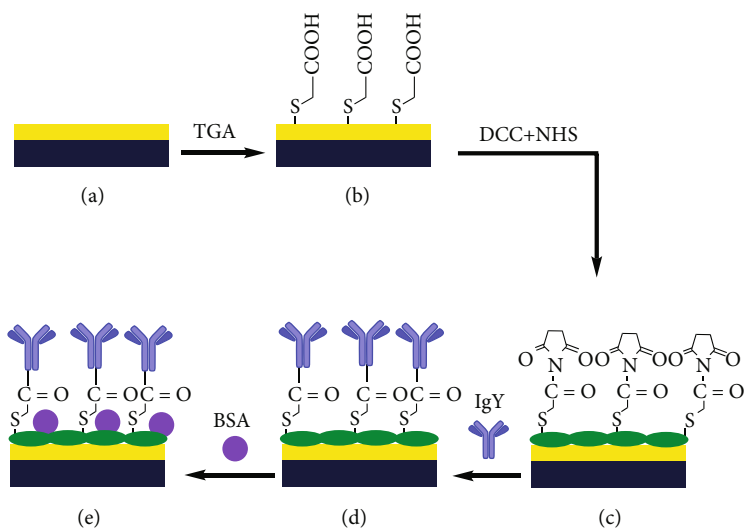

Figure 3: The scheme of antibody immobilization process using SAM/NHS.

2.3.1. The Scheme of Antibody Immobilization Process Using PrA/GA. The scheme of antibody immobilization process using PrA/GA is shown in Figures 2(a)–2(e). Firstly, the Au working electrode (WE) was incubated with a solution of protein A (1 mg/mL in PBS) for 3 hours. The PrA-modified electrode was then soaked in a solution of GA (5% wt. in deionized water) for 30 minutes. Then, IgY antibodies (60 μg/mL in PBS) were immobilized on the Au WE for 3 hours at 4°C. Lastly, BSA (1% wt./vol. in PBS) was deposited on the WE for 30 minutes to block unbound sites. After each modified step, the WE was rinsed with PBS to remove unbound molecules. The immunosensor was stored in a refrigerator at 4°C for further use.

2.3.2. The Scheme of Antibody Immobilization Process Using SAM/NHS. The scheme of antibody immobilization process using SAM/NHS is shown in Figures 3(a)–3(e). The Au WE was incubated with ethanol solution of 10 mM TGA for 24 hours for self-assembly modification (SAM) to occur. The excess TGA molecules on the modified WE were removed by rinsing with ethanol. The SAM-modified Au WE was treated with a DMF solution of 0.2 M DCC and 0.1 M NHS for 1 h at room temperature to convert the terminal carboxylic group to the active NHS ester. After rinsing with deionized water, the WE was incubated with 60 μg/mL solution (borate buffer, pH = 8.2) of IgY antibodies for 12 hours at 4°C. The excess antibodies were then washed off with PBS. BSA (1% wt./vol. in PBS) was also used to block unbound sites. Finally, the WE was rinsed with PBS, nitrogen dried, and stored at 4°C.

2.4. Newcastle Disease Virus Detection. In the three-electrode system, the Au (WE) was prepared with IgY antibodies and the fabricated Ag/AgCl qRE was wired with the microchamber (Figure 1). ND virus was detected using the label-free electrochemical immunosensor. 20 μL NDV sample (with varied concentrations of the NDV in 0.01 M PBS, pH 7.4) was injected into the microchamber. After the microchamber was incubated for 1 hour at 25°C, it was rinsed five times with PBS buffer. Electrolyte, composed of 0.1 M KCl and 0.03 M $K_3Fe(CN)_6/K_4Fe(CN)_6$ (1 : 1) as a redox couple, was pumped into the microchamber with the rate of 100 μL/min. Cyclic

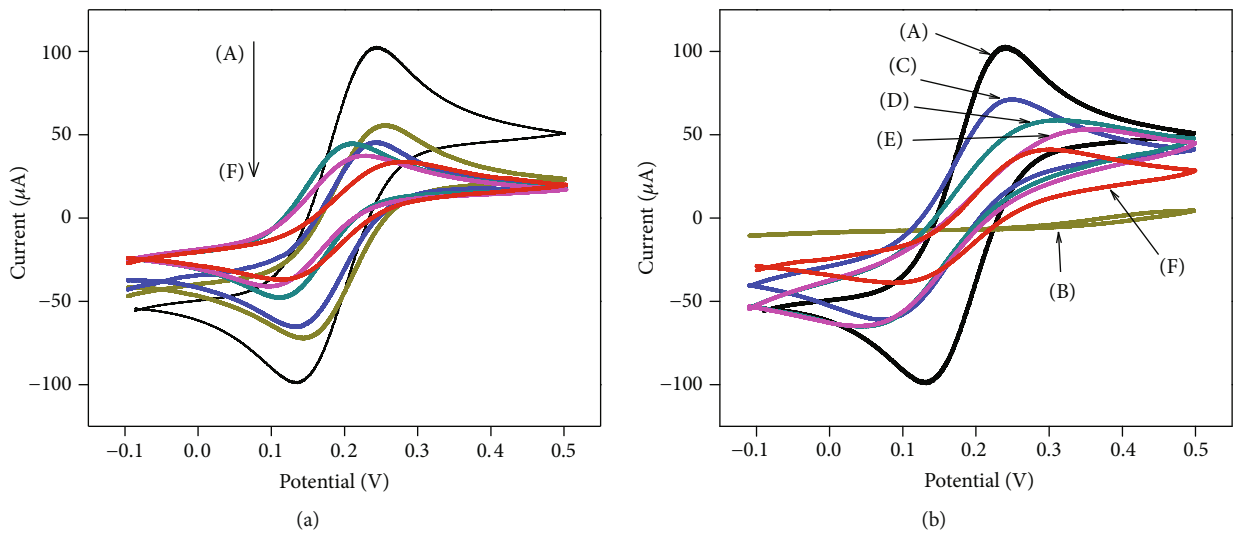

Figure 4: CV characterization of modified electrodes measured in the microchamber. (a) PrA/GA immunosensor: CV curve of (A) Au electrode, (B) PrA-Au electrode, (C) GA-PrA-Au electrode, (D) IgY-GA-PrA-Au electrode, and (E) BSA-IgY-GA-PrA-Au electrode and (F) after immunoreaction of 10^4 EID_{50}/mL NDV solution with PrA/GA immunosensor. (b) SAM/NHS immunosensor: (A) Au electrode, (B) TGA-Au electrode, (C) NHS-TGA-Au electrode, (D) IgY-NHS-TGA-Au electrode, and (E) BSA-IgY-NHS-TGA-Au electrode and (F) after immunoreaction of 10^4 EID_{50}/mL NDV solution with SAM/NHS immunosensor.

voltammetry (CV) measurements were performed using EC301 Stanford Research Systems; the potential was cycled from -0.2 to 0.5 V with scan rate 25 mV/s.

3. Results and Discussion

A cyclic voltammetry (CV) test was conducted using conventional reference electrode and the fabricated Ag/AgCl qRE (located inside the microchamber). In both cases, two peaks at 0.2 V/0.1 V and 0.27 V/0.17 V, representing the oxidation of $Fe(CN)_6^{4-}$ and reduction of $Fe(CN)_6^{3-}$, were observed on the CV curves. The measured peak current (I_{anodic} and $I_{cathodic}$) and the difference between the anodic and cathodic peak potentials, ΔE, stayed almost the same after 20 CV cycles (detail was described in supplemental data).

3.1. Immobilization of the IgY Antibody from Chicken Egg Yolk on the Au Electrode. Figure 4 shows CV characteristics of the WE measured in $Fe(CN)_6^{3-/4-}$ solution with different IgY antibody immobilization step for PrA/GA immunosensor (Figure 4(a)) and SAM/NHS immunosensor (Figure 4(b)). The difference in the current peak ($I_{peak} = I_{anodic} - I_{cathodic}$) was used to demonstrate the formation of the layers of the immunosensor during stepwise modification procedures (see Table S1 in supplemental information).

3.1.1. Antibody Immobilization Using PrA/GA Approach. As observed in Figure 4(a), the highest I_{peak} (202.8 μA) on the CV curve obtained with the bare Au electrode due to high conductivity and low barrier of gold metal makes it easy for electron transfer. The adsorption of protein A on the Au surface formed an insulating layer that reduces electron transfer leading to a lower peak current of the Au/PrA electrode ($I_{peak,Au/PrA} = 129.2\,\mu$A). The attachment of glutaraldehyde linkers onto the PrA/Au electrode also resulted in a reduction of I_{peak} ($I_{peak,Au/PrA/GA} = 110.0\,\mu$A). Glutaraldehyde plays a cross-linking role between protein A and IgY antibody through the formation of imine bonds (C=N bonds) between -CHO groups and $-NH_2$ groups as shown in Figure 2. The immobilization of IgY antibodies caused a further decrease in I_{peak} ($I_{peak,Au/PrA/GA/IgY} = 99.0\,\mu$A).

The above discussion revealed that the binding of IgY antibodies on the surface of immunosensor leads to an increase in the charge transfer resistance of $Fe(CN)_6^{3-/4-}$ redox couple to the Au electrode, thereby reducing the peak current. When the WE was deposited with BSA for blocking unbound sites and the IgY antibody was immobilized on the Au electrode, a slight decrease in the peak current was also observed ($I_{peak,PrA-GA\ immunosensor} = 87.3\,\mu$A).

3.1.2. Antibody Immobilization Using SAM/NHS Approach. As shown in Figure 3(b), a self-assembled modification (SAM) of TGA is formed on the Au electrode surface through the strong gold-thiolate bonds leading to the formation of a highly insulating surface layer that blocks almost all the faradic currents [24, 25]. That is why no (current) peak on the curve (B) was observed (Figure 4(b)). The reason for this is that the negatively charged terminal carboxyl groups of TGA (formed by the deprotonation in aqueous solution) prevent the transfer of negative $Fe(CN)_6^{3-/4-}$ redox couple to the electrode surface creating a depleted layer between the sensor surface and solution. If the TGA layer is activated by DCC and NHS, it forms an NHS ester and the negatively charged carboxyl groups of TGA are replaced by the neutrally charged NHS esters as shown in Figure 3(c). Thus, the transfer of the negative $Fe(CN)_6^{3-/4-}$ redox couple to the electrode surface makes it advantageous for the current to

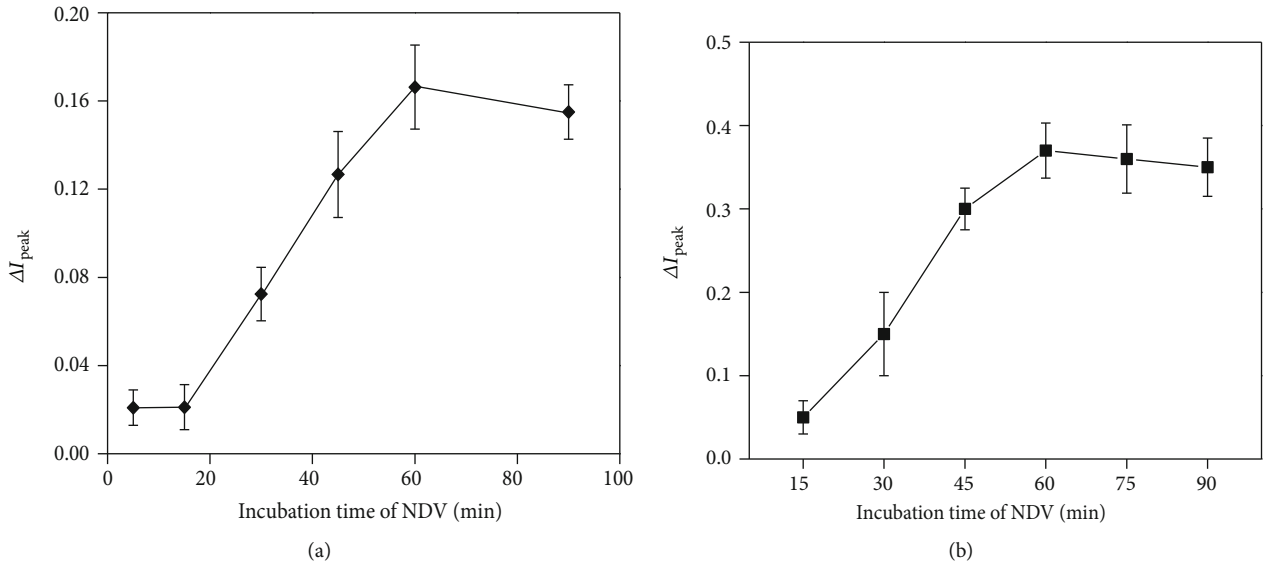

Figure 5: The output signal of immunosensor depends on incubation time: (a) PrA/GA immunosensor (with 10^6 EID_{50}/mL NDV) and (b) SAM/NHS immunosensor (with 10^2 EID_{50}/mL NDV).

flow. As a result, the current density is increased as illustrated in Figure 4(b) (C) ($I_{peak,Au/TGA/DCC+NHS} = 132.29\,\mu A$).

The immobilization of IgY antibodies on the immunosensor's surface in which active NHS ester is replaced by the amine groups of anti-NDV IgY (Figure 3(d)) leads to an increase in the charge transfer resistance of $Fe(CN)_6^{3-/4-}$ redox couple to the Au electrode, thereby reducing the peak current ($I_{peak,Au/TGA/DCC+NHS/IgY} = 124.75\,\mu A$). When the WE was deposited with BSA for blocking unbound sites, a further slight decrease in the peak current was also observed in Figure 4(b) (E) ($I_{peak,SAM-NHS\,immunosensor} = 116.7\,\mu A$). The two immobilization methods of IgY antibodies on the Au electrode exhibit good repeatability that are demonstrated by small deviation values of $I_{peak,immunosensor}$ (as shown in Figure S2 of supplemental data).

3.2. Newcastle Disease Virus Detection. The current response of immunosensors after reaction with NDV was also characterized by CV measurements in $K_3Fe(CN)_6/K_4Fe(CN)_6$ solution with a scan rate of 25 mV/s and shown as each curve (F) in Figure 4(a) (PrA/GA immunosensor) and Figure 4(b) (SAM/NHS immunosensor).

As observed in Figure 4(a), in the case of PrA/GA immunosensor, when specific antibody-virus interaction occurred on the surface of the immunosensor, the peak current ($I_{peak,NDV/immunosensor} = 79.1\,\mu A$, curve (F)) decreased compared to that of the immunosensor without biological interactions ($I_{peak,immunosensor} = 88.2\,\mu A$, curve (E)). Performing the same experiment using the SAM/NHS immunosensor (Figure 4(b)), one could obtain the similar result. The peak current ($I_{peak,NDV/immunosensor} = 60.3\,\mu A$, curve (F)), given by the interaction between specific antibody and virus that occurred on the surface of the immunosensor, was smaller than that with no biological interactions ($I_{peak,immunosensor} = 116.7\,\mu A$, curve (E)). The above results could explain that NDV are bound on the surface of the immunosensor based on specific antibody-virus interaction and therefore inhibiting the charge transfer process of $Fe(CN)_6^{3-/4-}$ redox couple to the Au electrode surface, resulting in a decrease in current response.

The output signal of the immunosensor is calculated by the following equation:

$$\Delta I_{peak} = \frac{I_{peak}(0) - I_{peak}(i)}{I_{peak}(0)}, \quad (1)$$

where $I_{peak}(0)$ is the I_{peak} of the immunosensor treated with 0 EID_{50}/mL NDV (in 0.01 M PBS, pH = 7.4), and $I_{peak}(i)$ is the I_{peak} of the immunosensor obtained after incubating with a certain NDV sample.

3.3. Effect of Virus Incubation Time on the Output Signal of the Immunosensors. In both cases of PrA/GA immunosensors and SAM-NHS immunosensors, the current responses increase accordingly with the incubation time and ΔI_{peak} reaches its maximum value ($\Delta I_{peak} = 0.166$ and $\Delta I_{peak} = 0.370$, respectively) at 60 minutes for the immunoreaction (Figures 5(a) and 5(b)). Further increase in incubation time did not cause significant change in ΔI_{peak} for both types of immunosensors.

$$\text{IgY Antibody} + \text{Antigen (ND Virus)} \rightarrow \text{Immune complex} \quad (2)$$

This is due to the nonlinear kinetic of the reversible immunoreaction as shown below that reaches its fastest rate of the association in the first hour [26]. Therefore, for further experiments, 60 min is selected as the virus incubation time for both types of immunosensors.

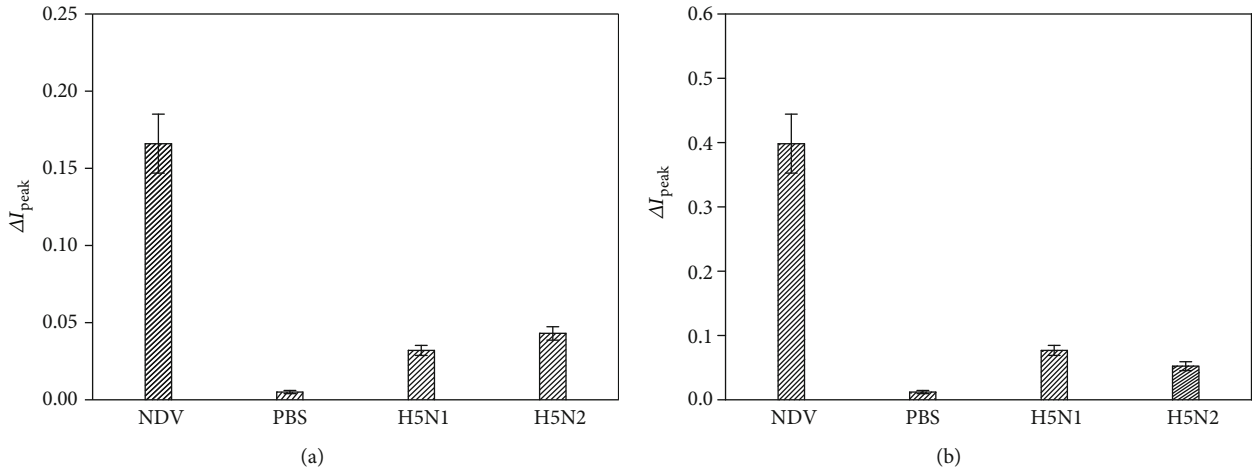

Figure 6: Specificity of the PrA/GA (a) and SAM/NHS (b) immunosensors for NDV detection. The output signals, ΔI_{peak}, of the immunosensors induced by 10^2 EID_{50}/mL NDV and nonspecific samples such as 0.01 M PBS (pH = 7.4), 10^2 EID_{50}/mL AIV/H5N1, and 10^2 EID_{50}/mL AIV/H5N2.

3.4. Specificity of the ND Virus Immunosensors. In order to evaluate the specificity of the PrA/GA and SAM/NHS immunosensors for the detection of NDV, ΔI_{peak} induced by PBS as the blank and several nonspecific viruses was measured. Nonspecific viruses, including H5N1 and H5N2 avian influenza A virus, and specific NDV were all prepared in 10^2 EID_{50}/mL. The immunoreactions were carried out with NDV, PBS, AIV/H5N1, and AIV/H5N2 samples for 1 h at 25°C in the microchamber. The specificity of the PrA/GA and SAM/NHS immunosensors for the NDV is exhibited in Figures 6(a) and 6(b). No obvious ΔI_{peak} response could be found under the blank (PBS). Similarly, at the same concentration, ΔI_{peak} obtained in the NDV measurement was much higher than that in cases of AIV/H5N1 and of AIV/H5N2. This implies that only the interaction between IgY antibody and NDV can cause significant current changes, another way to say that the developed PrA/GA and SAM/NHS immunosensors offer a good specificity to NDV.

3.5. Sensitivity of the ND Virus Immunosensors. To determine the sensitivity of the fabricated immunosensors, various samples of inactivated NDV with concentrations varying from 10^2 to10^6 EID_{50}/mL (in 0.01 M PBS, pH = 7.4) were tested. For each NDV concentration, five CV measurements were performed similarly using five immunosensors. The standard deviation of the measurements is calculated by the following formula:

$$S = \sqrt{\frac{1}{(N-1)} \sum_{i=1}^{N} \left[(\Delta I)_i - \overline{(\Delta I)} \right]^2}, \quad (3)$$

where N is the number of measurements corresponding to N immunosensors; $(\Delta I)_i$ is the output signal of the ith immunosensor; $\overline{(\Delta I)}$ is the average value of N ΔI values corresponding to N immunosensors; S is the real standard deviation (the absolute deviation), and $(S/\overline{\Delta I}) \times 100(\%)$ is the relative standard deviation.

After acquiring and processing the data, the calibration curves for both corresponding to the two types of fabricated immunosensors that express the relationship between ΔI_{peak} and the logarithm of ND virus concentration are presented in Figure 7. As shown in Figure 7, both types of immunosensors showed the linear relationship between ΔI_{peak} and $\log[C_{NDV}]$ in the range of 10^2 EID_{50}/mL–10^6 EID_{50}/mL NDV. The linear regression equation of the PrA/GA immunosensor was $\Delta I_{peak} = 0.0289 \times \log[C_{NDV}] - 0.0099$ ($R^2 = 0.983$) and that of the SAM/NHS immunosensor was $\Delta I_{peak} = 0.0588 \times \log[C_{NDV}] + 0.261$ ($R^2 = 0.991$). The calibration curve corresponding to the SAM/NHS immunosensor exhibited a higher slope value and ΔI_{peak} values at each concentration than those of the PrA/GA immunosensor.

According to Swartz [27], the limit of detection (LOD) and the limit of quantification (LOQ) can be calculated using the following equations:

$$\mathrm{LOD} = \frac{3.3 \times \sigma}{S}, \qquad \mathrm{LOQ} = \frac{10 \times \sigma}{S}, \quad (4)$$

where σ is the standard deviation of the response y-intercept of the regression line and S is the slope of the calibration curve. Table 1 shows the crucial parameters obtained from the two calibration curves corresponding to the two types of electrochemical label-free immunosensors. The LOD and LOQ were $10^{0.95}$ EID_{50}/mL and $10^{2.88}$ EID_{50}/mL in the case of PrA/GA immunosensor and $10^{0.67}$ EID_{50}/mL and $10^{2.03}$ EID_{50}/mL in the case of SAM/NHS immunosensor, respectively. It can be explained that, at the same measuring conditions and immune reaction (temperature, pH, incubation time, etc.), due to the formation of stable covalent bonds,

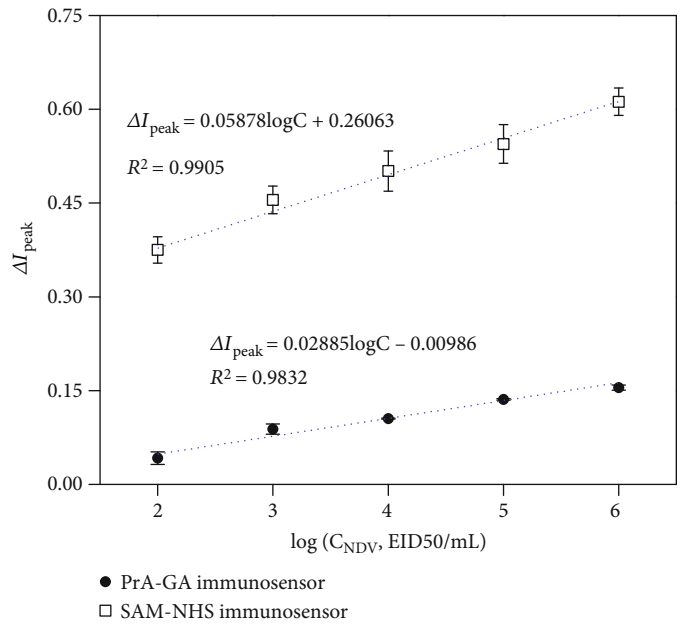

Figure 7: ΔI_{peak} is a function of NDV concentrations.

Table 1: The crucial parameters of the two types of electrochemical label-free immunosensors.

Parameter	PrA/GA immunosensor	SAM/NHS immunosensor
Linear range of concentration	10^2-10^6 EID_{50}/mL	10^2-10^6 EID_{50}/mL
Correlation coefficient (R^2)	0.983	0.991
Slope (S)	0.0289	0.0588
Standard deviation of the slope (SD_S)	0.00188	0.00286
y-intercept (y_i)	-0.0099	0.2606
Standard deviation of the y-intercept (σ)	0.0080	0.0119
LOD	0.95 (9 EID_{50}/mL)	0.67 (5 EID_{50}/mL)
LOQ	2.88 ($10^{2.88}$ EID_{50}/mL)	2.03 ($10^{2.03}$ EID_{50}/mL)

Table 2: Comparison of analytical properties of different methods for the detection of NDV.

Technique	Immobilization	Type	Antibody	Virus	Limit of detection	Ref.
Optic	APTES/CDI	Indirect	Goat monoclonal IgY	Purified NDV	2 ng/mL	[30]
RT-PCR				Inactivated NDV	5×10^2 ELD_{50}/mL	[31]
RT-PCR				Inactivated NDV	5×10^2 ELD_{50}/mL	[5]
RT-PCR				Inactivated NDV	$10^{5.8}$ ELD_{50}/mL	[6]
RRT-PCR				NDV RNA	10 EID_{50}/mL	[1]
CV	PrA/GA	Direct	IgY	Inactivated NDV	9 EID_{50}/mL	This work
CV	SAM/NHS	Direct	IgY	Inactivated NDV	5 EID_{50}/mL	

NDV: Newcastle disease virus; EID: embryo infectious dose; ELD: embryo lethal dose; RT-PCR: reverse transcriptase-polymerase chain reaction; RRT-PCR: real-time reverse transcription PCR.

the density of specific antibodies bound on the SAM/NHS immunosensor's surface is higher than that of the PrA/GA immunosensor. Moreover, the insulating property of PrA that influences the formation of the antibody-antigen complex partly contributes to lowering sensitivity of the PrA/GA immunosensor as compared to the SAM/NHS immunosensor.

Table 2 summarizes some analytical properties of different methods for the detection of NDV. The limits of detection values of the two types of electrochemical label-free immunosensors were comparable to those of the PCR. Moreover, the fabricated immunosensors also showed advantages over conventional ones such as simple process, do not require clean room facilities, quick response, direct detection,

and potential miniaturization by integrating with micro reactors (100 μL–1 mL in volume) which may be suitable for future on-site and in-field measurements. In particular, in this work, the chicken egg yolk antibody (IgY) was used as the biological recognition element of the immunosensor instead of using IgG antibody (monoclonal and polyclonal antibody) [16, 28, 29] which requires modern techniques and expensive biologicals and goes through many steps with complicated procedure [19, 20].

The study about using chicken egg yolk antibody (IgY) as the biological recognition element of the immunosensor may not only reduce analysis costs but also provide an effective solution to detect immediately virus in outbreaks of infectious diseases.

4. Conclusions

The integrated three-electrode system using fabricated Ag/AgCl electrode as qRE and the microchamber not only simplifies the microelectrode fabrication process in a clean room and reduces the analytical volume but also increases accuracy by enhancing the signal-to-noise ratio and thereby improving the sensitivity of electrochemical immunosensors. The IgY was used as the biological recognition element to replace purified IgG antibody that requires a complex extraction process and is time-consuming. The IgY against NDV was immobilized on the Au electrodes (WE) using PrA/GA and SAM/NHS approaches. Both immunosensors offer linear relationship with $\log[C_{NDV}]$ in the range of 10^2 EID_{50}/mL-10^6 EID_{50}/mL NDV. The fabricated immunosensors showed advantages over conventional ones such as simple process, do not require clean room facilities, quick response, direct detection, and potential miniaturization by integrating with micro reactors (100 μL–1 mL in volume) which may be suitable for future on-site and in-field measurements.

Data Availability

The data used to support the findings of this study are included within the article and the supplementary information file.

Conflicts of Interest

The authors declare that there is no conflict of interest regarding the publication of this paper.

Acknowledgments

This research is supported by the Vietnamese Ministry of Education and Training (MOET) under grant number B2015-01-102.

Supplementary Materials

A supplementary file is submitted along with the manuscript. In this file, Figure S1 shows the CV measured in $Fe(CN)_6^{3-/4-}$ solution at a 25 mV/s scan rate of the three-electrode system in the open cell using Ag/AgCl (in sat. 3 M KCl) conventional RE (curve a) and inside the microchamber using fabricated Ag/AgCl electrode as qRE (curve b). Besides, Table S1 shows the difference in the current peak ($I_{peak} = I_{anodic} - I_{cathodic}$) that was used to demonstrate the formation of the layers of the immunosensor during stepwise modification procedures. Finally, Figure S2 and Table S2 present the average values and the standard deviations of I_{peak} of six bare Au electrodes, six PrA/GA immunosensors, and six SAM/NHS immunosensors. *(Supplementary Materials)*

References

[1] T. Farkas, É. Székely, S. Belák, and I. Kiss, "Real-time PCR-based pathotyping of Newcastle disease virus by use of TaqMan minor groove binder probes," *Journal of Clinical Microbiology*, vol. 47, no. 7, pp. 2114–2123, 2009.

[2] H. Chaka, P. N. Thompson, F. Goutard, and V. Grosbois, "Evaluation of enzyme-linked immunosorbent assays and a haemagglutination inhibition tests for the detection of antibodies to Newcastle disease virus in village chickens using a Bayesian approach," *Preventive Veterinary Medicine*, vol. 119, no. 1-2, pp. 21–30, 2015.

[3] J. J. de Wit, F. G. Davelaar, and W. W. Braunius, "Comparison of the enzyme linked immunosorbent assay, the haemagglutination inhibition test and the agar gel precipitation test for the detection of antibodies against infectious bronchitis and Newcastle disease in commercial broilers," *Avian Pathology*, vol. 21, no. 4, pp. 651–658, 1992.

[4] G. Thirumurugan, R. Jayakumar, K. Kumanan, A. T. Venugopalan, and K. Nachimuthu, "Latex immunoassay for rapid detection of Newcastle disease virus," *Tropical Animal Health and Production*, vol. 29, no. 4, pp. 227–230, 1997.

[5] S. G. Daniela, T. Barbara, and M. A. Hofmann, "Detection of Newcastle disease virus in organs and faeces of experimentally infected chickens using RT-PCR," *Avian Pathology*, vol. 29, no. 2, pp. 143–152, 2000.

[6] F. Perozo, P. Villegas, C. Estevez, I. Alvarado, and L. B. Purvis, "Use of FTA filter paper for the molecular detection of Newcastle disease virus," *Avian Pathology*, vol. 35, no. 2, pp. 93–98, 2006.

[7] H. Y. Wu, S. H. Chiou, J. H. Shien, P. C. Chang, and H. K. Shieh, "Detection of proteins and nucleic acids of Newcastle disease virus in Eimeria acervuline," *Avian Pathology*, vol. 28, no. 5, pp. 441–445, 1999.

[8] P. Skládal, "Advances in electrochemical immunosensors," *Electroanalysis*, vol. 9, no. 10, pp. 737–745, 1997.

[9] R. Wang, J. Lin, K. Lassiter et al., "Evaluation study of a portable impedance biosensor for detection of avian influenza virus," *Journal of Virological Methods*, vol. 178, no. 1-2, pp. 52–58, 2011.

[10] J. Heo and S. Z. Hua, "An overview of recent strategies in pathogen sensing," *Sensors*, vol. 9, no. 6, pp. 4483–4502, 2009.

[11] B. Pejcic, R. De Marco, and G. Parkinson, "The role of biosensors in the detection of emerging infectious diseases," *Analyst*, vol. 131, no. 10, pp. 1079–1090, 2006.

[12] Y. Wang, Q. He, Y. Dong, and H. Chen, "In-channel modification of biosensor electrodes integrated on a polycarbonate microfluidic chip for micro flow-injection amperometric determination of glucose," *Sensors and Actuators B: Chemical*, vol. 145, no. 1, pp. 553–560, 2010.

[13] P. He, Z. Wang, and W. Yang, "Development of a label-free electrochemical immunosensor based on carbon nanotube for rapid determination of clenbuterol," *Food Chemistry*, vol. 112, no. 3, pp. 707–714, 2009.

[14] J. Wu, R. Wang, H. Yu et al., "Inkjet-printed microelectrodes on PDMS as biosensors for functionalized microfluidic systems," *Lab on a Chip*, vol. 15, no. 3, pp. 690–695, 2015.

[15] T. L. Tran, T. X. Chu, P. Q. Do et al., "In-channel-grown polypyrrole nanowire for the detection of DNA hybridization in an electrochemical microfluidic biosensor," *Journal of Nanomaterials*, vol. 2015, 7 pages, 2015.

[16] R. Wang, Y. Wang, K. Lassiter et al., "Interdigitated array microelectrode based impedance immunosensor for detection of avian influenza virus H5N1," *Talanta*, vol. 79, no. 2, pp. 159–164, 2009.

[17] J. Lum, R. Wang, K. Lassiter et al., "Rapid detection of avian influenza H5N1 virus using impedance measurement of immuno-reaction coupled with RBC amplification," *Biosensors & Bioelectronics*, vol. 38, no. 1, pp. 67–73, 2012.

[18] J. Zhou, L. Du, L. Zou, Y. Zou, N. Hu, and P. Wang, "An ultrasensitive electrochemical immunosensor for carcinoembryonic antigen detection based on staphylococcal protein A - Au nanoparticle modified gold electrode," *Sensors and Actuators B: Chemical*, vol. 197, pp. 220–227, 2014.

[19] M. Page and R. Thorpe, "Purification of IgG using protein A or protein G," in *The Protein Protocols Handbook*, J. M. Walker, Ed., pp. 993-994, Humana Press, Totowa, NJ, 2nd Edition edition, 2002.

[20] P. J. Conroy, S. Hearty, P. Leonard, and R. J. O'Kennedy, "Antibody production, design and use for biosensor-based applications," *Seminars in Cell & Developmental Biology*, vol. 20, no. 1, pp. 10–26, 2009.

[21] T. Quang Thinh, T. Van Vu Quan, L. B. Dương, T. H. Thuy, C. T. Xuan, and M. Anh Tuan, "A label-free electrochemical immunosensor for detection of Newcastle disease virus," *IFMBE Proceedings*, *7th International Conference on the Development of Biomedical Engineering in Vietnam (BME7)*, vol. 69, pp. 699–703, Springer, Singapore, BME 2018.

[22] T. L. Tran, T. X. Chu, D. C. Huynh, D. T. Pham, T. H. T. Luu, and A. T. Mai, "Effective immobilization of DNA for development of polypyrrole nanowires based biosensor," *Applied Surface Science*, vol. 314, pp. 260–265, 2014.

[23] Y. Bi and J. Ye, "In situ oxidation synthesis of Ag/AgCl core–shell nanowires and their photocatalytic properties," *Chemical Communications*, vol. 2009, no. 43, pp. 6551–6553, 2009.

[24] S. J. Ding, B. W. Chang, C. C. Wu, M. F. Lai, and H. C. Chang, "Impedance spectral studies of self-assembly of alkanethiols with different chain lengths using different immobilization strategies on Au electrodes," *Analytica Chimica Acta*, vol. 554, no. 1-2, pp. 43–51, 2005.

[25] A. Tlili, A. Abdelghani, S. Hleli, and M. Maaref, "Electrical characterization of a thiol SAM on gold as a first step for the fabrication of immunosensors based on a quartz crystal microbalance," *Sensors*, vol. 4, no. 6, pp. 105–114, 2004.

[26] R. Reverberi and L. Reverberi, "Factors affecting the antigen-antibody reaction," *Blood Transfusion*, vol. 5, pp. 227–240, 2007.

[27] M. Swartz, *Handbook of Analytical Validation*, CRC Press, 2012.

[28] B. Byrne, E. Stack, N. Gilmartin, and R. O'Kennedy, "Antibody-based sensors: principles, problems and potential for detection of pathogens and associated toxins," *Sensors*, vol. 9, no. 6, pp. 4407–4445, 2009.

[29] C. Ding, H. Li, K. Hu, and J.-M. Lin, "Electrochemical immunoassay of hepatitis B surface antigen by the amplification of gold nanoparticles based on the nanoporous gold electrode," *Talanta*, vol. 80, no. 3, pp. 1385–1391, 2010.

[30] L. E. William and T. H. Gail, "Detection of Newcastle disease virus using an evanescent wave immuno-based biosensor," *Canadian Journal of Chemistry*, vol. 74, no. 5, pp. 707–712, 1996.

[31] S. Norbert, B. Katrin, L. Bruckner, and H. A. Martin, "Detection of Newcastle disease virus in poultry vaccines using the polymerase chain reaction and direct sequencing of amplified cDNA," *Vaccine*, vol. 13, no. 4, pp. 360–364, 1995.

Hindawi
Journal of Nanomaterials
Volume 2019, Article ID 6248725, 31 pages
https://doi.org/10.1155/2019/6248725

Review Article

Recent Advances in the Synthesis, Properties, and Biological Applications of Platinum Nanoclusters

Xin Huang,[1] **Zengbei Li**,[1] **Zhengguo Yu**,[1] **Xinjie Deng**,[1] **and Yi Xin**[2]

[1]*School of Textiles, Zhongyuan University of Technology, Zhengzhou 450007, China*
[2]*Department of Respiratory and Critical Care Medicine, The Fifth Affiliated Hospital of Zhengzhou University, Zhengzhou 450052, China*

Correspondence should be addressed to Xin Huang; xinhuang@zut.edu.cn

Received 3 April 2019; Accepted 12 July 2019; Published 8 September 2019

Guest Editor: Teofil Jesionowski

Noble metal nanoclusters (M NCs), defined as an aggregation of a few to tens of atoms, are considered a borderline between atoms and metal nanoparticles (M NPs), which tends to exhibit molecule-like behaviours such as discrete electronic state and size-dependent fluorescence. In the past decades, gold and silver nanoclusters (Au NCs and Ag NCs) have been massively explored and utilized in the field of industrial catalysis, optoelectronic devices, biological imaging, environmental detection, clinical diagnoses, and treatment. The analogue of Au and Ag NCs and platinum nanoclusters (Pt NCs), especially their biological applications, is relatively and rarely discussed. This review firstly investigates the synthetic methodology of Pt NCs including template-assisted and template-free approaches and then introduces their unique optical, catalytic, and thermal properties. Particular importance here is the biological applications of Pt NCs such as the bioimaging of various cells as a preferred fluorophore in contrast to traditional fluorescent markers (e.g., organic dye, semiconductor quantum dots, and fluorescent proteins), the usage of Pt NCs-based antitumour drugs as a new class chemotherapeutics for malignant tumour therapy, and the utilization of antibacteria as an alternative of Ag-based antibacterial agent. On the whole, the development of Pt NCs has already gained delectable progress; however, the study of ultrafine Pt NCs is at the beginning stage and there are still plenty of challenges like synthesis of near-infrared (NIR) fluorescent Pt NCs, the explicit signal pathway of cell apoptosis, and attempt in diverse biological applications that need to be urgently tackled in future.

1. Introduction

Noble metal like rhodium (Rh), palladium (Pd), silver (Ag), platinum (Pt), and gold (Au) is one kind of modish and desired material, according to their inherent resistance to oxidation and corrosion even in the moist environment [1–3]. Its physical and chemical properties appear to be entirely change as the size of metal continuously decreases into nanoscale because of the quantum size effect, surface effect, small size effect, and macroquantum tunnel effect [4]. For example, noble metal nanoparticles (M NPs) which are defined as the particle size ranged from 1 to 100 nm have the high surface-to-volume ratio and electrodynamic interaction, leading to emerge distinct electronic, magnetic, and optical properties in contrast to bulk counterparts or individual atoms [5, 6]. In view of freely moving delocalized electrons in the conduction band, metals in a bulk state are good optical reflectors and electrically conducting (Figure 1). As for M NPs, a specific size-dependent plasma absorption will be presented when the size is smaller than the average free path length of conduction electrons (i.e., <20 nm) based on Mie's theory [7, 8]. If the M NPs are irradiated by light, strong optical absorption and/or scattering phenomenon will happen forcefully relied on their size, morphology, and dielectric environment, which is recognized as localized surface plasmon resonance (LSPR) [9–11]. Consequently, M NPs show the intense colours owing to the collective oscillation of conduction electrons upon interaction with light and this particular property has been widely developed in catalysis, optoelectronics, sensing, and surface-enhanced Raman scattering (SERS) [12–16]. Further declining the size of metal nanomaterials

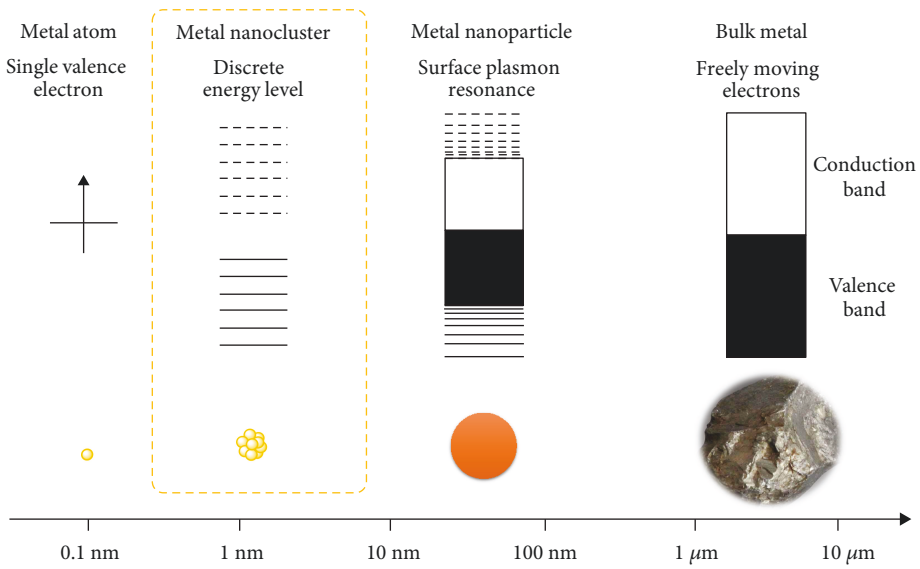

Figure 1: Schematic representation for size effect of metals. M NCs are a borderline between M NPs and atoms.

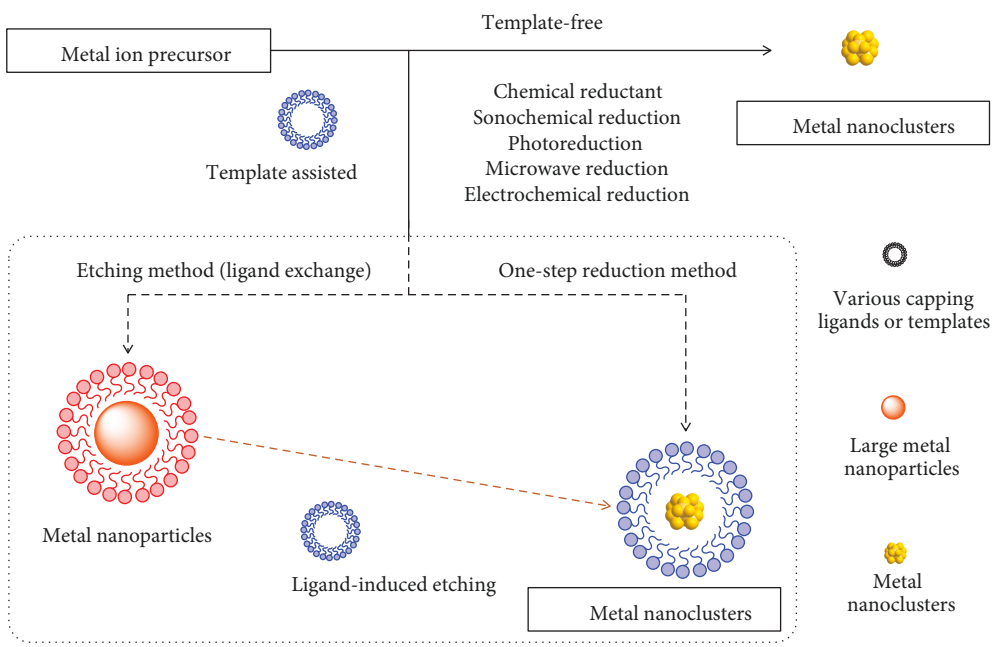

Figure 2: Schematic route for common synthesis of Pt NCs.

into around 0.1-2 nm, M NPs turn into metal nanocluster (M NC) region [17]. M NCs as a borderline between M NP and atoms were firstly discovered by Cotton and Haas in 1964 [18]. On this length scale, the electronic band structure of M NCs is broken down into discrete energy levels under the condition of free electrons' size near Fermi wavelength (i.e., <2 nm), resulting in the acquisition of molecule-like behaviours like the discrete electronic state [19–21]. Moreover, M NCs exhibit the intense light absorption and emission by the interaction between NCs and light *via* electronic transitions between energy levels. This unique electronic properties of M NCs are potently depended on their size, morphology, metal oxidation state, and surrounding ligands [22, 23]. Thus, a plenty of efforts focused on the preparation of desired and versatile M NCs by precise control of their sizes or shapes through meticulously choosing stabilized ligands or templates and the usage of NCs in an optical device [24, 25], chemical detection [26–29], catalytic conversion [30], and especially in biological applications [31].

Platinum (Pt), as one of the representative noble metal, has the physicochemical stability and remarkable resistance to corrosion even at high temperature based on its steady electrical structure [2]. Its physical and chemical inertness makes Pt widely employ in the fundamental industrial fields such as electrodes, dentistry equipment, Pt resistance

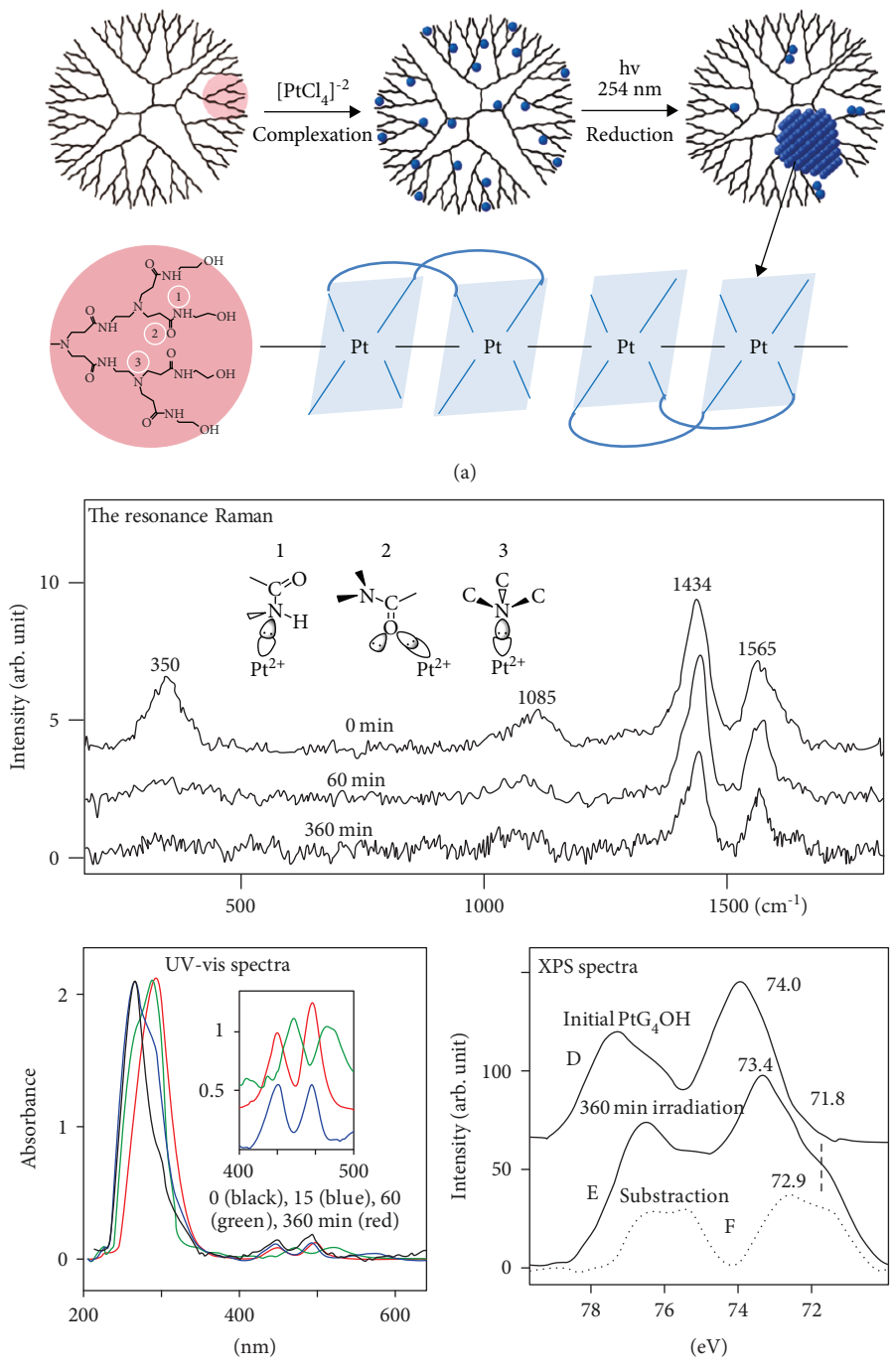

Figure 3: Continued.

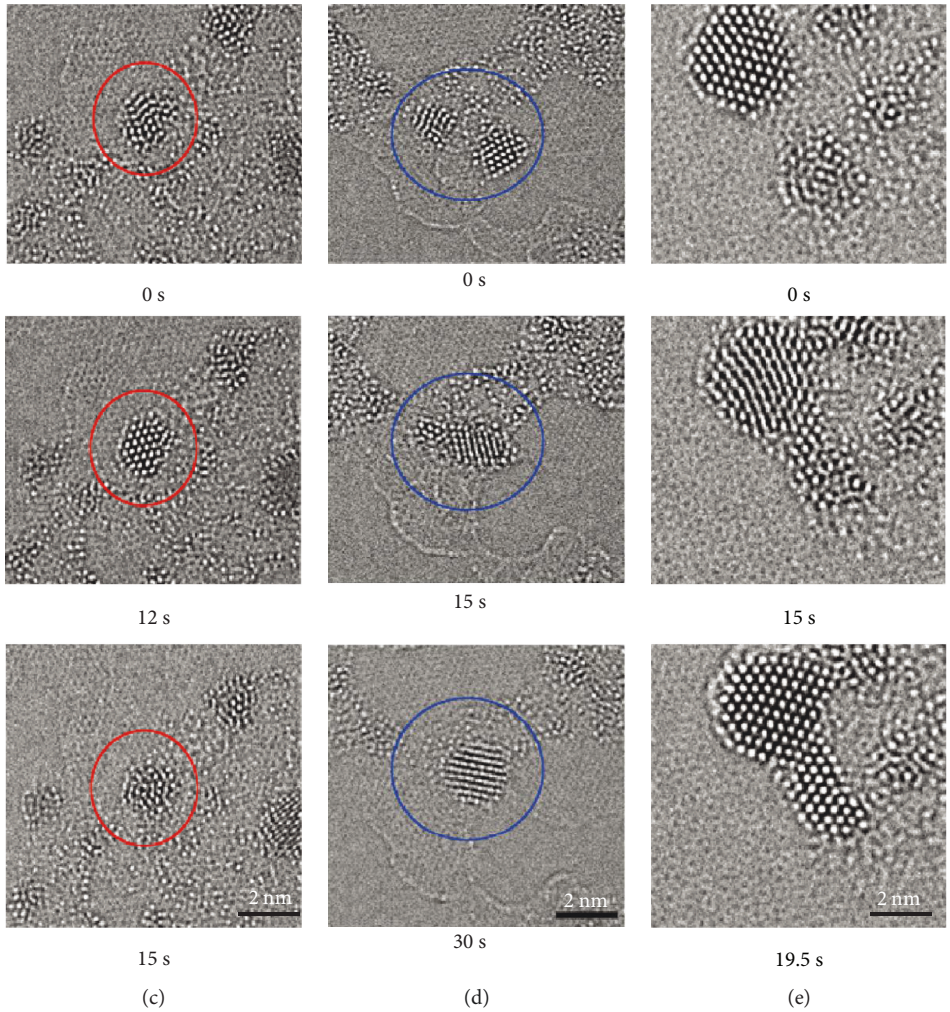

Figure 3: (a) Schematic process of the formation of Pt NCs using a dendrimer as a template under the UV light irradiation. (b) The resonance Raman, UV-vis, and XPS spectra of synthesized Pt NCs. The HR-TEM of dynamic transformation of Pt NCs at (c) metastable mesocrystal, (d) mesocrystal combination, and (e) oriented crystal, as the irradiation time increased (reprinted major modification with permission from [72], Copyright 2012, American Chemical Society).

thermometers, and catalytic converters [2, 32]. The fabrication and application of Pt materials on the subnanoscale became a research hotspot in the past few decades, especially in the catalysis and medicine. The most common utilizations of Pt nanomaterials are the catalysis of chemical reaction according to their high surface activity [33]. Based on their scarcity and preciousness, the research priorities of Pt materials are aimed at developing high-performance Pt-based materials through enhancing the catalytic efficiency as well as decreasing the usage amount. Undoubtedly, Pt's size and morphology play a critical and indispensable role [34]. On the other hand, Pt-based antineoplastic agents (like cisplatin, oxaliplatin, and carboplatin) have been universally used in the clinical chemotherapy against multiple cancers [35]. For example, Pt(II) anticancer drugs could induce the crosslinking of DNA, leading to the inhabitation of DNA synthesis or repair in tumour cells [36].

Up to now, typical Pt NPs demonstrated their applicable and prospective capacities in enormous areas such as gas detection, fuel cells, biosensors, and chemotherapeutics [37]. Besides, the analogues of Pt NCs, namely, Au NCs [38, 39], Ag NCs [40], Pd NCs [41] and Cu NCs [42], have been intensively investigated for their catalytic abilities, biological behaviours, and electrical and optical properties. By comparison of well-studied Pt NPs or congeneric NCs, the investigation of Pt NCs is just at an early stage in the last few decades; herein, this review summarizes the recent advance in the synthetic method of Pt NCs and special physicochemical properties, especially their fascinated biological applications.

2. Synthetic Method of Platinum Nanoclusters

In comparison to metal bulk or M NPs, the preparation of Pt NCs refers to the precise control and rigorous synthetic conditions due to their extreme small size [43]. There are many classification standards of the preparation method (Figure 2) [44–47], like physical and chemical method and one-pot and etching method. We generally divided the

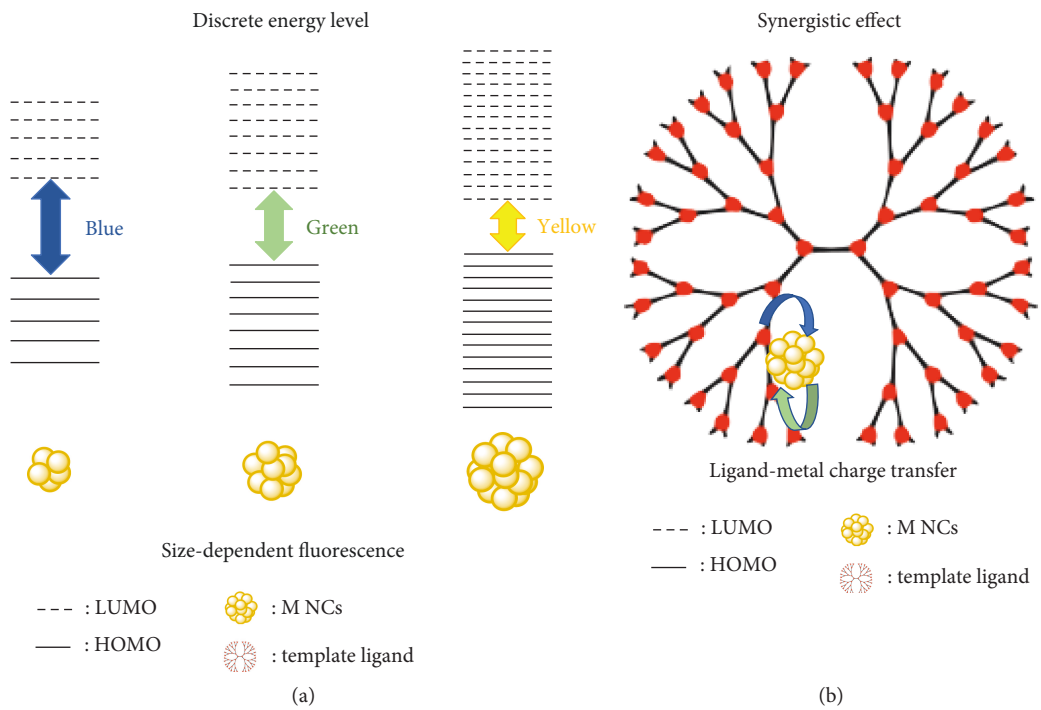

Figure 4: Schematic mechanism for (a) size-dependent fluorescence of Pt NCs and (b) the synergistic effect between metal and surrounding ligands.

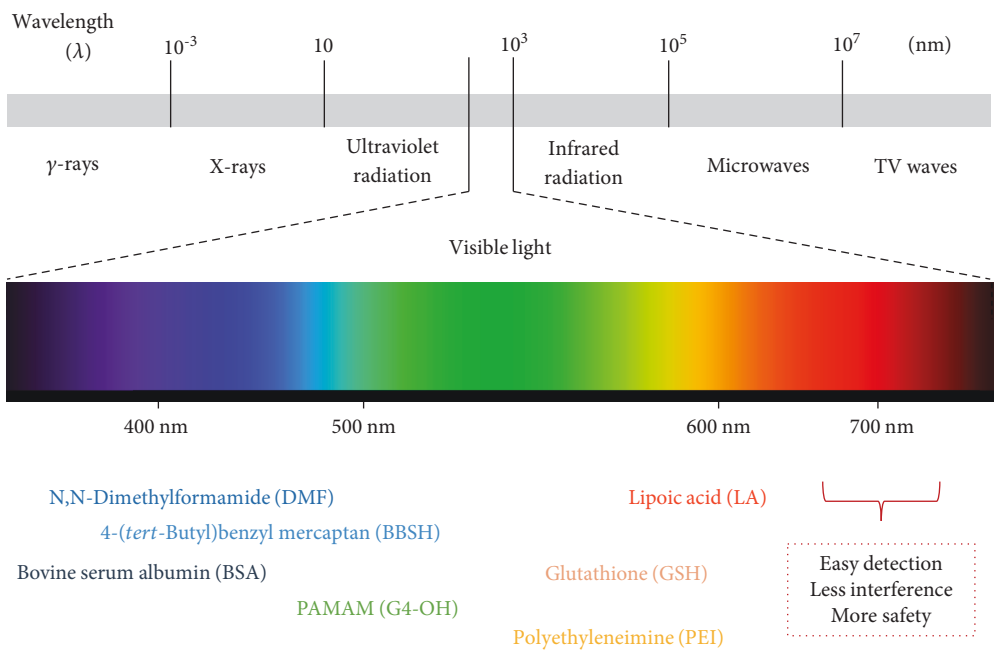

Figure 5: Schematic diagram of the used template for synthesizing fluorescent Pt NCs and the corresponding visible fluorescent emission region.

synthetic protocols of Pt NCs into two aspects: template-assisted method and template-free method.

2.1. Template-Assisted Method. Template-assisted method is based on the presence of various templates during the synthetic process, which plays a role as a protecting agent, a stabilizer, a capping agent, and even as the restrict space provider. The usual templates impart the M NCs' new unique features or specific structure by means of three main ways [3]: (1) decline of the surface energy to prevent the NCs' aggregation *via* electrostatic interaction, chemical bonding, and space steric effect; (2) accurate control and tailor of M NCs' size, dispersity, and morphology, which will profoundly influence, determine, and enhance their inherent functions;

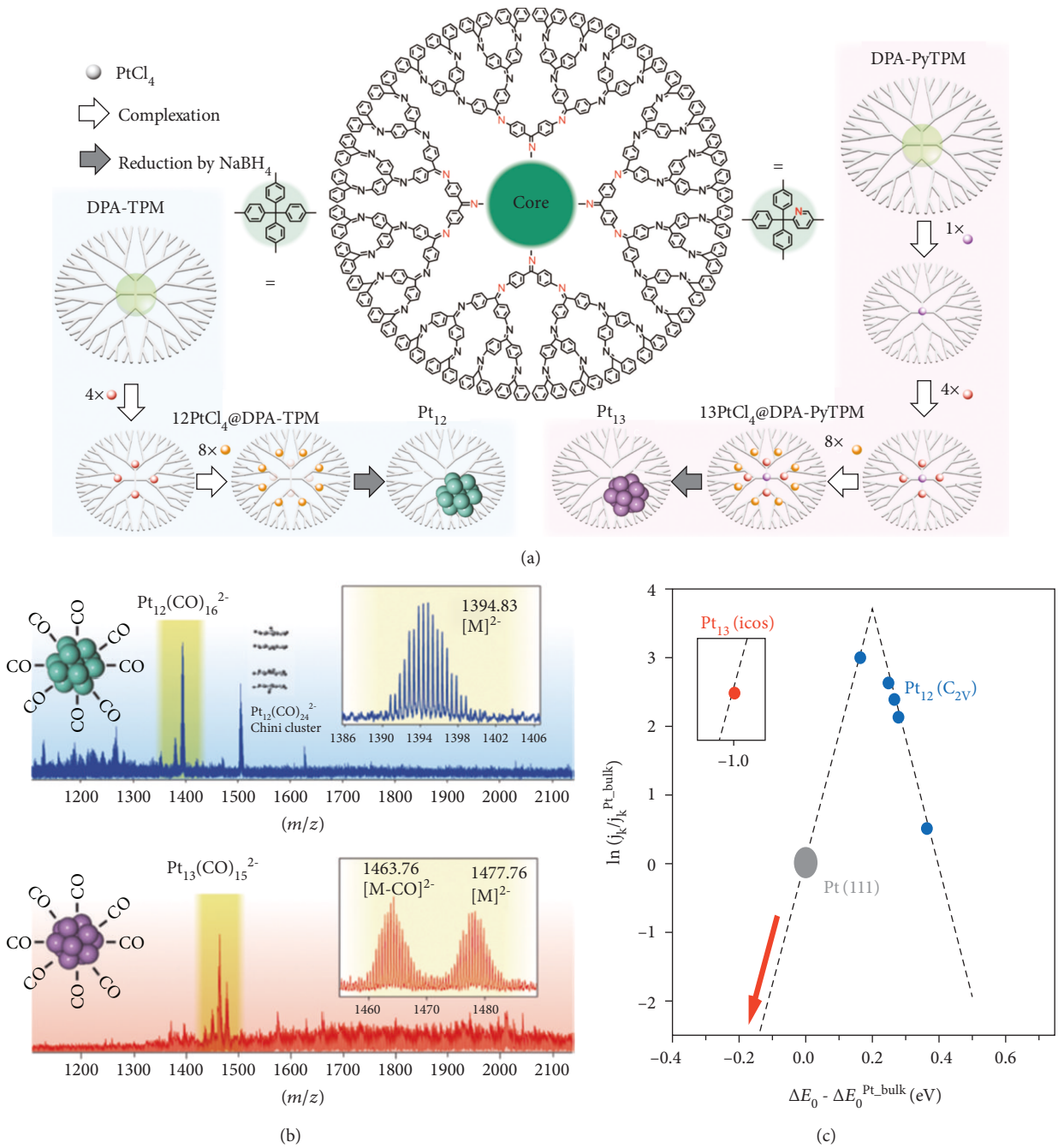

Figure 6: Continued.

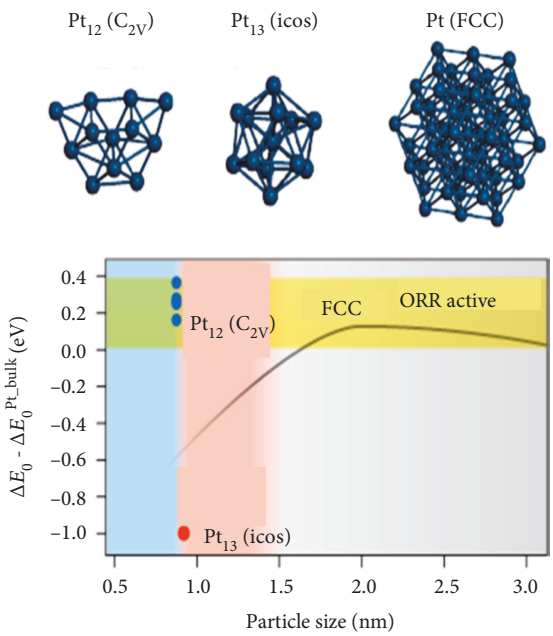

(d)

Figure 6: (a) Schematic process of preparing Pt_{12} and Pt_{13} NCs employed DPA-TPM and DPA-PyTPM as the template, respectively. (b) The electrospray ionization time of flight mass spectrometry (ESI-TOF-MS) of Pt NCs after ligand exchange by CO gas. (c) The diagrams of relationship between kinetic current density (j_K) and calculated oxygen adsorption energy (ΔE_0) for ORR using Pt-based catalyst, e.g., Pt_{12}, Pt_{13}, and $Pt_{(111)}$. (d) Simulated structures for optimized geometry of Pt_{12} NCs, Pt_{13} NCs, and FCC-structured Pt NPs and the relationship diagram of relative ΔE_0 and particle size (reprinted major modification with permission from [155], Copyright 2013, American Chemical Society).

and (3) decoration and modification of the M NCs' surface to endow some reactive functional groups in order to achieve the further applications. The ideal templates always include electron-rich atoms (e.g., N, P, S, and O) or certain functional groups (e.g., -COOH, $-NH_2$, -OH, and -SH).

Common templates utilized during the synthesis of M NCs are small organic molecules like representative surfactant, thiol compounds, organophosphorus compounds, and amino compounds [48–51]. Polymer ligand including nonionic and ionic polymers (such as acrylic polymer, amine polymer, polyethylene glycol, poly(N-vinyl-2-pyrrolidone), polypyrrole, and dendrimer) is another widely used template materials [52–54]. A polymer template stabilizes the NCs by chemical bonding and electrostatic effect, as well as steric effect due to large spatial configuration. Compared to small organic molecules, polymer has the easier modification, better controlling ability, and lower toxicity [55, 56], making them a preferred option for synthesis of M NCs. Furthermore, a biomacromolecule template, such as DNA, protein, oligonucleotides, and enzymes, is a kind of prevalent materials used to manufacture the medical and biological metal nanomaterials [57, 58]. Biomacromolecule is always relative to a specific biomolecular recognition function, multifunctional group (-SH, -COOH, -OH, and $-NH_2$), and excellent biocompatibility [59], showing a promising potential in the development of various biofunctional M NCs. In general, a template cannot reduce the metal precursor to form the M NCs without adding any other chemical redundant or with the help of physicochemical means such as the γ-radiolysis method [60], microwave-ultrasonic method [61], sonochemical method [62], photoreduction method [63], and electrochemical method [64].

Chemical etching method also called ligand-induced exchange etching involves two processes: the larger-sized M NPs are formed firstly under the stabilized template with a weak interaction and secondly, ligand-induced etching of larger-sized NPs occurs under the existing excess ligands by a strong interaction between ligands and metal atoms to produce smaller size NCs. Highly blue fluorescent Pt NCs with two peaks at 410/436 nm were synthesized by phase transfer through electrostatic interactions under an etching environment [65]. The presynthesized glutathione- (GSH-) protected Pt NPs were transferred into organic solvent with the support of cetyl trimethyl ammonium bromide (CTAB) to secondly form the fluorescent small Pt NCs. However, this method is always related to a time-consuming and complicated process, which is not suitable for the production of M NCs at a large scale.

Direct reduction in the present of templates and extra chemical reductant is a classical and extensive way to acquire the small size NCs. Atomically precise Pt NCs which consist of 11 atoms (Pt_{11} NCs) were obtained by a direct chemical reduction using small molecule 4-(*tert*-butyl)benzyl mercaptan (BBS) as the template and sodium borohydride ($NaBH_4$) as the reducing agent [66]. The structure of NCs was defined as $Pt_{11}(BBS)_8$ by matrix-assisted laser desorption-ionization mass spectrometry (MALDI-MS) and electrospray ionization (ESI) technology. Moreover, special octahedral Pt NCs were successfully synthesized employing glucose as the reducing agent and CTAB as the shape-control templates *via* one-pot

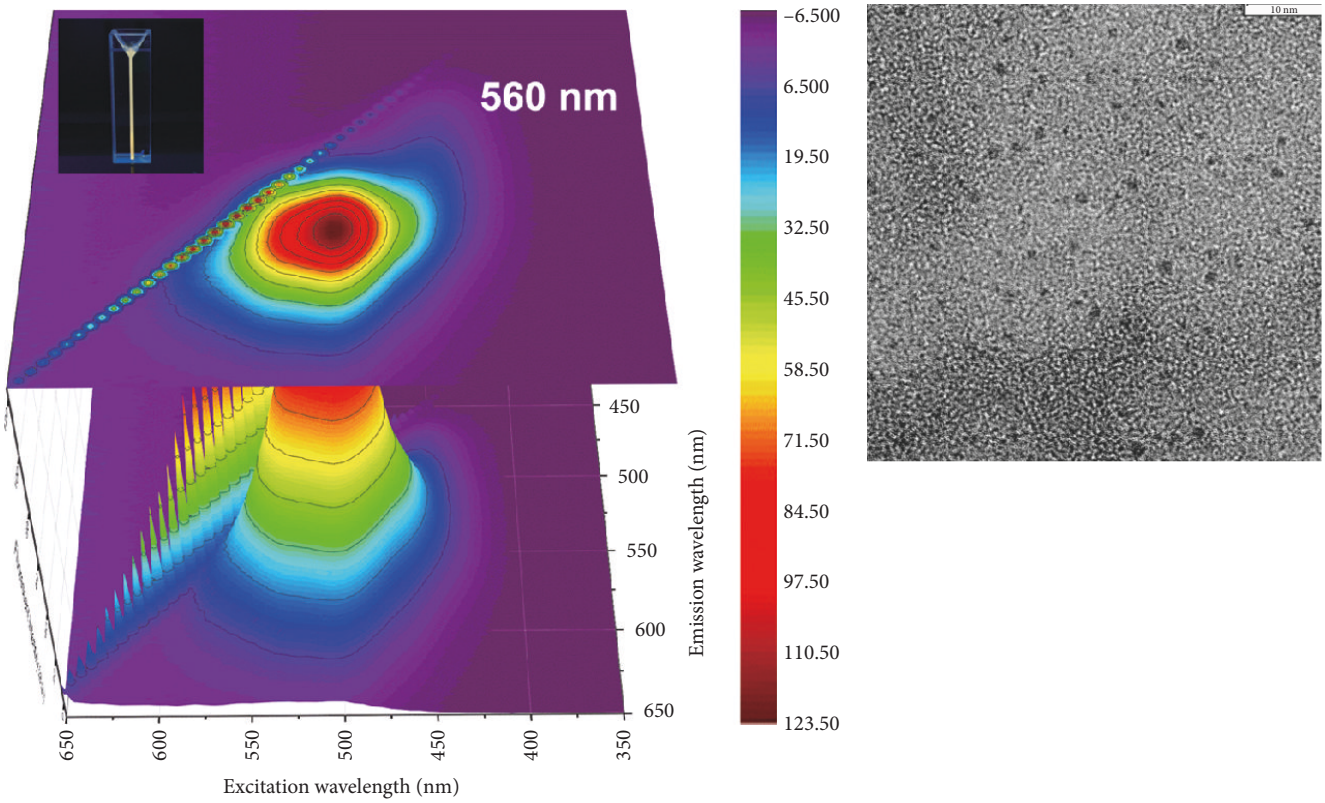

(a) (b)

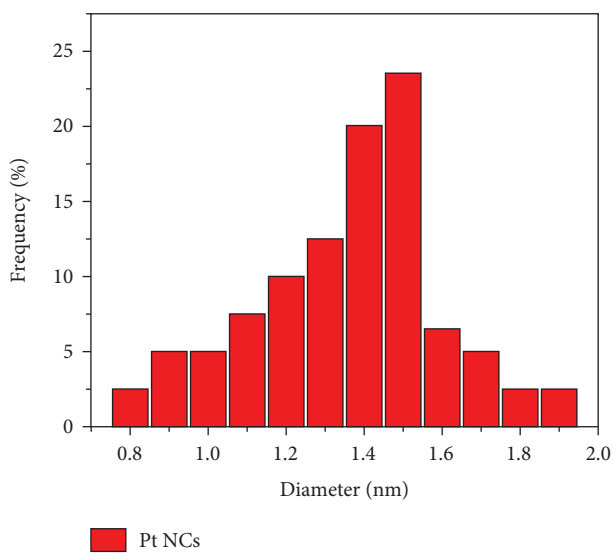

(c)

Figure 7: Continued.

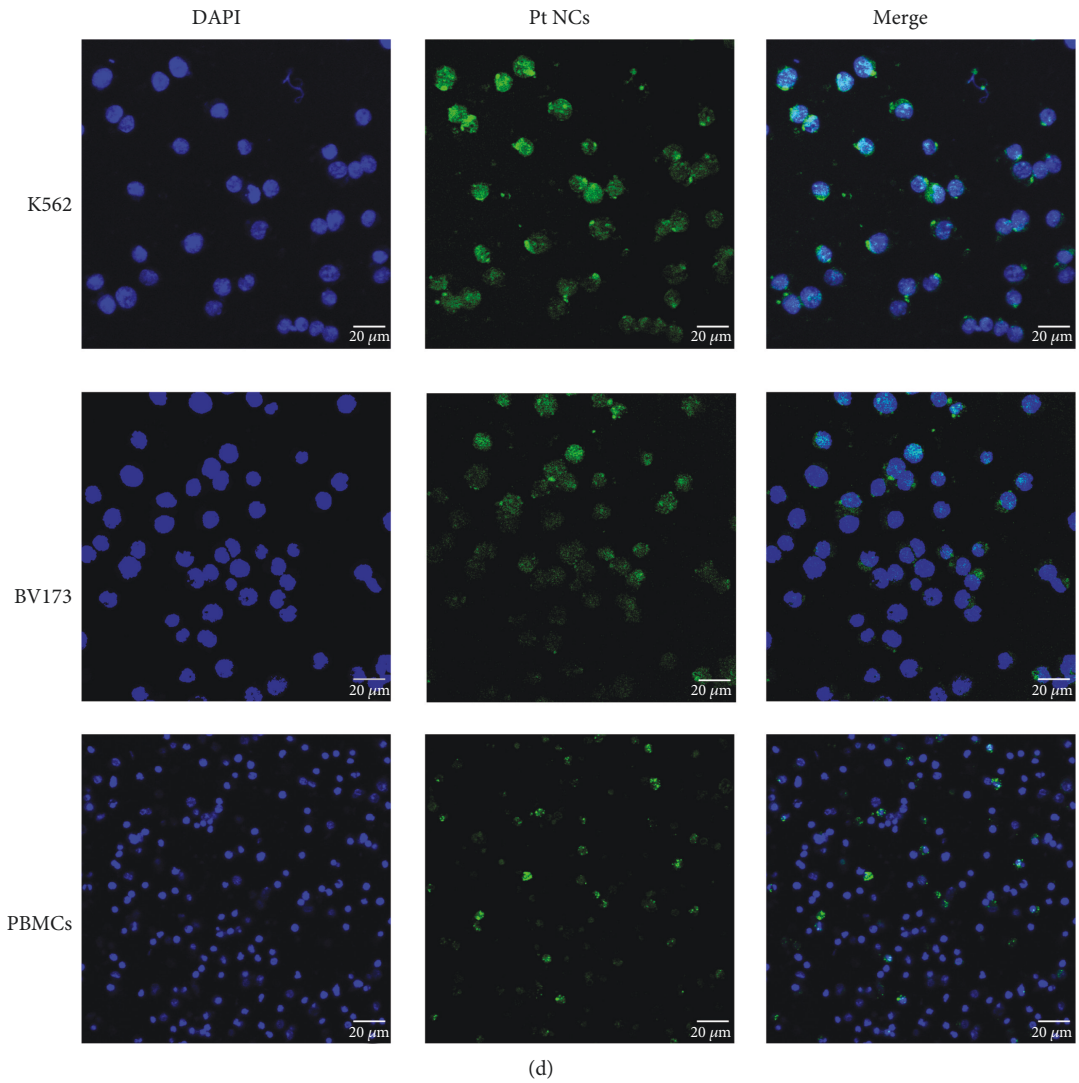

Figure 7: (a) 3D fluorescence spectra of Pt NCs. Insert is the photograph of Pt NCs under 365 nm UV irradiation. (b) TEM pictures of Pt NCs and (c) corresponding size distribution histogram. (d) Confocal microscopic photographs of K562, BV173 cancer cells, and normal PBMC cells after cultured with Pt NCs for 4 h. DAPI is employed to stain the cell nuclei emitting blue fluorescence, and Pt NCs show the green fluorescence (the scale bar is 20 μm) (reprinted major modification with permission from [186], Copyright 2018, Elsevier).

hydrothermal process [67]. The formation mechanism of octahedral NCs is that glucose reduces Pt ions into atoms and then atoms grow to octahedron by the precise control of CTAB, namely, the synergetic effect both of CTAB and glucose. Cho et al. put forward the sol-gel polymerization protocol of poly(2-hydroxyethyl-2-mercaptoethyl aspartamide) (PHMA) capped Pt NCs [47]. PHMA as a polymer template could control the morphology of NCs and organize their structure association, based on binding Pt procurers *via* amine functional groups and particles *via* thiol functional groups. For another instance, dendrimer, as a favourable template, has a uniform structure which can supply a predetermined formation environment to accurately control the NCs' size and morphology [68–71]. A linear structural Pt NCs with 4-8 atoms were fabricated inside of polyamidoamine dendrimer by UV irradiation at 254 nm (Figure 3) [72]. The tools of resonance Raman spectra, ultraviolet-visible (UV-Vis) spectroscopy, X-ray photoelectron spectroscopy (XPS), and high-resolution transmission electron microscopy (HR-TEM) were employed to clarify that the assemble of Pt nanocrystals is owing to an oriented attachment mechanism.

Physicochemical technique can assist the preparation of ultrafine Pt NCs, instead of using chemical reductants. Microwaves, as the electromagnetic waves, could obtain monodispersed M NCs by the fast and homogeneous heating [61]. Microwaves heat polar molecules rapidly at the high temperature without heating the glass container, leading to the formation of colloidal metal nanomaterials. The synthesized M NCs are always related to the high quality and narrow size distribution. Tu and Liu employed microwave irradiation to prepare the poly(N-vinyl-2-pyrrolidone)-supported Pt NCs with an average size at 1.52 ± 0.26 nm [73]. This method could continuously produce the uniform Pt NCs even at a large scale, satisfying industrial applications. Photoreduction is a simple, feasible, and nontoxic approach

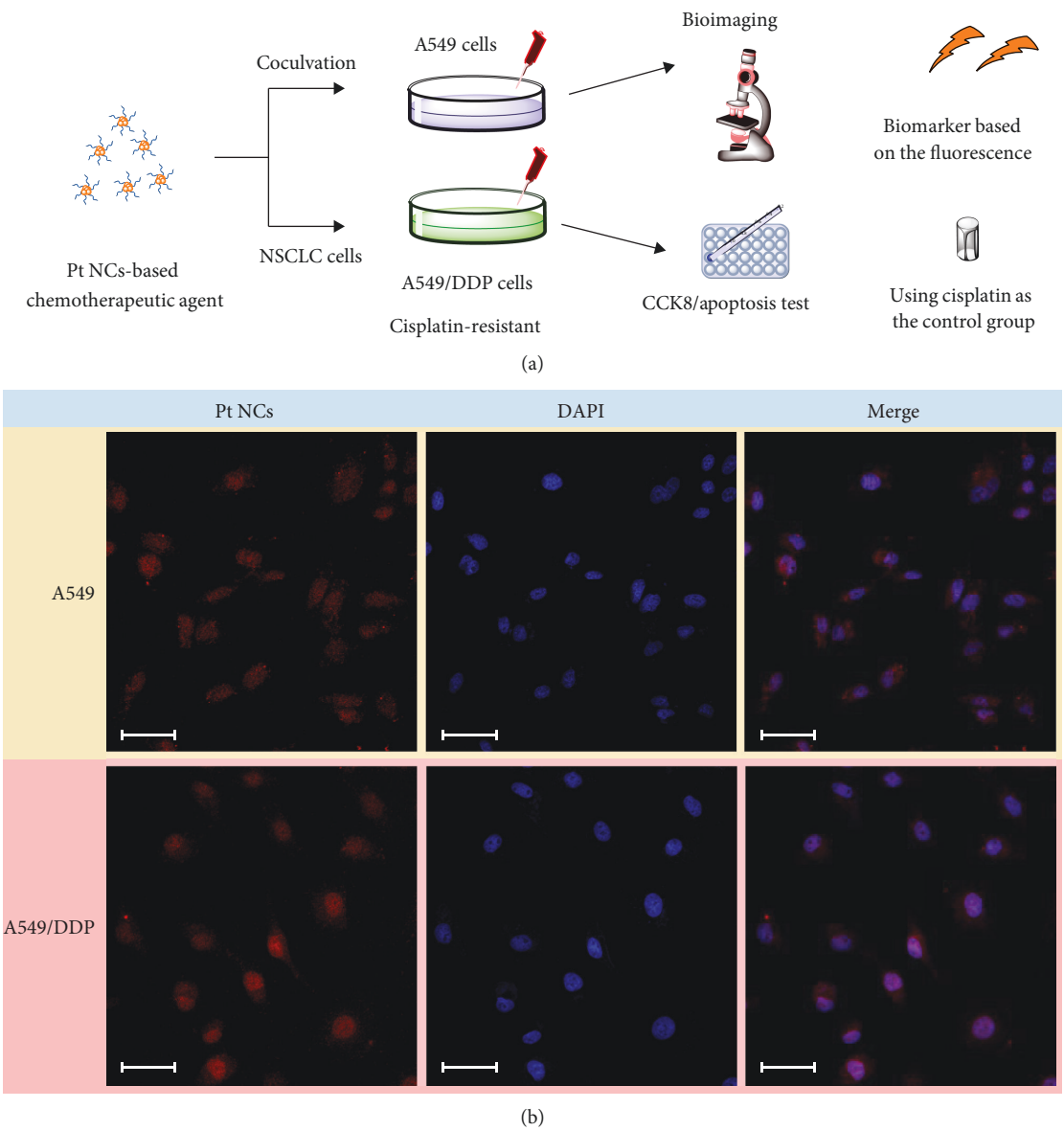

Figure 8: (a) The schematic process of bioimaging of human lung adenocarcinoma cells. (b) Confocal microscopic photographs of A549 and cisplatin-resistant A549/DDP cells cultured with Pt NCs-based chemotherapeutic agent (red fluorescence) after incubated for 4 h, respectively. DAPI stained cell nuclei (blue fluorescence), and the scale bar is 50 μm (reprinted with permission from [187], Copyright 2019, Elsevier).

avoiding the usage of additional reducing agents [74]. The reduction mechanism is due to the energy transfer under the condition of light irradiation to generate the reductive hydration electrons or reactive radicals [63], which is frequently utilized to explore the origination of photoluminescence because no other compounds are introduced. The Pt NCs with the size ranged from 1.0 to 2.2 nm were prepared with the aid of UV light under the alkaline environment [75]. The presynthesized NCs have a face-centred cubic spatial structure, and the author inferred that the UV light could achieve the nucleation and growth of NCs, not by the thermal reduction. Finally, electrodeposition is a usual and effective method to control size and shape of metals and decorate the substrate surface by adjusting deposition parameters, involving a plenty of distinct advantages such as low cost, rapid producing rates, and precious controllability [76, 77]. Qian et al. firstly modified the four-generation poly(amidoamine) dendrimer (G4-NH_2) onto indium-doped tin oxide (ITO) and then electrodeposited Pt NCs on the surface of G4-NH_2 dendrimer to form larger-sized NPs near 100 ± 20 nm [78]. The size and morphology could be tailored by polyelectrolytes or the types of PAMAM ligands. These physicochemical techniques mentioned above are environmentally friendly, less time-consuming, and convenient, which are beneficial to investigate the formation process and fluorescence mechanism and meet the demand of green industrial fabrication.

In addition, the defined templates during the formation of Pt NCs can be extended to a broad range involving multicomponent materials like multimetallic alloy [79–83] and

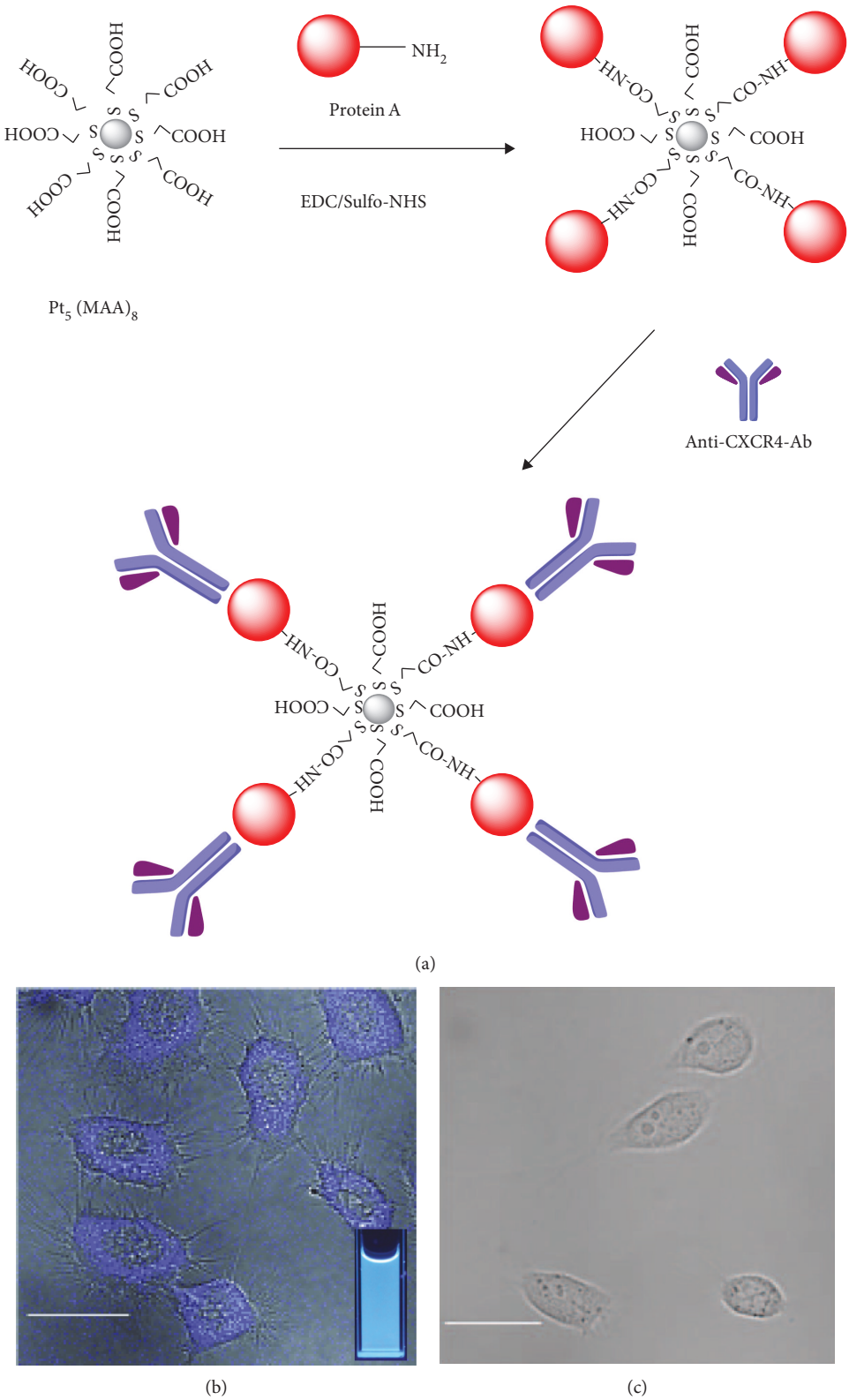

Figure 9: (a) The schematic fabrication of $Pt_5(MAA)_8$-protein A-anti-CXCR4-Ab complex. Confocal microscopic photographs merged with differential interference contrast (DIC) picture of (b) HeLa cells and (c) CHO-K1 cells stained by a blue fluorescent antibody-modified Pt complex. The scale bars are 20 μm (reprinted major modification with permission from [130], Copyright 2011, Wiley).

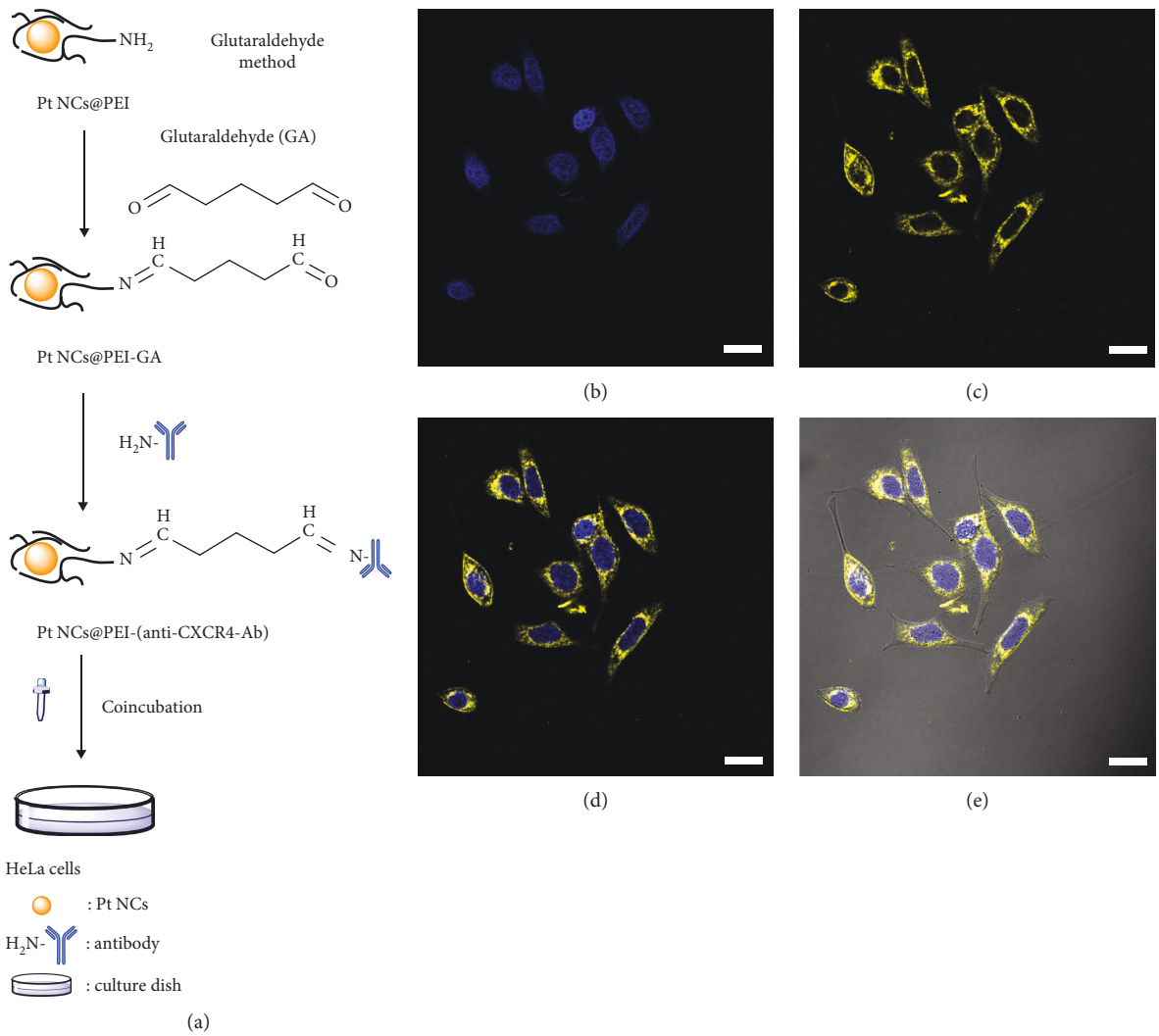

Figure 10: (a) The schematic synthesis of Pt NCs@PEI conjugated with the antibody by a glutaraldehyde method. Confocal microscopic photographs merged with differential interference contrast (DIC) picture of HeLa cells stained by (b) only DAPI, (c) only Pt NCs-antibody complex, (d) merge of (b) and (c), and (e) the bright filed of (d). The scale bars are 20 μm (reprinted major modification with permission from [188], Copyright 2016, Royal Society of Chemistry).

doped substrate material [84–87]. For instance, bimetallic or multimetallic alloy is designed by a combination concept of different metallic compounds in order to obtain composite performance. Pure Al, Co, and Pt were melted and then dealloyed in alkaline solution at certain temperature to form $Al_{85}Co_{14}Pt_1$ ternary alloy [88]. Even the amount of Pt was quite small, the electrocatalytical activity was improved dramatically and the ampere-metric determination limit of sodium nitrite ($NaNO_2$) was 0.067 μM ($S/N = 3$). On the other hand, a doped substrate method is allowing Pt NCs doped or dispersed into the substrate materials such as polymer film [89–92], inorganic substrate [93–96], metal organic framework (MOF) [97], carbon nanotubes (CNTs) [98, 99], and graphene [100–102], which could easily adjust and enhance the pure NCs' chemical and physical performance. Pt NCs with an average diameter of 0.7 ± 0.3 nm were deposited on $SmMn_2O_5$ (SMO) mullite-type oxides by an atomic layer deposition method (ALD), showing the efficient ability to solve the CO poisoning problem for the Pt-based catalyst [103]. This catalytic activity even under low temperature originated from O_2 dissociation at the bifunctional interface structure. Lee et al. put forward that monodispersed Pt NCs (diameter = 1.25 ± 0.30 nm) were loaded onto three-dimensional graphene-like carbon (3D GLC) which was employed in the electrochemical oxidation reaction [104]. These Pt NCs-doped 3D GLC catalysts possess near 2910 m^2/g superficial area and exhibit excellent glycerol oxidation reaction (GOR) activity and extreme stability *via* firm adhesion of glycerol on the Pt NCs' surface. Recently, Pt precursor solution was added into poly(diallyldimethylammonium chloride) and poly(sodium 4-styrenesulfonate) to assemble polyelectrolyte multilayer (PEM) films and then the Pt NCs were in situ yielded with various sizes from 1.2 to 2.3 nm only by tailoring the salt concentration and reduction time, instead of the reduction temperature [105].

2.2. Template-Free Method. Template-free protocol is a method avoiding the introduction of extra substance and

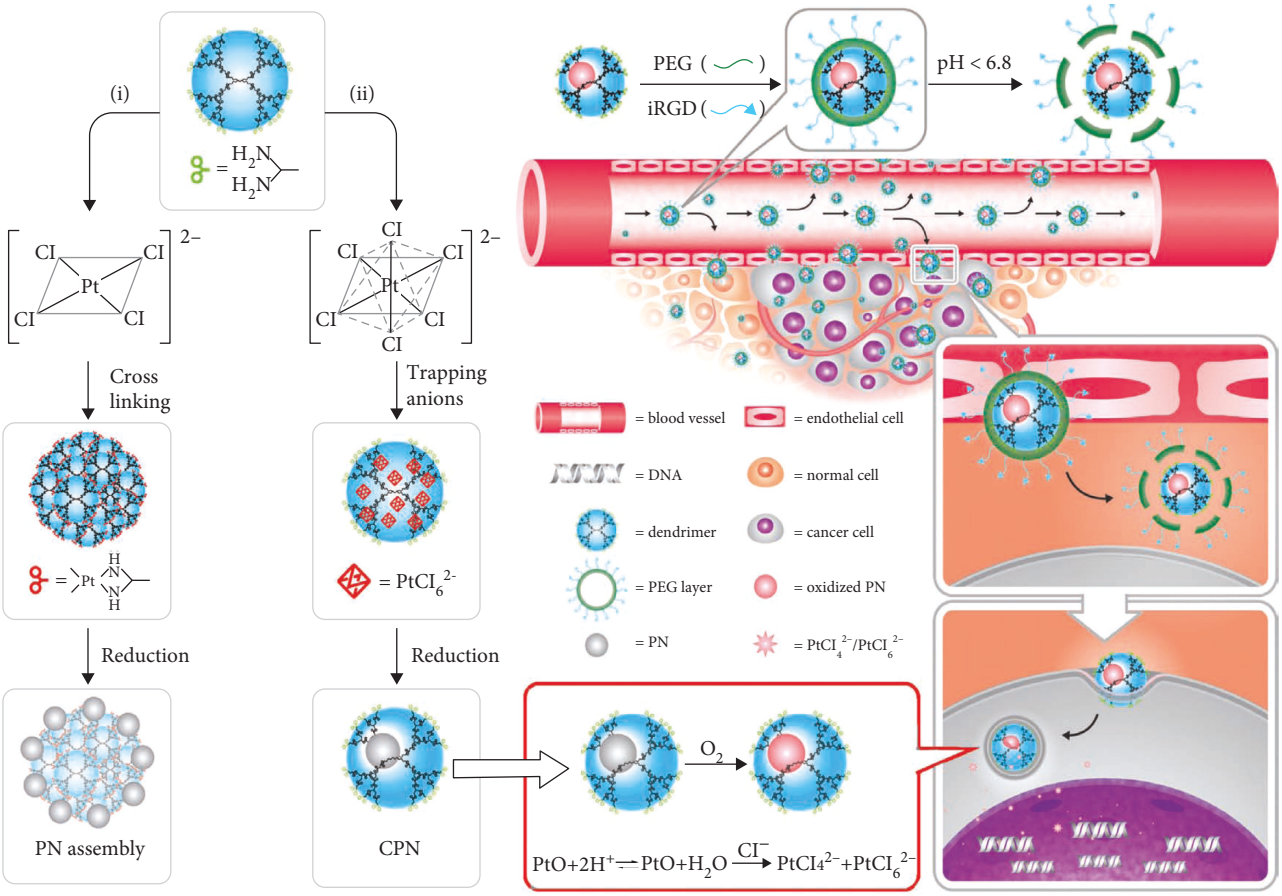

(a)

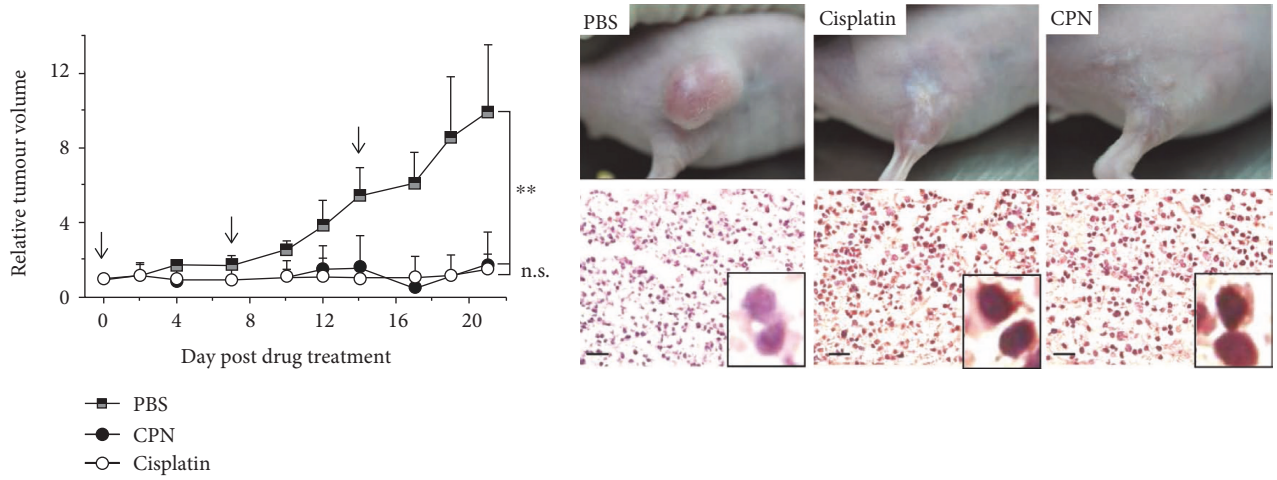

(b)

Figure 11: Continued.

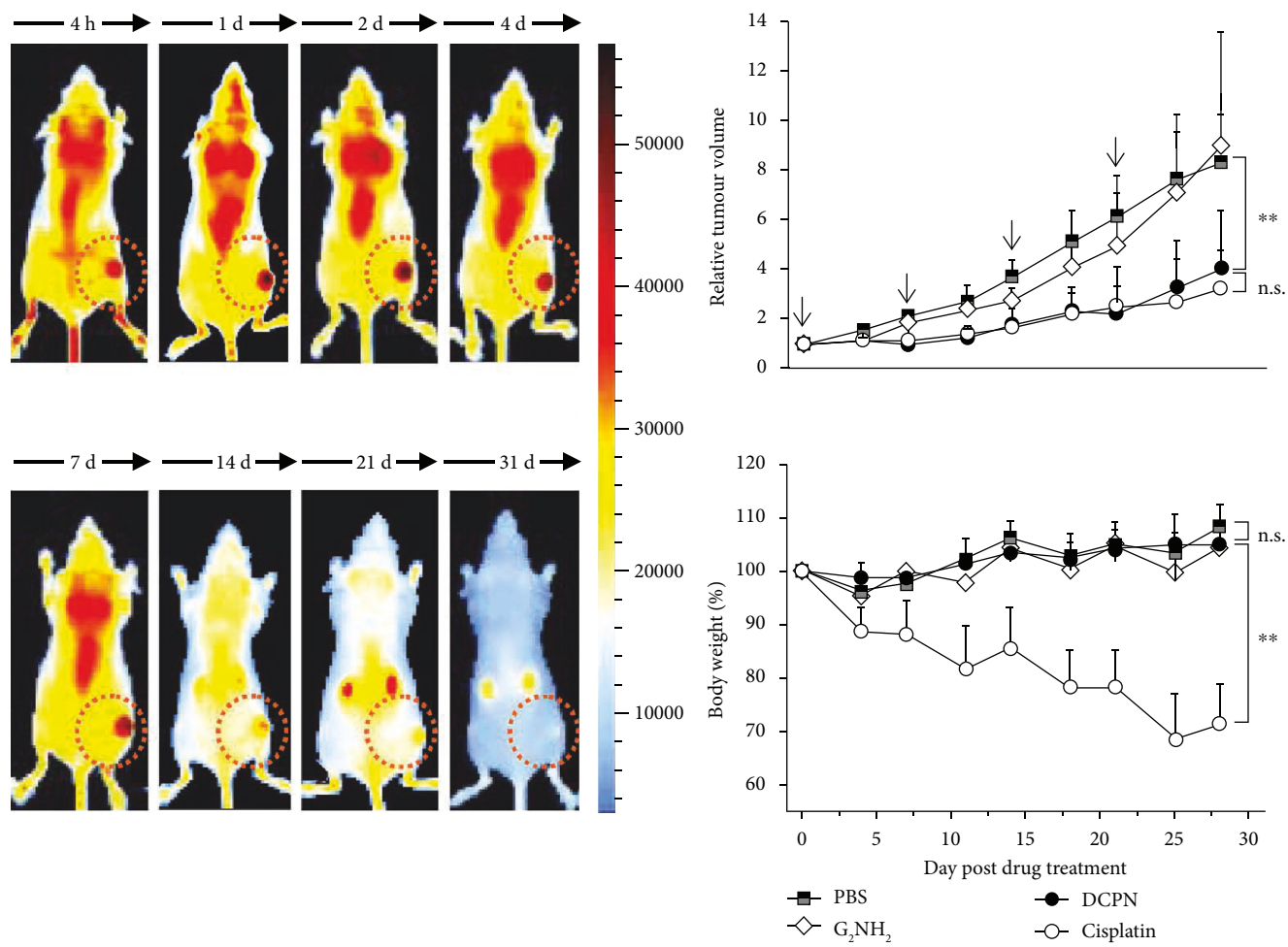

(c)

Figure 11: (a) Schematic route of fabricating caged Pt NCs (CPN) and the endocytosis pathway of CPN after conjugated with a tumour-penetrating peptide and PEG corona to form double-caged Pt NCs (DCPN). (b) Relative tumour volume and photographs of tumour size at the end point; the apoptotic cell death was detected by TUNEL assay after treated by CPN, and the scale bar is 20 μm. (c) Tumour target imaging, relative tumour volume, and body weight of mice after IT and IV injection by DCPN (reprinted major modification with permission from [201], Copyright 2013, Wiley).

has extensive advantages such as effortless postprocessing and pure product [106]. Kawasaki's group proposed a surfactant-free synthetic approach to obtain Pt NCs consisting of 4 to 6 atoms with blue fluorescence in N,N-dimethylformamide (DMF) solution [107]. These NCs showed extreme stability against strong ionic and variable acid-alkali conditions. Subsequently, Duchesne and Zhang employed X-ray absorption near-edge spectroscopy (XANES) and extended X-ray absorption fine structure (EXAFS) techniques which revealed the details of surfactant-free-synthesized Pt NCs' local structure and oxidation states [108]. The local structure of Pt is primarily due to the changes in the metal-ligand coordination, not the Pt-Pt bonding. The oxidation of Pt species is a combination of Pt(IV) and Pt(0), indicating that nonmetallic Pt NCs are responsible for their fluorescent properties. Meanwhile, this surfactant-free method synthesized Pt NCs were used to sensitively sense the aqueous Fe^{3+} ion solution and the limit of detection was 4 ppm (15 μM) under the concentration range of Fe^{3+} ions from 0.007 to 0.530 mM [109].

3. Properties of Platinum Nanoclusters

The properties of Pt NCs are the consequence of their distinct electronic and structural properties, which have access to NC's size, morphology, and surface surroundings inseparably. Herein, we summarize the classical features of Pt NCs including optical properties, catalytic properties, and other properties.

3.1. Optical Properties. Optical properties benefit for offering an insight to understand the electronic and geometric structures of M NCs in depth [110]. The applications of M NCs strongly depend on their optical properties, and there are a lot of research reported the NCs' unique optical phenomenon such as steady-state absorption and fluorescence, temperature-dependent fluorescence, ultrafast fluorescence

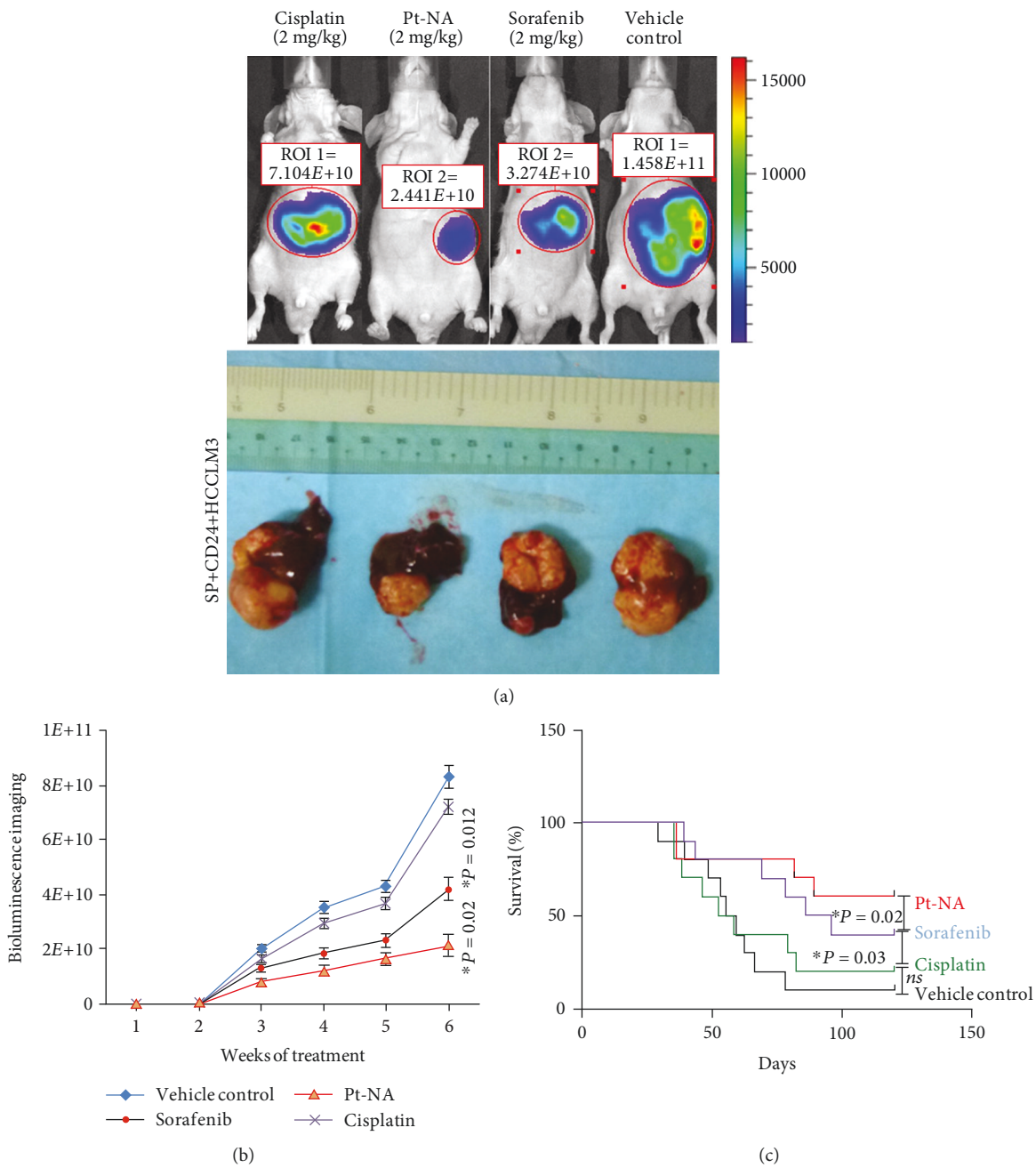

Figure 12: Continued.

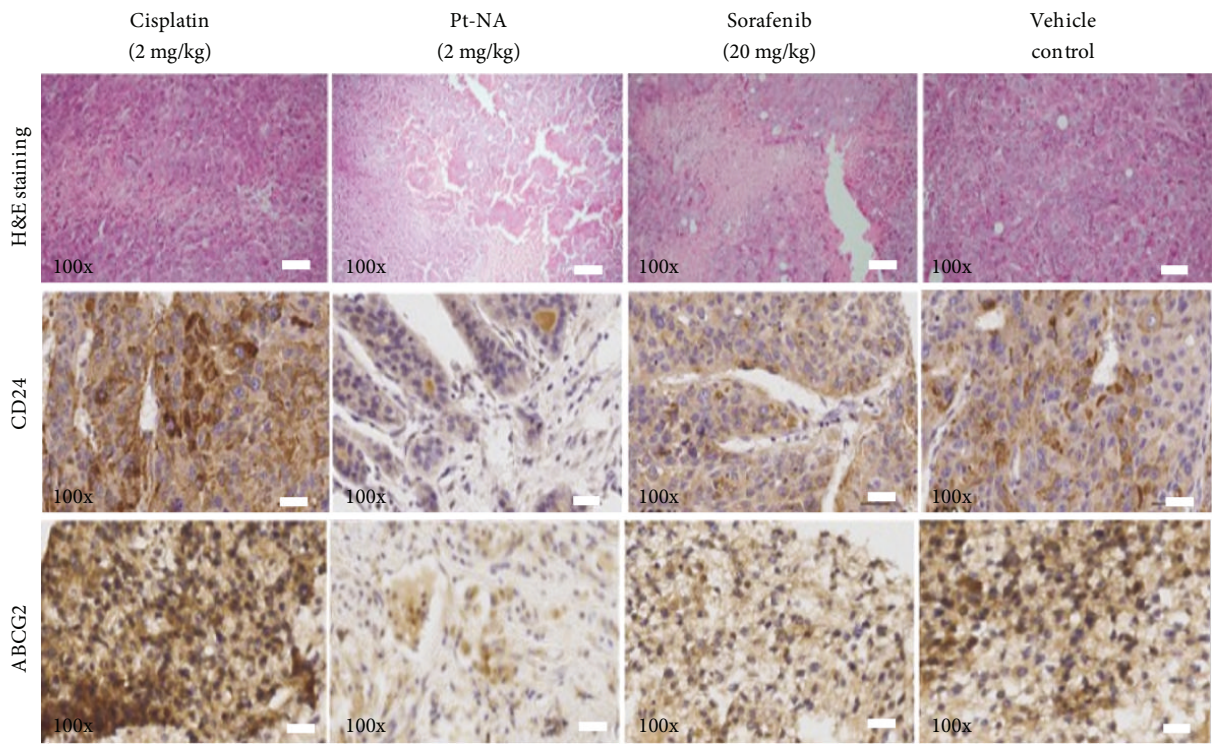

(d)

Figure 12: (a) Photographs of luminescence signals and the tumour-bearing livers of orthotopic tumour xenografts at the therapeutic end point for four treatment groups. The variation of (b) luminescence signals and (c) survival percentage of mice versus the time increasing. (d) Immunohistochemical staining for the expression of ABCG2 and CD24 in the tumours in four treatment groups; the scale bar is 100 μm (reprinted with permission from [203], Copyright 2016, American Chemical Society).

and transient absorption, fluorescence enhancement, and electrochemiluminescence [21, 111–113]. This part, we will introduce about the theoretical and practical progress of size-dependent fluorescence for Pt NCs.

Unlike M NPs which possess apparent surface plasmon resonance (SPR) absorption, Pt NCs lost this particular property, replaced by the size-dependent fluorescence ranging from the visible to near-infrared (NIR) region. Generally, this fluorescence of Pt NCs generated from the electronic transitions between the highest occupied molecular orbital (HOMO) and lowest unoccupied molecular orbital (LUMO). Their finite size is a critical point for molecule-like electronic transitions between HOMO and LUMO energy levels. Energy transitions can be expressed as Equation (1) based on the jellium model [3, 114]:

$$E_\delta = \frac{E_f}{N^{1/3}}, \tag{1}$$

where E_δ represents the energy level spacing, E_f is the Fermi energy, and N stands for the number of atoms in NCs. The E_f of free electron is only related to the metals' Wigner-Seitz radius (r_s) or the electron density (ρ_0) because the free electrons are piled up with constant electron density. Owing to N equals to $(R/r_s)^3$, Equation (1) transfers to Equation (2) using the emission/excitation frequency (ω_0) and NCs' radius (R) expressed as follows:

$$E_\delta = \hbar\omega_0 = \frac{E_f r_s}{R}. \tag{2}$$

Equation (2) is suitable for the M NCs when N is smaller than 20, which is well depicted by a spherical harmonic potential. Hamiltonian for an electron in a single-particle 3D harmonic oscillator can be described as follows:

$$H = -\frac{p^2}{2m} + \frac{m{\omega_0}^2 q^2}{2}, \tag{3}$$

where p represents the single-electron momentum and q is the coordinate operators. The small anharmonic distortion term should be taken into consideration under the condition of $N > 20$. Defining the distortion parameter (U) as a constant value (0.033), the correlated transition energy spacing (ΔE_{em}) is shown as Equation (4) using angular momentum (l) and shell number (n) expressed as follows:

$$\Delta E_{em} = \frac{E_f}{N^{1/3}}\left[1 - U\left({l_e}^2 - {l_g}^2 - \frac{n+2}{3}\right)\right], \tag{4}$$

where l_e represents the angular momentum of excited state and l_g is the angular momentum of ground state. Based on the Equations (2) ($N < 20$) and (4) ($N > 20$) displayed above,

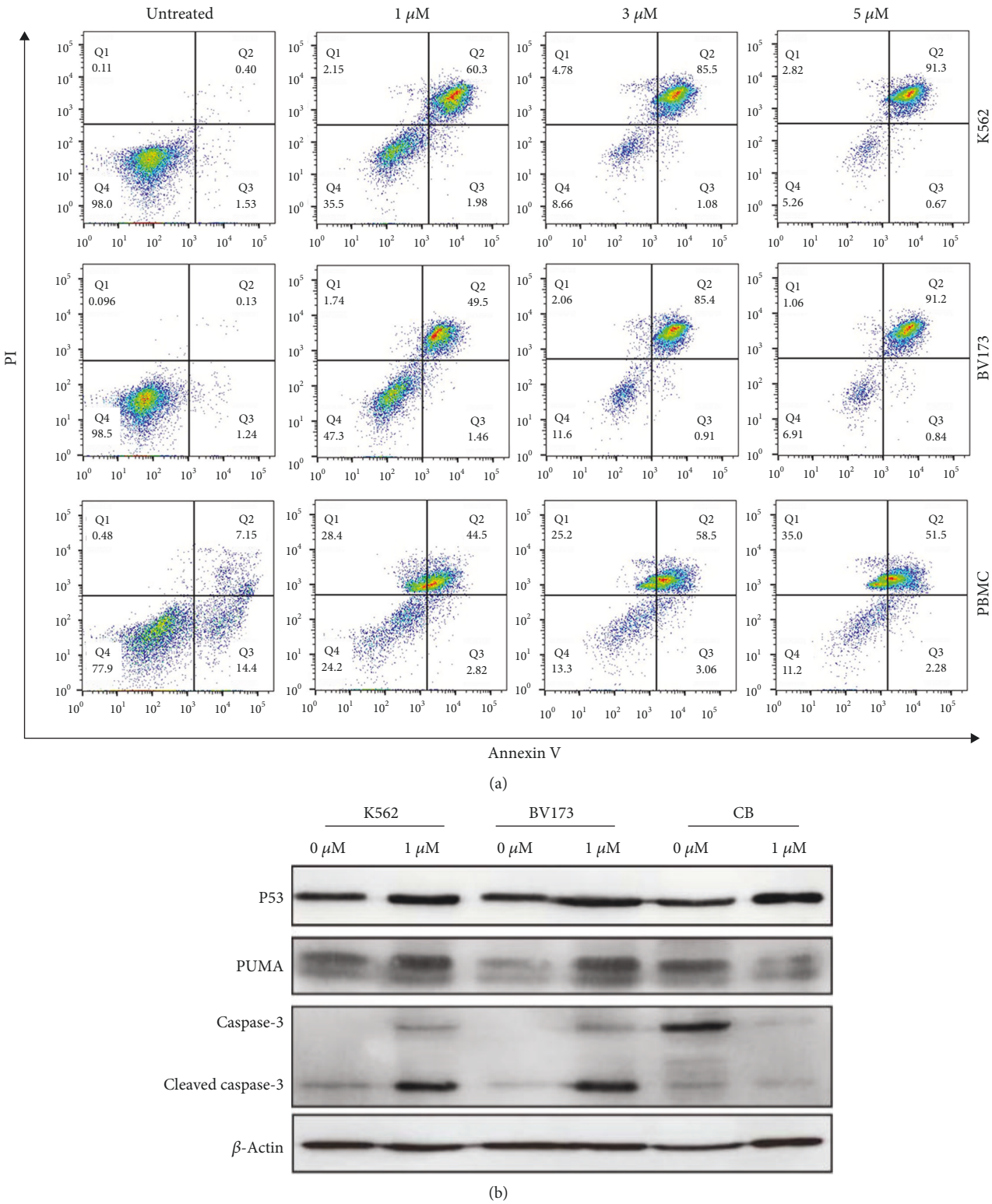

Figure 13: (a) The apoptosis in hematopoietic K562 and BV173 cancer cells and hematopoietic normal cell (PBMCs) induced by Pt NCs-based anticancer drugs after cultured for 4 h. (d) The west blotting assay result of three kinds of cells to detect protein expression of p53, PUMA, caspase-3, cleaved caspase-3, and β-actin, respectively (reprinted with permission from [186], Copyright 2018, Elsevier).

this dependency can be defined as the large size of M NCs is related to the small energy level spacing with longer emission wavelength fluorescence emitted and vice versa (Figure 4(a)).

Besides of the size-dependent fluorescence effect described above, surrounding ligands or templates also play a significant role on the fluorescent properties through ligand-metal charge

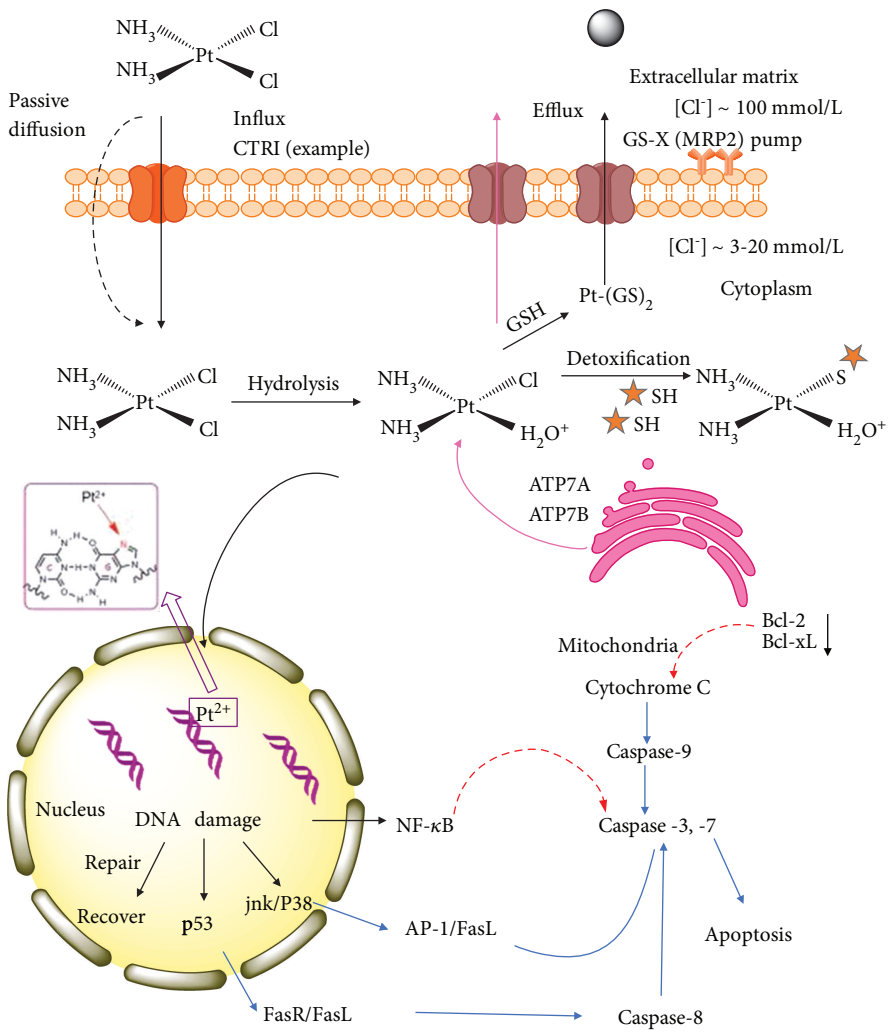

(a)

Figure 14: Continued.

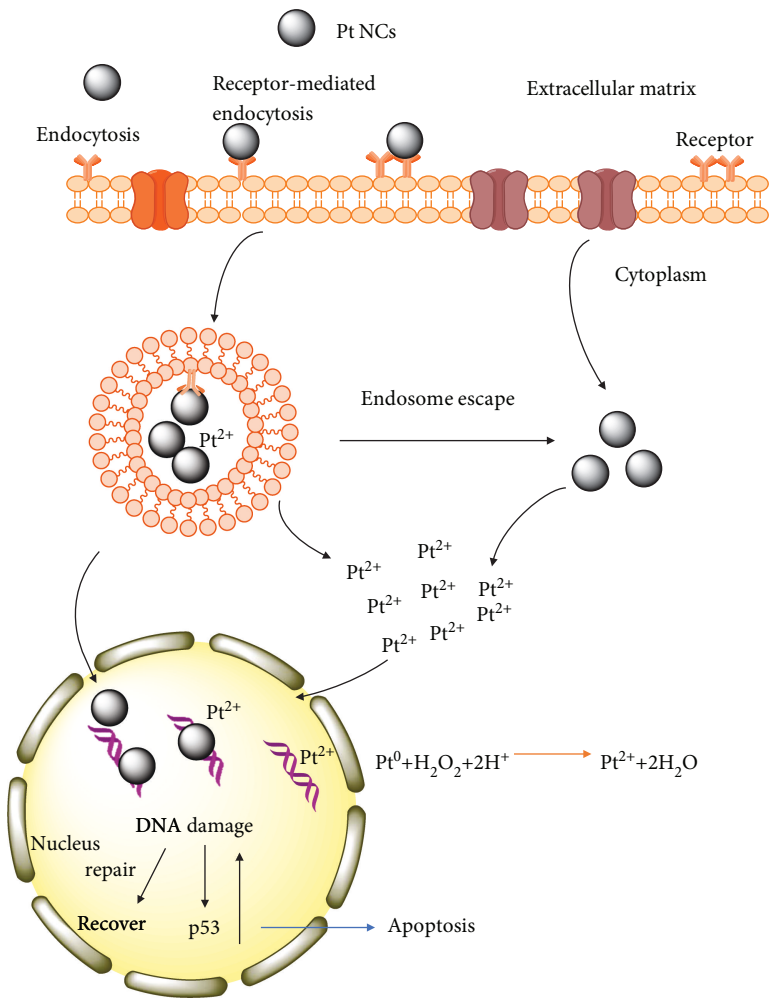

(b)

Figure 14: (a) Schematic apoptosis mechanism of cisplatin and inhibiting cisplatin-induced apoptosis. Red dotted line means that antiapoptotic factors counteract caspase activation. (b) Schematic apoptosis mechanism of Pt NCs. Abundant oxidized Pt ions and Pt NCs coordinate the DNA damage activating the p53 pathway (reprinted with permission from [204], Copyright 2017, Elsevier).

transfer (LMCT) (Figure 4(b)) [115–118]. Not only the enhancement or quenching of fluorescence could be realized by the collaboration between NCs and ligands but also the fluorescent intensity and maximum peak of emission wavelength can be adjusted. Thus, the mechanism of M NCs' fluorescence is ascribed to the intrinsic electronic transitions between HOMO-LUMO energy levels and the electronic transitions between NCs' surface and surrounding ligands *via* LMCT.

Until now, fluorescent Au and Ag NCs have been deeply researched and utilized in various fields [119–125]. As for the fluorescent Pt NCs, the number of synthetic methods, usable templates, and optical applications is significantly fewer than Au or Ag counterparts and most reports focused on the blue-, green-, and yellow-emitting fluorescence (Figure 5). The longer emission wavelength, especially near-infrared (NIR) region, is rarely mentioned. NIR fluorescence has a plenty of merits such as easy detection, less autofluorescence interference, and more use safety, making it attractive in both biological sensing and labelling analysis [126]. Furthermore, the fluorescent Pt NCs have the specific advantage than Ag and Au NCs, such as higher photoluminescence quantum yield (QY) and instinct properties like anticancer [127]. Therefore, great efforts payed out to study on the facile and repeatable synthesis of fluorescent Pt NCs with longer emission wavelength in the past decades.

Bovine serum albumin (BSA) supported blue fluorescent Pt NCs (emission wavelength region from 350 to 500 nm) which were fabricated by an easy $NaBH_4$-reduced method. These NCs could achieve the selective examination of hypochlorite among the concentration range from 12 to 240 mM *via* the visible fluorescence quenching due to the formation of oxidized Pt [128]. A GSH-induced etching process were employed to produce the yellow fluorescent Pt NCs (maximum emission wavelength at 570 nm) with the fluorescent QY at 17% [129]. Most Pt NCs are in the Pt(I) state, and the optimized molar ratio between Pt and GSH is determined at 1 : 10. Afterwards, blue [130] and green [131] fluorescent Pt NCs were precisely synthesized by employing the template of fourth-generation polyamidoamine dendrimer, short for PAMAM (G4-OH), and their absolute QYs reach to 18% and 28%

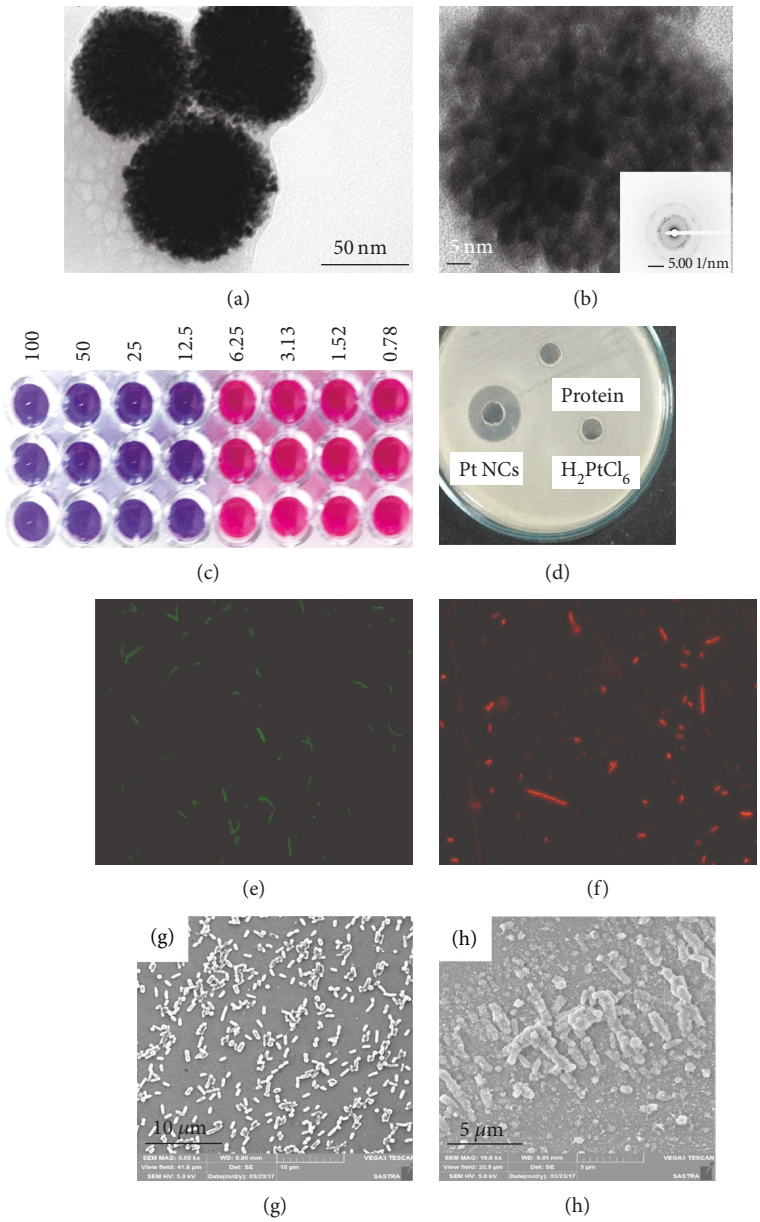

Figure 15: (a) TEM photograph of Pt NCs; the scale bar is 50 nm. (b) HR-TEM photograph shows that the NCs are formed *via* self-assembled NPs (scale bar is 5 nm). Inset corresponds the selected area electron diffraction (SAED) pattern. (c) MIC determination by resazurin microtiter plate assay (REMA) for Pt NCs towards Salmonella typhi and (d) zone of inhibition assay at MIC (12.5 μM). Fluorescence microscopy photographs of Salmonella typhi double stained with acridine orange (AO, membrane, green) and propidium iodide (PI, nucleic acid, red) for (e) untreated cells and (f) 12.5 μM Pt NCs treated. SEM photographs of (g) untreated cells and (h) 12.5 μM Pt NCs treated (reprinted major modification with permission from [206], Copyright 2018, Elsevier).

in water, respectively. We previously reported that various aqueous Pt NCs from blue to yellow fluorescence were prepared by a facile method using hyperbranched polyethyleneimine (PEI) as a stabilizing agent and environment-friendly L-ascorbic acid as a reductant [132]. Their optical properties can be tailored by adjusting the molar ratio between Pt ions and protecting ligands. Moreover, these Pt NCs have the ability of quantitative and selective detection for Co^{2+} ions and the limit of detection is up to 500 nM. Meanwhile, Xu et al. used the same method to prepared blue fluorescent Pt NCs and applied them for sensing nitroimidazoles (MTZ) with the limit concentration of 0.1 μM [133]. As for longer fluorescent emission, García's group demonstrated that red fluorescent Pt NCs in aqueous solution could be obtained by a chemical reduction method using lipoic acid (LA) as a capping agent [134]. The synthesized NCs with the maximum emission wavelength at 680 nm have a relatively high QY at 47% and present excellent stability towards pH media and high ionic solution. Moreover, hemoglobin-protected Pt NCs appeared to have two fluorescence regions: emission wavelength at 450 nm which is contributed by Pt_6 NCs at zero oxidation state and emission wavelength at 760 nm that is due to the formation of aggregated

Pt(II)-Hb complexes caused by LMCT effect from N/O to Pt atoms (the structure is assigned to Pt_{16} NCs) [135]. They also indicated that the NIR fluorescence is too weak to observe clearly because of a lower proportion of Pt(II) on the NC's surface (only near 13.68%). To our knowledge, it is the longest emission fluorescence reported for Pt NC materials, even for their poor fluorescent intensity.

In spite of the progress discussed above, the synthesis of fluorescent Pt NCs is still in its initial stage. There remains some challenge that needs to be solved, including the acquisition of highly longer emission fluorescent Pt NCs to realize the practice application, clarification of fluorescent mechanism to provide guidance, and large-scale production of Pt NCs to meet industrial demand.

3.2. Catalytic Properties. M NCs have been widely investigated for their catalytic properties from the theory to practical application [32, 136, 137]. Pt-based catalysts are pervasively applied in the development of the cost-effective proton exchange membrane fuel cells (PEMFCs) involving electrochimerical oxygen reduction reaction (ORR), methanol oxidation reaction (MOR), ethanol oxidation reaction (EOR) [138–142], and the catalysis of different chemical reactions like hydrogenation reactions [143–146]. It is well known that the catalytic reactivity of Pt varies by their sizes, morphology, and dispersion [147].

There are two common views for Pt-based catalysts. One is that Pt NPs (near 2 nm) are thought to be at the limit of their catalytic performance due to too strong Pt-O binding energy on the smaller clusters [148, 149]. That is to say, large Pt NPs with a face-centred-cubic (FCC) structure (near 2 to 3 nm) have the best activity and the ultrasmall Pt NCs are considered to have lower or even no catalytic ability, especially for ORR. However, a recent study rejected this traditional concept and their applicability [150]. It was found that Pt NCs with the size less than 2 nm also emerged a better catalytic performance. Accordingly, the catalytic capacity is no longer dependent on the size effect. Vajda et al. proved that small $Pt_{8\text{-}10}$ NCs loaded on a high-surface area template showed 40-100 times higher catalytic activity for the oxidative dehydrogenation than common Pt-based catalysts and extreme selectivity to produce the propylene [151]. Considering about the hydrogenation of methyl acrylate, the catalytic capacity of Pt-based materials depended on their size ranged from 2.4 to 3.0 nm which could be controlled by the amount of poly(N-vinyl-2-pyrrolidone) (PVP) [152]. Subsequently, Lan's group modified the counter electrode by PVP-protected Pt NCs for the dye-sensitized solar cell (DSSC) and found that this modified electrode exhibited light soaking durability and high conversion efficiency (near 9.37%) in a highly volatile electrolyte system [153]. Based on the results above, the "uniqueness of size effect" issue for Pt-based catalysts is now reexamined and no longer exist.

The other common view is that certain morphology of Pt NCs like topological magic number structure (e.g., Pt_{13} and Pt_{55}) with high symmetry could exhibit the higher catalytic ability [148, 154]. Imaoka et al. compared the ORR catalytic capacity between Pt_{12} NCs with less symmetric structure prepared using a phenylazomethine dendrimer with a tetraphenylmethane core (DPA-TPM) and Pt_{13} NCs with high symmetry obtained using phenylazomethine dendrimer with a triphenylpyridylmethane core (DPA-PyTPM) (Figure 6) [155]. One interesting finding is that misshapen structure Pt_{12} has a double catalytic activity compared with that of the topological stable Pt_{13} with the high symmetry. This distinction is mainly caused by two reasons: (1) less symmetric structure of Pt_{12} with a smaller number of internal Pt-Pt bonds and (2) structural transition of Pt_{12} makes the size further decreases against the smallest limit of icosahedral Pt_{13} NCs. Besides, this group further explored the atomicity-specific catalytic activity of Pt NCs within a significant small atomicity ($n < 20$), revealing Pt_{17} and Pt_{19} exhibited higher performance than other series [150]. As a result, the atomic coordination structure is completely different from that of the larger-sized FCC nanomaterial and the catalytic activities for the ORR are significantly altered by the spatial arrangement and atomicity. Hence, the fact discussed above proved the idea that the catalytic activity has weak access to the topological magic number of Pt on the nanoscale.

In summary, the emergence of Pt NCs has already reversed the traditional idea on Pt-based catalysts. The further investigations about the precise control of atomic number, seeking of different steric topological structures, and catalytic application of diverse chemical reactions need to be comprehensively and deeply studied in future.

3.3. Other Properties. Except for the optical and catalytic properties, Pt NCs also have unique physical characteristics, like thermal properties [156]. The phase stability of Pt_n NCs ($n = 38$, 147, 309, and 561 atoms) under various temperature conditions was surveyed by the molecular dynamics (MD) simulation combined with an embedded atom scheme (EAM) [157]. Furthermore, Akbarzadeh and Parsafar discussed the melting and thermal physical properties of Pt_n NCs in a larger size ($n = 256$ to 8788 atoms) by means of molecular dynamics simulations employing quantum Sutton-Chen (QSC) potential [158]. Both for the larger and relative smaller NCs, the melting temperature goes up as the NCs' size increased and that of Pt_{8788} NCs approaches to the Pt bulk limit.

4. Biological Applications of Platinum Nanoclusters

Pt NCs consisting of few to tens of atoms own plenty of outstanding features and possess a great potential in the various applications, e.g., catalysis [159], sensing [133], and cancer therapy [160]. This part, we focus on the Pt NCs' biological applications which are strongly in accordance with their size-dependent effects and the coordination between NCs and functional surrounding ligands.

4.1. Biological Imaging. In the past decades, fluorescent biological imaging technology which is the process of light emission in living organisms [161] became an indispensable and visualized tool for the drug delivery system [162, 163], gene therapy [164], and cancer diagnoses [165, 166]. The used fluorophore is a key point for successful bioimaging of cells,

which concerns about their safety, sensitivity, and wide applicability. Organic dyes [167–169], semiconductor quantum dots (QDots) [170, 171], fluorescent proteins [172, 173], lanthanides [174, 175], and carbon dots (CDots) [176, 177] as the common fluorophores have been already explored for practical imaging and extensively presented their merits and drawbacks. For example, organic dyes possess the high fluorescence QY; however, the dramatic cytotoxicity severely handicaps their practical applications [178]. Besides, QDots have unique features such as tunable colours, great photostability, narrow emission spectra, and broad excitation spectra [179]. The disadvantages like large size (>3 nm), on-and-off blinking behaviour, and low biocompatibility are important issues that need to be solved [180, 181]. As an alternative to organic dyes and QDots, M NCs have a crowd of strike features like ultrasmall size, water solubility, high fluorescent efficiency, large Stokes shifts, excellent photostability, and low cytotoxicity [182], making them become the safe and nontoxic clinical fluorescent contrast agents. In comparison to well-studied Au and Ag NCs [31, 183–185], relatively little research investigated the bioimaging application of fluorescent Pt NCs. In general, the imaging way of Pt NCs can be divided into two parts: (1) direct labelling without any other materials and (2) combination of certain biomolecule (e.g., proteins and DNA) to targeted imaging. Our previous work reported that fluorescent Pt NCs stabilized by polyamine ligands (average size near 1.4 nm) could accomplish the biostaining of the suspension hematopoietic cell system [186]. The ligand-capped Pt NCs could selectively enter into K562 and BV173 cancer cells compared to the normal peripheral blood mononucleated cells (PBMCs) from healthy donors (Figure 7). This distinction gives an opportunity to achieve the specific labelling of hematopoietic cells during the disease diagnosis. Recently, we extended this fluorescent probe to label the lung cancer [187]. The classical human lung adenocarcinoma cells were chosen to examine their biological imaging ability (Figure 8). Both A549 (normal cells) and A549/DDP (cisplatin-resistant cells) cells exhibit the red fluorescence signal that is emitted from Pt NCs-based drugs, while the cell nuclei are stained by 4′,6-diamidino-2-phenylindole (DAPI) exhibiting the blue fluorescence. Most interesting finding is that Pt NCs preferably enter almost cell nuclei in the cisplatin-resistant A549/DDP cell groups, compared to the A549 cell group where the Pt NCs are observed evenly distributed in both cell nuclei and cytoplasm. As a result, Pt NC nanomaterial could realize the visual imaging individually as a fluorophore on the account of the fluorescence effect.

The aim of conjugating the biomolecule is to achieve the deliberate target of the specific tissue. Antibody is a suitable and effective choice. An antibody belonging to proteins has a lot of functional groups (e.g., -NH_2 and -COOH) which could feasibly react with those groups on the surrounding ligands of NCs by chemical reaction, and then, the presynthesized Pt NC-antibody complex is delivered to express on the certain targeted position *via* antigen-antibody reaction. This approach could complete the targeted imaging of lesion location. For example, after bounding to the antichemokine receptor antibody (anti-CXCR4-Ab) through a conjugated protein A, blue fluorescent mercaptoacetic acid-(MAA-) capped Pt NCs were observed on the cell membranes where the receptors are expressed (Figure 9) [130]. In order to check this specific combination of antibody-modified $Pt_5(MAA)_8$-protein A-anti-CXCR4-Ab complex and chemokine receptor, Chinese hamster ovary (CHO-K1) cells were selected as a control group due to their negative behaviours against the chemokine receptor. The result indicated that the Pt NC complex cannot stain the CHO-K1 cells, proving the success in the targeted imaging. Simultaneously, the same work was also done for green-emitting Pt NCs [131]. Most importantly, these reported that Pt NCs have the considerably low cytotoxicity and excellent biocompatibility, demonstrating enormous potential in the tracking, imaging, and labelling of cancer cells or other kinds of cells as an alternative fluorescently labelled probe.

Similarly, yellow fluorescent PEI-stabilized Pt NCs (Pt NCs@PEI) could effortlessly conjugate with an antichemokine receptor antibody and then successfully realized the double staining of HeLa cells using DAPI-stained nuclei and Pt NCs@PEI expressed on the cell membrane (Figure 10) [188]. To achieve targeted expression on the cell membrane, a simple glutaraldehyde method was used to conjugate Pt NCs@PEI to the anti-CXCR4-Ab. Confocal fluorescence images show HeLa cell nuclei in blue color (DAPI stained) and cell membranes as yellow color, demonstrating the evidence that the usage of Pt NCs@PEI will not be affected by any other fluorophores, simultaneously. Furthermore, the relationship between NCs and PEI ligands was also checked and the results elucidate that these Pt NCs are stabilized mostly by primary amine. Based on this discovery, the fluorescence of Pt NCs may be originated *via* two pathways, that is, the electronic transitions between HOMO-LUMO energy levels of Pt NCs and the NCs' surface surrounding ligands through LMCT.

4.2. Antitumour Drugs. Pt-based antitumour drugs are one of the most effective tools for the treatment of different tumours, and Food and Drug Administration (FDA) authorized the Pt as the effective antitumour drugs for various cancer therapies in 1978 [127, 189–192]. Cisplatin in the Pt(II) state as a representative drug emerged a few deficiencies which influences the therapeutic efficiency. For instance, it could have side effect like myelosuppression, nephrotoxicity, and neurotoxicity in the course of medicine treatment [193–195]. On the other hand, typical breast, colorectal, and prostate cancers exhibit less sensitive to cisplatin [196, 197]. More serious is that testicular and ovarian cancers intrinsically resist to cisplatin treatment after several cycles of therapy, even though it is efficient at the beginning stage [198]. These drawbacks including the systemic toxicities and poor specificity impede their anticancer efficiency; therefore, developing a new-type Pt-based antitumour drug with little side effect and excellent specificity could afford a powerful supporting technique for diagnosis and treatment of diverse malignant tumours.

In the current years, Pt NPs and NCs have been used to develop the latest Pt-based anticancer nanomedicine and found their preferable ability of inducing the apoptosis of

several cancer diseases [160, 199, 200]. Chien et al. reported a low-generation dendrimer-caged Pt NCs (CPN) with 0.93 nm diameter [201]. After attaching to the cleavable polyethylene glycol (PEG) corona and targetable iRGD (CRGDKGPDC), this complex achieved the targeting of human breast cancer cell line MDA-MB-231 and release of toxins against malignant cells by affecting tumour-inside activation for anticancer chemotherapeutics (Figure 11). By means of subcutaneous breast cancer xenograft in mice, the therapeutic effect of CPN was examined *via* intratumoural injection in *vivo* and the result indicated that this kind of chemotherapeutics has the same efficacy compared to cisplatin.

Fluorescent GSH-capped Pt NCs were prepared by a green and simple chemical method and employed to biolabel the HepG2 cells [202]. It is worth noting that the synthesized Pt NCs could obviously kill the HeLa cells under the irradiation by infrared (IR) light, while it was not happened under UV light condition. The killing mechanism of cancer cells is contributed to heating effect instead of free radical effect. Xia et al. presented an approach to package the Pt NCs with polypeptide and targeting peptide SP9443 to form the assembled Pt NAs. These Pt NAs could damage DNA through targeting disseminated hepatocellular carcinoma (HCC) tumour-initiating cancer stem-like cells (CSLCs) to achieve inhibiting proliferation of tumours [203]. Gene expression profile analysis proved that ABCG2 and CD24, which expressed highly in the sorted SP+CD24+ cells, could be adjusted by Pt NAs, while the cisplatin could not downregulate. Furthermore, real-time quantitative polymerase chain reaction (RT-qPCR) analysis also demonstrated that Pt NAs induced the downregulation of CCNB1, CDK1, and TOP2A, leading to DNA damage and modulation of the cell cycle (Figure 12). This study verified that the prepared ultrafine Pt NAs have the ability to accelerate the release of toxic Pt ions and overcome the cisplatin-resistant problem for HCC CLSCs.

In a previous study, we used the dual-functional Pt NCs-based anticancer materials to biologically image the blood system suspension cells as the fluorescent markers. Meanwhile, the selective inhibition of hematopoietic K562 and BV173 cancer cells was investigated as well [186]. The relative cell apoptotic rate for K562 and BV173 cancer cells is three times higher than hematopoietic normal cell (PBMCs) *via* induction of the expression of p53, PUMA, and cleaved caspase-3 proteins (Figure 13). These Pt NCs manifest the evident apoptosis efficacy possibly due to the inherent characteristic of Pt and exhibit a great potential in effective treatment of hematopoietic system disease, especially acute myeloid leukaemia and lymphoma. Currently, the cisplatin-resistant-non-small-cell lung cancer (NSCLC) was chosen as the targeted object because the lung cancer incidence is increasing continually owing to the environment deterioration and smoking. The problem of drug resistance seriously affects the chemotherapy efficiency and survival rate of patients during the treatment with chemotherapy drugs due to multiple mechanism, such as the lack of effective drug concentration in tumour cells, reduction of drug activity, cell apoptosis changes, and DNA repair pathways. The experimental results illustrated that Pt NCs-based anticancer drug could achieve the excellent induced apoptosis in both cisplatin-resistant A549/DDP and non-cisplatin-resistant A549 cells [187]. More interesting is that cisplatin-resistant A549/DDP showed the superior inhibitory and apoptotic effects than non-cisplatin-resistant A549 cells by the way of activating p53 protein and the related signalling pathway, which could be proved through the apparent endocytosis behaviour by the nucleus of cisplatin-resistant A549/DDP cells. As for NSCLC, the synthesized Pt NCs-based anticancer drugs could overcome the toxic side effects and drug resistance to enhance the clinical therapeutic effect.

In contrast to the well-known cisplatin resistance mechanism concerning about antiapoptotic factors that counteract caspase activation (Figure 14(a)), the mechanism for Pt NCs-based nanomedicine is still inconclusive. Some researches assume that ultrafine Pt subnanomaterials possess extreme tiny size approximately 1 nm, leading to near 90% of Pt atoms exposed on the NC's surface. This kind of high surface-active Pt NCs is affected by intracellular acidic organelles like endosomes and lysosomes and then rapidly decomposed to form oxidation states of Pt (Figure 14(b)) [204]. These corrosive Pt trends to combine with DNA or proteins and then destroy the DNA consequently, resulting in the apoptosis of cancer cells. In addition, ultrafine Pt NCs have an ability to anchor onto the grooves of DNA double helix to further damage the DNA. Thus, the reasonable and receivable mechanism for the Pt NCs-based chemotherapeutics may be summarized as the synergistic effect of both Pt NCs and Pt ions causing the damage of DNA to kill the cancer cells.

4.3. Antibacteria. The usage of noble metal (Ag and Au) as antimicrobial agents was largely investigated, especially for Ag-based nanomaterials [205]. The mechanisms of antibacteria are related to the DNA damage, membrane damage, and production of some active radicals (e.g., reactive oxygen species (ROS)). Because of the ultrafine size of NCs, Ag NCs with higher surface-to-volume ratios and abundant surface atoms express higher antimicrobial efficiency. However, the antibacterial feature of Pt NCs is rarely studied. Subramaniyan et al. put forward the green synthesis protocol employing phytoprotein obtained from spinach leaves as a ligand to gain spherical Pt NCs with the average size of 5 nm and self-assembled species at the size range from 100 to 250 nm [206]. These protein-stabilized Pt NCs have the excellent Salmonella typhi-inhibiting ability, and the minimum inhibitory concentration (MIC) was determined at 12.5 μM (Figure 15). The inhibition effect was proved as the damage of established biofilms, confirmed by scanning electron microscopy (SEM) and fluorescence microscopy. Moreover, intracellular ROS generated by Pt NCs was also the ancillary killer to Salmonella typhi *via* oxidative injury against the antioxidant defence.

5. Conclusions and Outlook

Conclusively, Pt NCs containing few to dozens of atoms exhibit unique physicochemical properties due to their molecule-like behaviours such as discrete electronic state

and size-dependent fluorescence. The synthesis of Pt NCs can be divided into two ways: template-assisted approach that is related to designed properties, controllable size, and specific morphology and template-free protocol which has access to the feasible posttreatment process and pure product. Subsequently, the optical, catalytic, and thermal properties of Pt NCs were introduced and these features have a strong relationship with the distinct electronic and structural characteristics, as well as the various surrounding ligands. Breaking the traditional concepts, ultrafine Pt NCs exhibit the favourable catalytic abilities even in the form of less symmetric topological structure. Most importantly, the diverse biological applications of Pt NCs were summarized in detail. Fluorescent Pt NCs have already bioimaged different kinds of tumours like HeLa cells, hematopoietic K569 and BV173 cells, NSCLC A549 cells, and HepG2 cells, as a preferred fluorophore in contrast to traditional fluorescent labels. Moreover, Pt NCs were employed as new class chemotherapeutics in the diagnoses and treatment of hematopoietic, lung, and hepatocellular malignant tumours, exhibiting excellent therapy effect, especially overcoming the problem of cisplatin resistance. Finally, Pt NCs were identified to possess a good antibacterial capacity which could be used as an alternative of the Ag antibacterial material.

Despite these exciting and promising progress of Pt NCs mentioned above, the study of ultrafine Pt NCs is at the beginning stage and there still remains a great challenge as follows: (1) synthesis of NIR fluorescent Pt NCs with outstanding optical features, (2) evident clarification of the apoptosis pathway and mechanism of Pt NCs for hematopoietic tumour and cisplatin-resistant NSCLC, (3) valid combination of Pt NCs with other materials to endow multifunctionality, and (4) comprehensive utilization of Pt NCs in diverse biological applications, not only for the different tissue systems (like osteocarcinoma and pancreatic carcinoma) but also the application types that need to be extended such as gene therapy, DNA sensing, and protein detection.

Conflicts of Interest

The authors declare that there is no conflict of interest regarding the publication of this paper.

Acknowledgments

This research was funded by the National Natural Science Foundation of China (21807121), Key Scientific Research Projects of High Education of Henan Province (18A430005), and Project for Fundamental Research Funds of Zhongyuan University of Technology (K2018YY020). Dr. X.H. gratefully acknowledges the Collaborative Innovation Centre of Textile and Garment Industry, Henan Province, for their assistance and the support from the 2019 Youth Talents Promotion Project of Henan Province, the 2018 Backbone Teachers of Zhongyuan University of Technology, and the Program for Interdisciplinary Direction Team in Zhongyuan University of Technology, China.

References

[1] W. P. Griffith, *The Chemistry of the Rarer Platinum Metals (Os, Ru, Ir, and Rh)*, Interscience Publishers, 1967.

[2] F. R. Hartley, *The Chemistry of Platinum and Palladium: With Particular Reference to Complexes of the Elements*, Applied Science Publishers Ltd., 1973.

[3] X. Huang, *Polymer Ligand Stabilized Fluorescent Platinum Nanoclusters: Synthesis, Characterization, and Their Applications*, Osaka University, 2016.

[4] R. W. Siegel, "Nanostructured materials -mind over matter," *Nanostructured Materials*, vol. 4, no. 1, pp. 121–138, 1994.

[5] P. C. Ray, "Size and shape dependent second order nonlinear optical properties of nanomaterials and their application in biological and chemical sensing," *Chemical Reviews*, vol. 110, no. 9, pp. 5332–5365, 2010.

[6] X. Jiang, B. Du, Y. Huang, and J. Zheng, "Ultrasmall noble metal nanoparticles: breakthroughs and biomedical implications," *Nano Today*, vol. 21, pp. 106–125, 2018.

[7] G. Mie, "Beiträge zur optik trüber medien, speziell kolloidaler metallösungen (Contributions to the optics of diffuse media, especially colloid metal solutions)," *Annals of Physics*, vol. 330, no. 3, pp. 377–445, 1908.

[8] P. K. Jain, X. Huang, I. H. El-Sayed, and M. A. El-Sayed, "Noble metals on the nanoscale: optical and photothermal properties and some applications in imaging, sensing, biology, and medicine," *Accounts of Chemical Research*, vol. 41, no. 12, pp. 1578–1586, 2008.

[9] M. Faraday, "XLVII. *Experimental relations of gold (and other metals) to light. – The Bakerian lecture*," *The London, Edinburgh, and Dublin Philosophical Magazine and Journal of Science*, vol. 14, no. 95, pp. 401–417, 1857.

[10] H. Kang, J. T. Buchman, R. S. Rodriguez et al., "Stabilization of silver and gold nanoparticles: preservation and improvement of plasmonic functionalities," *Chemical Reviews*, vol. 119, no. 1, pp. 664–699, 2019.

[11] A. Amirjani and D. F. Haghshenas, "Ag nanostructures as the surface plasmon resonance (SPR)?based sensors: a mechanistic study with an emphasis on heavy metallic ions detection," *Sensors and Actuators B: Chemical*, vol. 273, pp. 1768–1779, 2018.

[12] M. M. Alvarez, J. T. Khoury, T. G. Schaaff, M. N. Shafigullin, I. Vezmar, and R. L. Whetten, "Optical absorption spectra of nanocrystal gold molecules," *The Journal of Physical Chemistry B*, vol. 101, no. 19, pp. 3706–3712, 1997.

[13] S. K. Ghosh and T. Pal, "Interparticle coupling effect on the surface plasmon resonance of gold nanoparticles: from theory to applications," *Chemical Reviews*, vol. 107, no. 11, pp. 4797–4862, 2007.

[14] E. Konował, A. Modrzejewska-Sikorska, M. Motylenko et al., "Functionalization of organically modified silica with gold nanoparticles in the presence of lignosulfonate," *International Journal of Biological Macromolecules*, vol. 85, pp. 74–81, 2016.

[15] A. Modrzejewska-Sikorska, E. Konował, A. Cichy, M. Nowicki, T. Jesionowski, and G. Milczarek, "The effect of silver salts and lignosulfonates in the synthesis of lignosulfonate-stabilized silver nanoparticles," *Journal of Molecular Liquids*, vol. 240, pp. 80–86, 2017.

[16] Q. Tong, W. Wang, Y. Fan, and L. Dong, "Recent progressive preparations and applications of silver-based SERS substrates,"

TrAC Trends in Analytical Chemistry, vol. 106, pp. 246–258, 2018.

[17] G. Schmid, "Large clusters and colloids. Metals in the embryonic state," *Chemical Reviews*, vol. 92, no. 8, pp. 1709–1727, 1992.

[18] F. A. Cotton and T. E. Haas, "A molecular orbital treatment of the bonding in certain metal atom clusters," *Inorganic Chemistry*, vol. 3, no. 1, pp. 10–17, 1964.

[19] L. Yu, L. Zhang, G. Ren et al., "Multicolorful fluorescent-nanoprobe composed of Au nanocluster and carbon dots for colorimetric and fluorescent sensing Hg^{2+} and Cr^{6+}," *Sensors and Actuators B: Chemical*, vol. 262, pp. 678–686, 2018.

[20] M. I. Halawa, J. Lai, and G. Xu, "Gold nanoclusters: synthetic strategies and recent advances in fluorescent sensing," *Materials Today Nano*, vol. 3, pp. 9–27, 2018.

[21] H. Yu, B. Rao, W. Jiang, S. Yang, and M. Zhu, "The photoluminescent metal nanoclusters with atomic precision," *Coordination Chemistry Reviews*, vol. 378, pp. 595–617, 2019.

[22] R. Jin, "Atomically precise metal nanoclusters: stable sizes and optical properties," *Nanoscale*, vol. 7, no. 5, pp. 1549–1565, 2015.

[23] R. Jin, C. Zeng, M. Zhou, and Y. Chen, "Atomically precise colloidal metal nanoclusters and nanoparticles: fundamentals and opportunities," *Chemical Reviews*, vol. 116, no. 18, pp. 10346–10413, 2016.

[24] T.-H. Lee, J. I. Gonzalez, J. Zheng, and R. M. Dickson, "Single-molecule optoelectronics," *Accounts of Chemical Research*, vol. 38, no. 7, pp. 534–541, 2005.

[25] S. Morawiec, M. J. Mendes, F. Priolo, and I. Crupi, "Plasmonic nanostructures for light trapping in thin-film solar cells," *Materials Science in Semiconductor Processing*, vol. 92, pp. 10–18, 2019.

[26] F. Lu, H. Yang, Z. Yuan, T. Nakanishi, C. Lu, and Y. He, "Highly fluorescent polyethyleneimine protected Au_8 nanoclusters: one-pot synthesis and application in hemoglobin detection," *Sensors and Actuators B: Chemical*, vol. 291, pp. 170–176, 2019.

[27] N. Xiao, J. X. Dong, S. G. Liu et al., "Multifunctional fluorescent sensors for independent detection of multiple metal ions based on Ag nanoclusters," *Sensors and Actuators B: Chemical*, vol. 264, pp. 184–192, 2018.

[28] S. Ghosh, J. R. Bhamore, N. I. Malek, Z. V. P. Murthy, and S. K. Kailasa, "Trypsin mediated one-pot reaction for the synthesis of red fluorescent gold nanoclusters: sensing of multiple analytes (carbidopa, dopamine, Cu^{2+}, Co^{2+} and Hg^{2+} ions)," *Spectrochimica Acta Part A: Molecular and Biomolecular Spectroscopy*, vol. 215, pp. 209–217, 2019.

[29] X. Y. Wang, G. B. Zhu, W. D. Cao et al., "A novel ratiometric fluorescent probe for the detection of uric acid in human blood based on H_2O_2-mediated fluorescence quenching of gold/silver nanoclusters," *Talanta*, vol. 191, pp. 46–53, 2019.

[30] J. D. Aiken III and R. G. Finke, "A review of modern transition-metal nanoclusters: their synthesis, characterization, and applications in catalysis," *Journal of Molecular Catalysis A: Chemical*, vol. 145, no. 1–2, pp. 1–44, 1999.

[31] Y. Zhang, C. Zhang, C. Xu et al., "Ultrasmall Au nanoclusters for biomedical and biosensing applications: a mini-review," *Talanta*, vol. 200, pp. 432–442, 2019.

[32] L. N. Lewis, "Chemical catalysis by colloids and clusters," *Chemical Reviews*, vol. 93, no. 8, pp. 2693–2730, 1993.

[33] J. Wu and H. Yang, "Platinum-based oxygen reduction electrocatalysts," *Accounts of Chemical Research*, vol. 46, no. 8, pp. 1848–1857, 2013.

[34] Z. Peng and H. Yang, "Designer platinum nanoparticles: control of shape, composition in alloy, nanostructure and electrocatalytic property," *Nano Today*, vol. 4, no. 2, pp. 143–164, 2009.

[35] H. Xiao, L. Yan, E. M. Dempsey et al., "Recent progress in polymer-based platinum drug delivery systems," *Progress in Polymer Science*, vol. 87, pp. 70–106, 2018.

[36] A. V. Klein and T. W. Hambley, "Platinum drug distribution in cancer cells and tumors," *Chemical Reviews*, vol. 109, no. 10, pp. 4911–4920, 2009.

[37] A. Chen and P. Holt-Hindle, "Platinum-based nanostructured materials: synthesis, properties, and applications," *Chemical Reviews*, vol. 110, no. 6, pp. 3767–3804, 2010.

[38] R. Jin, "Quantum sized, thiolate-protected gold nanoclusters," *Nanoscale*, vol. 2, no. 3, pp. 343–362, 2010.

[39] Y. Wang, H. Guo, Y. Zhang et al., "Achieving highly water-soluble and luminescent gold nanoclusters modified by β–cyclodextrin as multifunctional nanoprobe for biological applications," *Dyes and Pigments*, vol. 157, pp. 359–368, 2018.

[40] I. Diez and R. H. A. Ras, "Fluorescent silver nanoclusters," *Nanoscale*, vol. 3, no. 5, pp. 1963–1970, 2011.

[41] C.-H. Lu and F.-C. Chang, "Polyhedral oligomeric silsesquioxane-encapsulating amorphous palladium nanoclusters as catalysts for heck reactions," *ACS Catalysis*, vol. 1, no. 5, pp. 481–488, 2011.

[42] X. Liu and D. Astruc, "Atomically precise copper nanoclusters and their applications," *Coordination Chemistry Reviews*, vol. 359, pp. 112–126, 2018.

[43] Q. Yao, T. Chen, X. Yuan, and J. Xie, "Toward total synthesis of thiolate-protected metal nanoclusters," *Accounts of Chemical Research*, vol. 51, no. 6, pp. 1338–1348, 2018.

[44] B. Helmut and S. Nagabhushana Kyatanahalli, "Chapter 2 - metal nanoclusters: synthesis and strategies for their size control," in *Metal nanoclusters in catalysis and materials science: the issue of size control*, pp. 21–48, Elsevier, 2008.

[45] O. Kylián, J. Prokeš, O. Polonskyi et al., "Deposition and characterization of Pt nanocluster films by means of gas aggregation cluster source," *Thin Solid Films*, vol. 571, pp. 13–17, 2014.

[46] K. Sokołowska, S. Malola, M. Lahtinen et al., "Towards controlled synthesis of water-soluble gold nanoclusters: synthesis and analysis," *Journal of Physical Chemistry C*, vol. 123, no. 4, pp. 2602–2612, 2019.

[47] S. W. Cho, H. J. Kim, Y. N. Cho, J. H. Jeong, and H. Kong, "Top-down synthesis of polyaspartamide morphogens to derive platinum nanoclusters," *Materials Letters*, vol. 168, pp. 184–187, 2016.

[48] R. R. Nasaruddin, T. Chen, N. Yan, and J. Xie, "Roles of thiolate ligands in the synthesis, properties and catalytic application of gold nanoclusters," *Coordination Chemistry Reviews*, vol. 368, pp. 60–79, 2018.

[49] W. W. Weare, S. M. Reed, M. G. Warner, and J. E. Hutchison, "Improved synthesis of small ($d_{\mathrm{CORE}} \approx 1.5$ nm) phosphine-stabilized gold nanoparticles," *Journal of the American Chemical Society*, vol. 122, no. 51, pp. 12890-12891, 2000.

[50] Ö. Metin, S. Duman, M. Dinç, and S. Özkar, "Oleylamine-stabilized palladium(0) nanoclusters as highly active

heterogeneous catalyst for the dehydrogenation of ammonia borane," *The Journal of Physical Chemistry C*, vol. 115, no. 21, pp. 10736–10743, 2011.

[51] J. Xu, X. Wu, G. Fu et al., "Fabrication of phosphonate functionalized platinum nanoclusters and their application in hydrogen peroxide sensing in the presence of oxygen," *Electrochimica Acta*, vol. 80, pp. 233–239, 2012.

[52] J. Ma, S. Reng, D. Pan, R. Li, and K. Xie, "PVP-Pt nanoclusters supported zeolite catalysts for converting methane to higher hydrocarbon at low temperature," *Reactive and Functional Polymers*, vol. 62, no. 1, pp. 31–39, 2005.

[53] I. Díez, M. Pusa, S. Kulmala et al., "Color tunability and electrochemiluminescence of silver nanoclusters," *Angewandte Chemie International Edition*, vol. 48, no. 12, pp. 2122–2125, 2009.

[54] R. M. Crooks, B. I. Lemon, L. Sun, L. K. Yeung, and M. Zhao, "Dendrimer-encapsulated metals and semiconductors: synthesis, characterization, and applications," in *Dendrimers III*, F. Vögtle, Ed., vol. 212 of Topics in Current Chemistry, pp. 81–135, Springer, Berlin, Heidelberg, 2001.

[55] X. Huang, H. Zhang, L. Liang, and B. Tan, "Preparation of nanoparticles with multi-functional water-soluble polymer ligands," *Progress in Chemistry*, vol. 22, no. 5, pp. 953–961, 2010.

[56] N. Erathodiyil and J. Y. Ying, "Functionalization of inorganic nanoparticles for bioimaging applications," *Accounts of Chemical Research*, vol. 44, no. 10, pp. 925–935, 2011.

[57] A. Lopez and J. Liu, "DNA-templated fluorescent gold nanoclusters reduced by good's buffer: from blue-emitting seeds to red and near infrared emitters," *Canadian Journal of Chemistry*, vol. 93, no. 6, pp. 615–620, 2015.

[58] W. Y. Mu, R. Yang, A. Robertson, and Q. Y. Chen, "A near-infrared BSA coated DNA-AgNCs for cellular imaging," *Colloids and Surfaces B: Biointerfaces*, vol. 162, pp. 427–431, 2018.

[59] A. Aires, I. Llarena, M. Moller, J. Castro-Smirnov, J. Cabanillas-Gonzalez, and A. L. Cortajarena, "A simple approach to design proteins for the sustainable synthesis of metal nanoclusters," *Angewandte Chemie International Edition*, vol. 58, no. 19, pp. 6214–6219, 2019.

[60] S. M. Ghoreishian, S. M. Kang, G. Seeta Rama Raju et al., "γ-Radiolysis as a highly efficient green approach to the synthesis of metal nanoclusters: a review of mechanisms and applications," *Chemical Engineering Journal*, vol. 360, pp. 1390–1406, 2019.

[61] B. A. Roberts and C. R. Strauss, "Toward rapid, "green", predictable microwave-assisted synthesis," *Accounts of Chemical Research*, vol. 38, no. 8, pp. 653–661, 2005.

[62] H. Xu, B. W. Zeiger, and K. S. Suslick, "Sonochemical synthesis of nanomaterials," *Chemical Society Reviews*, vol. 42, no. 7, pp. 2555–2567, 2013.

[63] K. Watanabe, D. Menzel, N. Nilius, and H.-J. Freund, "Photochemistry on metal nanoparticles," *Chemical Reviews*, vol. 106, no. 10, pp. 4301–4320, 2006.

[64] R. A. Hackendorn and A. V. Virkar, "Synthesis of platinum nanoclusters and electrochemical investigation of their stability," *Journal of Power Sources*, vol. 240, pp. 618–629, 2013.

[65] X. Yuan, Z. Luo, Q. Zhang et al., "Synthesis of highly fluorescent metal (Ag, Au, Pt, and Cu) nanoclusters by electrostatically induced reversible phase transfer," *ACS Nano*, vol. 5, no. 11, pp. 8800–8808, 2011.

[66] I. Chakraborty, R. G. Bhuin, S. Bhat, and T. Pradeep, "Blue emitting undecaplatinum clusters," *Nanoscale*, vol. 6, no. 15, pp. 8561–8564, 2014.

[67] L. Wang, S. Ouyang, B. Liu, R. Yang, T. Wang, and S. Wang, "One-pot synthesis of octahedral platinum nanoclusters with enhanced electrocatalytic activities," *Materials Research Bulletin*, vol. 61, pp. 357–362, 2015.

[68] R. W. J. Scott, O. M. Wilson, and R. M. Crooks, "Synthesis, characterization, and applications of dendrimer-encapsulated nanoparticles," *The Journal of Physical Chemistry B*, vol. 109, no. 2, pp. 692–704, 2005.

[69] Y. Borodko, C. M. Thompson, W. Huang, H. B. Yildiz, H. Frei, and G. A. Somorjai, "Spectroscopic study of platinum and rhodium dendrimer (PAMAM G4OH) compounds: structure and stability," *The Journal of Physical Chemistry C*, vol. 115, no. 11, pp. 4757–4767, 2011.

[70] P. Maity, S. Yamazoe, and T. Tsukuda, "Dendrimer-encapsulated copper cluster as a chemoselective and regenerable hydrogenation catalyst," *ACS Catalysis*, vol. 3, no. 2, pp. 182–185, 2013.

[71] H. Lim, Y. Ju, and J. Kim, "Tailoring catalytic activity of Pt nanoparticles encapsulated inside dendrimers by tuning nanoparticle sizes with subnanometer accuracy for sensitive chemiluminescence-based analyses," *Analytical Chemistry*, vol. 88, no. 9, pp. 4751–4758, 2016.

[72] Y. Borodko, P. Ercius, V. Pushkarev, C. Thompson, and G. Somorjai, "From single Pt atoms to Pt nanocrystals: photoreduction of Pt^{2+} inside of a PAMAM dendrimer," *The Journal of Physical Chemistry Letters*, vol. 3, no. 2, pp. 236–241, 2012.

[73] W. Tu and H. Liu, "Continuous synthesis of colloidal metal nanoclusters by microwave irradiation," *Chemistry of Materials*, vol. 12, no. 2, pp. 564–567, 2000.

[74] H. Zhang, X. Huang, L. Li et al., "Photoreductive synthesis of water-soluble fluorescent metal nanoclusters," *Chemical Communications*, vol. 48, no. 4, pp. 567–569, 2012.

[75] J. Quinson, L. Kacenauskaite, T. L. Christiansen, T. Vosch, M. Arenz, and K. M. Ø. Jensen, "Spatially localized synthesis and structural characterization of platinum nanocrystals obtained using UV light," *ACS Omega*, vol. 3, no. 8, pp. 10351–10356, 2018.

[76] P. Wang, F. Li, X. Huang, Y. Li, and L. Wang, "In situ electrodeposition of Pt nanoclusters on glassy carbon surface modified by monolayer choline film and their electrochemical applications," *Electrochemistry Communications*, vol. 10, no. 2, pp. 195–199, 2008.

[77] F. Liu, Y. Deng, X. Han, W. Hu, and C. Zhong, "Electrodeposition of metals and alloys from ionic liquids," *Journal of Alloys and Compounds*, vol. 654, pp. 163–170, 2016.

[78] L. Qian, Y. Liu, Y. Song, Z. Li, and X. Yang, "Electrodeposition of Pt nanoclusters on the surface modified by monolayer poly(amidoamine) dendrimer film," *Electrochemistry Communications*, vol. 7, no. 12, pp. 1209–1212, 2005.

[79] J. Camacho-Bunquin, M. S. Ferrandon, H. Sohn et al., "Atomically precise strategy to a PtZn alloy nanocluster catalyst for the deep dehydrogenation of *n*-butane to 1,3-butadiene," *ACS Catalysis*, vol. 8, no. 11, pp. 10058–10063, 2018.

[80] H. Shi, P. S. Thapa, B. Subramaniam, and R. V. Chaudhari, "Oxidation of glucose using mono- and bimetallic catalysts

under base-free conditions," *Organic Process Research & Development*, vol. 22, no. 12, pp. 1653–1662, 2018.

[81] J. Zhang, W. L. Yu, S. H. Zhou, Y. Li, Y.-F. Zhang, and W.-K. Chen, "Nanoclusters $Au_{19}Pd$ and $Au_{19}Pt$ catalyzing CO oxidation: a density functional study," *Chinese Journal of Structural Chemistry*, vol. 37, no. 12, pp. 1849–1859, 2018.

[82] K. Li, Y. Li, Y. Wang, J. Ge, C. Liu, and W. Xing, "Enhanced electrocatalytic performance for the hydrogen evolution reaction through surface enrichment of platinum nanoclusters alloying with ruthenium *in situ* embedded in carbon," *Energy & Environmental Science*, vol. 11, no. 5, pp. 1232–1239, 2018.

[83] X. L. Chen, L. Zhang, J. J. Feng et al., "Facile solvothermal fabrication of polypyrrole sheets supported dendritic platinum-cobalt nanoclusters for highly efficient oxygen reduction and ethylene glycol oxidation," *Journal of Colloid and Interface Science*, vol. 530, pp. 394–402, 2018.

[84] V. Sharma, S. Kumar, and V. Krishnan, "Homogeneously embedded Pt nanoclusters on amorphous titania matrix as highly efficient visible light active photocatalyst material," *Materials Chemistry and Physics*, vol. 179, pp. 129–136, 2016.

[85] A. S. Maldonado, C. I. N. Morgade, S. B. Ramos, and G. F. Cabeza, "Comparative study of CO adsorption on planar and tetrahedral Pt nanoclusters supported on TiO_2(110) stoichiometric and reduced surfaces," *Molecular Catalysis*, vol. 433, pp. 403–413, 2017.

[86] M. Torabi, R. Karimi Shervedani, and A. Amini, "High performance porous graphene nanoribbons electrodes synthesized via hydrogen plasma and modified by Pt-Ru nanoclusters for charge storage and methanol oxidation," *Electrochimica Acta*, vol. 290, pp. 616–625, 2018.

[87] L. Sun, B. Wang, and Y. Wang, "A Schottky-junction-based platinum nanoclusters@silicon carbide nanosheet as long-term stable hydrogen sensors," *Applied Surface Science*, vol. 473, pp. 641–648, 2019.

[88] L. Lu, "Highly sensitive detection of nitrite at a novel electrochemical sensor based on mutually stabilized Pt nanoclusters doped CoO nanohybrid," *Sensors and Actuators B: Chemical*, vol. 281, pp. 182–190, 2019.

[89] X. Zuo, H. Liu, D. Guo, and X. Yang, "Enantioselective hydrogenation of pyruvates over polymer-stabilized and supported platinum nanoclusters," *Tetrahedron*, vol. 55, no. 25, pp. 7787–7804, 1999.

[90] K. A. Carrado, G. Sandi, R. Kizilel, S. Seifert, and N. Castagnola, "Platinum nanoclusters immobilized on polymer–clay nanocomposite films," *Applied Clay Science*, vol. 30, no. 2, pp. 94–102, 2005.

[91] Z. Marco, C. Paolo, and C. Benedetto, "Chapter 10 - metal nanoclusters supported on cross-linked functional polymers: a class of emerging metal catalysts," in *Metal Nanoclusters in Catalysis and Materials Science: the issue of size control*, pp. 201–232, Elsevier, 2008.

[92] L. Jia, D. A. Bulushev, O. Y. Podyacheva et al., "Pt nanoclusters stabilized by N-doped carbon nanofibers for hydrogen production from formic acid," *Journal of Catalysis*, vol. 307, pp. 94–102, 2013.

[93] M. F. Luo, W. H. Wen, C. S. Lin, C. I. Chiang, S. D. Sartale, and M. S. Zei, "Structures of Co and Pt nanoclusters on a thin film of Al_2O_3/NiAl(100) from reflection high-energy electron diffraction and scanning-tunnelling microscopy," *Surface Science*, vol. 601, no. 10, pp. 2139–2146, 2007.

[94] M. F. Luo, W. R. Lin, W. H. Wen, and B. W. Chang, "Methanol electro-oxidation and induced sintering on Pt nanoclusters supported on thin-film Al_2O_3/NiAl(100)," *Surface Science*, vol. 602, no. 21, pp. 3258–3265, 2008.

[95] C. S. Chao, T. W. Liao, C. X. Wang, Y. D. Li, T. C. Hung, and M. F. Luo, "Obstruction by CO of the decomposition of methanol on Pt nanoclusters on a thin film of Al_2O_3/NiAl(100)," *Applied Surface Science*, vol. 293, pp. 352–358, 2014.

[96] A. S. Bazhenov and K. Honkala, "Globally optimized equilibrium shapes of zirconia-supported Rh and Pt nanoclusters: insights into site assembly and reactivity," *The Journal of Physical Chemistry C*, vol. 123, no. 12, pp. 7209–7216, 2019.

[97] M. Mon, M. A. Rivero-Crespo, J. Ferrando-Soria et al., "Synthesis of densely packaged, ultrasmall $Pt^0{}_2$ clusters within a thioether-functionalized MOF: catalytic activity in industrial reactions at low temperature," *Angewandte Chemie International Edition*, vol. 57, no. 21, pp. 6186–6191, 2018.

[98] C. Feng and P. He, "Atomistic investigation on the diffusion mechanism of Pt nanoclusters on well-aligned multi-walled carbon nanotubes," *Computational Materials Science*, vol. 103, pp. 157–164, 2015.

[99] H. Huang, Z. He, X. Lin, W. Ruan, Y. Liu, and Z. Yang, "Ultradispersed platinum nanoclusters on polydopamine-functionalized carbon nanotubes as an excellent catalyst for methanol oxidation reaction," *Applied Catalysis A: General*, vol. 490, pp. 65–70, 2015.

[100] I. Fampiou and A. Ramasubramaniam, "Influence of support effects on CO oxidation kinetics on CO-saturated graphene-supported Pt_{13} nanoclusters," *The Journal of Physical Chemistry C*, vol. 119, no. 16, pp. 8703–8710, 2015.

[101] P. Y. Cai, Y. W. Huang, Y. C. Huang et al., "Atomic structures of Pt nanoclusters supported on graphene grown on Pt(111)," *The Journal of Physical Chemistry C*, vol. 122, no. 28, pp. 16132–16141, 2018.

[102] F. Düll, F. Späth, U. Bauer et al., "Reactivity of CO on sulfur-passivated graphene-supported platinum nanocluster arrays," *The Journal of Physical Chemistry C*, vol. 122, no. 28, pp. 16008–16015, 2018.

[103] X. Liu, Y. Tang, M. Shen et al., "Bifunctional CO oxidation over Mn-mullite anchored Pt sub-nanoclusters *via* atomic layer deposition," *Chemical Science*, vol. 9, no. 9, pp. 2469–2473, 2018.

[104] D. Lee, Y. Kim, Y. Kwon et al., "Boosting the electrocatalytic glycerol oxidation performance with highly-dispersed Pt nanoclusters loaded on 3D graphene-like microporous carbon," *Applied Catalysis B: Environmental*, vol. 245, pp. 555–568, 2019.

[105] Z. Wang, G. Zhang, Z. Zhong, Y. Lin, and Z. Su, "In-situ synthesis of platinum nanoclusters in polyelectrolyte multilayer films," *Thin Solid Films*, vol. 660, pp. 59–64, 2018.

[106] M. Hyotanishi, Y. Isomura, H. Yamamoto, H. Kawasaki, and Y. Obora, "Surfactant-free synthesis of palladium nanoclusters for their use in catalytic cross-coupling reactions," *Chemical Communications*, vol. 47, no. 20, pp. 5750–5752, 2011.

[107] H. Kawasaki, H. Yamamoto, H. Fujimori, R. Arakawa, M. Inada, and Y. Iwasaki, "Surfactant-free solution synthesis of fluorescent platinum subnanoclusters," *Chemical Communications*, vol. 46, no. 21, pp. 3759–3761, 2010.

[108] P. N. Duchesne and P. Zhang, "Local structure of fluorescent platinum nanoclusters," *Nanoscale*, vol. 4, no. 14, pp. 4199–4205, 2012.

[109] A. George, H. Gopalakrishnan, and S. Mandal, "Surfactant free platinum nanocluster as fluorescent probe for the selective detection of Fe (III) ions in aqueous medium," *Sensors and Actuators B: Chemical*, vol. 243, pp. 332–337, 2017.

[110] P. Yu, X. Wen, Y.-R. Toh, X. Ma, and J. Tang, "Fluorescent metallic nanoclusters: electron dynamics, structure, and applications," *Particle & Particle Systems Characterization*, vol. 32, no. 2, pp. 142–163, 2015.

[111] H. Jiang and X.-M. Wang, "Progress of metal nanoclusters-based electrochemiluminescent analysis," *Chinese Journal of Analytical Chemistry*, vol. 45, no. 12, pp. 1776–1785, 2017.

[112] D. Li, Z. Chen, and X. Mei, "Fluorescence enhancement for noble metal nanoclusters," *Advances in Colloid and Interface Science*, vol. 250, pp. 25–39, 2017.

[113] S. H. Kim, K. C. Kim, Y. S. Kim, and H. J. Kim, "Abnormal optical changes with the formation of Pt nanoclusters," *Current Applied Physics*, vol. 6, no. 6, pp. 1036–1039, 2006.

[114] J. Zheng, P. R. Nicovich, and R. M. Dickson, "Highly fluorescent noble-metal quantum dots," *Annual Review of Physical Chemistry*, vol. 58, no. 1, pp. 409–431, 2007.

[115] A. Heuer-Jungemann, N. Feliu, I. Bakaimi et al., "The role of ligands in the chemical synthesis and applications of inorganic nanoparticles," *Chemical Reviews*, vol. 119, no. 8, pp. 4819–4880, 2019.

[116] Z. Wu and R. Jin, "On the ligand's role in the fluorescence of gold nanoclusters," *Nano Letters*, vol. 10, no. 7, pp. 2568–2573, 2010.

[117] J. M. Forward, D. Bohmann, J. P. Fackler, and R. J. Staples, "Luminescence studies of gold(I) thiolate complexes," *Inorganic Chemistry*, vol. 34, no. 25, pp. 6330–6336, 1995.

[118] M. S. Devadas, J. Kim, E. Sinn, D. Lee, T. Goodson III, and G. Ramakrishna, "Unique ultrafast visible luminescence in monolayer-protected Au_{25} clusters," *Journal of Physical Chemistry C*, vol. 114, no. 51, pp. 22417–22423, 2010.

[119] X. Huang, B. Li, L. Li et al., "Facile preparation of highly blue fluorescent metal nanoclusters in organic media," *The Journal of Physical Chemistry C*, vol. 116, no. 1, pp. 448–455, 2012.

[120] X. Yuan, M. I. Setyawati, A. S. Tan, C. N. Ong, D. T. Leong, and J. Xie, "Highly luminescent silver nanoclusters with tunable emissions: cyclic reduction-decomposition synthesis and antimicrobial properties," *NPG Asia Materials*, vol. 5, no. 2, article e39, 2013.

[121] E. Gwinn, D. Schultz, S. Copp, and S. Swasey, "DNA-protected silver clusters for nanophotonics," *Nanomaterials*, vol. 5, no. 1, pp. 180–207, 2015.

[122] Y. S. Ang, W. W. E. Woon, and L. Y. L. Yung, "The role of spacer sequence in modulating turn-on fluorescence of DNA-templated silver nanoclusters," *Nucleic Acids Research*, vol. 46, no. 14, pp. 6974–6982, 2018.

[123] M. Liu, F. Tang, Z. Yang, J. Xu, and X. Yang, "Recent progress on gold-nanocluster-based fluorescent probe for environmental analysis and biological sensing," *Journal of Analytical Methods in Chemistry*, vol. 2019, Article ID 1095148, 10 pages, 2019.

[124] S. Shadpour, J. P. Vanegas, A. Nemati, and T. Hegmann, "Amplification of chirality by adenosine monophosphate-capped luminescent gold nanoclusters in nematic lyotropic chromonic liquid crystal tactoids," *ACS Omega*, vol. 4, no. 1, pp. 1662–1668, 2019.

[125] L. Yang, X. Lou, F. Yu, and H. Liu, "Cross-linking structure-induced strong blue emissive gold nanoclusters for intracellular sensing," *Analyst*, vol. 144, no. 8, pp. 2765–2772, 2019.

[126] J. V. Frangioni, "*In vivo* near-infrared fluorescence imaging," *Current Opinion in Chemical Biology*, vol. 7, no. 5, pp. 626–634, 2003.

[127] B. Rosenberg, L. Vancamp, J. E. Trosko, and V. H. Mansour, "Platinum compounds: a new class of potent antitumour agents," *Nature*, vol. 222, no. 5191, pp. 385-386, 1969.

[128] X. Xia, Y. Zhang, and J. Wang, "Novel fabrication of highly fluorescent Pt nanoclusters and their applications in hypochlorite assay," *RSC Advances*, vol. 4, no. 48, pp. 25365–25368, 2014.

[129] X. Le Guével, V. Trouillet, C. Spies, G. Jung, and M. Schneider, "Synthesis of yellow-emitting platinum nanoclusters by ligand etching," *The Journal of Physical Chemistry C*, vol. 116, no. 10, pp. 6047–6051, 2012.

[130] S.-I. Tanaka, J. Miyazaki, D. K. Tiwari, T. Jin, and Y. Inouye, "Fluorescent platinum nanoclusters: synthesis, purification, characterization, and application to bioimaging," *Angewandte Chemie International Edition*, vol. 50, no. 2, pp. 431–435, 2011.

[131] S.-I. Tanaka, K. Aoki, A. Muratsugu, H. Ishitobi, T. Jin, and Y. Inouye, "Synthesis of green-emitting Pt_8 nanoclusters for biomedical imaging by pre-equilibrated Pt/PAMAM (G4-OH) and mild reduction," *Optical Materials Express*, vol. 3, no. 2, pp. 157–165, 2013.

[132] X. Huang, K. Aoki, H. Ishitobi, and Y. Inouye, "Preparation of Pt nanoclusters with different emission wavelengths and their application in Co^{2+} detection," *ChemPhysChem*, vol. 15, no. 4, pp. 642–646, 2014.

[133] N. Xu, H.-W. Li, and Y. Wu, "Hydrothermal synthesis of polyethylenimine-protected high luminescent Pt-nanoclusters and their application to the detection of nitroimidazoles," *Analytica Chimica Acta*, vol. 958, pp. 51–58, 2017.

[134] J. García Fernández, L. Trapiella-Alfonso, J. M. Costa-Fernández, R. Pereiro, and A. Sanz-Medel, "Aqueous synthesis of near-infrared highly fluorescent platinum nanoclusters," *Nanotechnology*, vol. 26, no. 21, article 215601, 2015.

[135] F. Molaabasi, M. Sarparast, M. Shamsipur et al., "Shape-controlled synthesis of luminescent hemoglobin capped hollow porous platinum nanoclusters and their application to catalytic oxygen reduction and cancer imaging," *Scientific Reports*, vol. 8, no. 1, article 14507, 2018.

[136] F. Klasovsky and P. Claus, "Chapter 8 - metal nanoclusters in catalysis: effects of nanoparticle size, shape, and structure," in *Metal Nanoclusters in Catalysis and Materials Science: the issue of size control*, pp. 167–181, Elsevier, 2008.

[137] J. Ustarroz, I. M. Ornelas, G. Zhang et al., "Mobility and poisoning of mass-selected platinum nanoclusters during the oxygen reduction reaction," *ACS Catalysis*, vol. 8, no. 8, pp. 6775–6790, 2018.

[138] J. Huang and M. Eikerling, "Modeling the oxygen reduction reaction at platinum-based catalysts: a brief review of recent developments," *Current Opinion in Electrochemistry*, vol. 13, pp. 157–165, 2019.

[139] F. T. Wagner, B. Lakshmanan, and M. F. Mathias, "Electrochemistry and the future of the automobile," *The Journal of Physical Chemistry Letters*, vol. 1, no. 14, pp. 2204–2219, 2010.

[140] X. Zhou, Y. Gan, J. du et al., "A review of hollow Pt-based nanocatalysts applied in proton exchange membrane fuel cells," *Journal of Power Sources*, vol. 232, pp. 310–322, 2013.

[141] F. Zhang, F. Jiao, X. Pan et al., "Tailoring the oxidation activity of Pt nanoclusters via encapsulation," *ACS Catalysis*, vol. 5, no. 2, pp. 1381–1385, 2015.

[142] G. Ercolano, S. Cavaliere, J. Rozière, and D. J. Jones, "Recent developments in electrocatalyst design thrifting noble metals in fuel cells," *Current Opinion in Electrochemistry*, vol. 9, pp. 271–277, 2018.

[143] J. Zhang, X. Yan, and H. Liu, "The effects of tin on the hydrogenation of α-diketones over platinum nanoclusters," *Journal of Molecular Catalysis A: Chemical*, vol. 176, no. 1-2, pp. 281–286, 2001.

[144] A. S. Crampton, "Hydrogenation reactions on small platinum clusters," in *Encyclopedia of Interfacial Chemistry*, pp. 465–476, Elsevier, 2018.

[145] C. Adlhart and E. Uggerud, "Reactions of platinum clusters $Pt_n^{\pm}$, n=1–21, with CH_4: to react or not to react," *Chemical Communications*, no. 24, pp. 2581-2582, 2006.

[146] K. Kon, S. M. A. Hakim Siddiki, and K.-I. Shimizu, "Size- and support-dependent Pt nanocluster catalysis for oxidant-free dehydrogenation of alcohols," *Journal of Catalysis*, vol. 304, pp. 63–71, 2013.

[147] R. M. Rioux, H. Song, P. Yang, and G. A. Somorjai, "Chapter 7 - platinum nanoclusters' size and surface structure sensitivity of catalytic reactions," in *Metal nanoclusters in catalysis and materials science: the issue of size control*, pp. 149–166, Elsevier, 2008.

[148] M. Shao, A. Peles, and K. Shoemaker, "Electrocatalysis on platinum nanoparticles: particle size effect on oxygen reduction reaction activity," *Nano Letters*, vol. 11, no. 9, pp. 3714–3719, 2011.

[149] H. Yano, J. Inukai, H. Uchida et al., "Particle-size effect of nanoscale platinum catalysts in oxygen reduction reaction: an electrochemical and ^{195}Pt EC-NMR study," *Physical Chemistry Chemical Physics*, vol. 8, no. 42, pp. 4932–4939, 2006.

[150] T. Imaoka, H. Kitazawa, W.-J. Chun, and K. Yamamoto, "Finding the most catalytically active platinum clusters with low atomicity," *Angewandte Chemie International Edition*, vol. 54, no. 34, pp. 9810–9815, 2015.

[151] S. Vajda, M. J. Pellin, J. P. Greeley et al., "Subnanometre platinum clusters as highly active and selective catalysts for the oxidative dehydrogenation of propane," *Nature Materials*, vol. 8, no. 3, pp. 213–216, 2009.

[152] Y. Shiraishi, M. Nakayama, E. Takagi, T. Tominaga, and N. Toshima, "Effect of quantity of polymer on catalysis and superstructure size of polymer-protected Pt nanoclusters," *Inorganica Chimica Acta*, vol. 300-302, pp. 964–969, 2000.

[153] J.-L. Lan, C.-C. Wan, T.-C. Wei, W.-C. Hsu, and Y.-H. Chang, "Durability test of PVP-capped Pt nanoclusters counter electrode for highly efficiency dye-sensitized solar cell," *Progress in Photovoltaics: Research and Applications*, vol. 20, no. 1, pp. 44–50, 2012.

[154] H. Li, L. Li, and Y. Li, "The electronic structure and geometric structure of nanoclusters as catalytic active sites," *Nanotechnology Reviews*, vol. 2, no. 5, pp. 515–528, 2013.

[155] T. Imaoka, H. Kitazawa, W. J. Chun, S. Omura, K. Albrecht, and K. Yamamoto, "Magic number Pt_{13} and misshapen Pt_{12} clusters: which one is the better catalyst?," *Journal of the American Chemical Society*, vol. 135, no. 35, pp. 13089–13095, 2013.

[156] V. S. Baidyshev, Y. Y. Gafner, S. L. Gafner, and L. V. Redel, "Thermal stability of Pt nanoclusters interacting to carbon sublattice," *Physics of the Solid State*, vol. 59, no. 12, pp. 2512–2518, 2017.

[157] S. H. Lee, S. S. Han, J. K. Kang, J. H. Ryu, and H. M. Lee, "Phase stability of Pt nanoclusters and the effect of a (0001) graphite surface through molecular dynamics simulation," *Surface Science*, vol. 602, no. 7, pp. 1433–1439, 2008.

[158] H. Akbarzadeh and G. A. Parsafar, "A molecular-dynamics study of thermal and physical properties of platinum nanoclusters," *Fluid Phase Equilibria*, vol. 280, no. 1-2, pp. 16–21, 2009.

[159] M. Farrag, "Preparation, characterization and photocatalytic activity of size selected platinum nanoclusters," *Journal of Photochemistry and Photobiology A: Chemistry*, vol. 318, pp. 42–50, 2016.

[160] D. Pedone, M. Moglianetti, E. De Luca, G. Bardi, and P. P. Pompa, "Platinum nanoparticles in nanobiomedicine," *Chemical Society Reviews*, vol. 46, no. 16, pp. 4951–4975, 2017.

[161] J. Niu, X. Wang, J. Lv, Y. Li, and B. Tang, "Luminescent nanoprobes for *in-vivo* bioimaging," *TrAC Trends in Analytical Chemistry*, vol. 58, pp. 112–119, 2014.

[162] F. Su, Q. Jia, Z. Li et al., "Aptamer-templated silver nanoclusters embedded in zirconium metal-organic framework for targeted antitumor drug delivery," *Microporous and Mesoporous Materials*, vol. 275, pp. 152–162, 2019.

[163] S. Jin and K. Ye, "Nanoparticle-mediated drug delivery and gene therapy," *Biotechnology Progress*, vol. 23, no. 1, pp. 32–41, 2007.

[164] A. K. Salem, P. C. Searson, and K. W. Leong, "Multifunctional nanorods for gene delivery," *Nature Materials*, vol. 2, no. 10, pp. 668–671, 2003.

[165] J. Xu and L. Shang, "Emerging applications of near-infrared fluorescent metal nanoclusters for biological imaging," *Chinese Chemical Letters*, vol. 29, no. 10, pp. 1436–1444, 2018.

[166] Z. Popović, W. Liu, V. P. Chauhan et al., "A nanoparticle size series for in vivo fluorescence imaging," *Angewandte Chemie International Edition*, vol. 49, no. 46, pp. 8649–8652, 2010.

[167] V. Parthasarathy, S. Fery-Forgues, E. Campioli, G. Recher, F. Terenziani, and M. Blanchard-Desce, "Dipolar versus octupolar triphenylamine-based fluorescent organic nanoparticles as brilliant one- and two-photon emitters for (bio)imaging," *Small*, vol. 7, no. 22, pp. 3219–3229, 2011.

[168] A. Shao, X. Wu, and W. Zhu, "Chapter 5. Bioimaging nanomaterials based on near infrared organic dyes," in *Near-Infrared Nanomaterials: Preparation, Bioimaging and Therapy Applications*, pp. 125–157, Royal Society of Chemistry, 2016.

[169] M. J. Schnermann, "Organic dyes for deep bioimaging," *Nature*, vol. 551, no. 7679, pp. 176-177, 2017.

[170] M. Bruchez Jr., M. Moronne, P. Gin, S. Weiss, and A. P. Alivisatos, "Semiconductor nanocrystals as fluorescent biological labels," *Science*, vol. 281, no. 5385, pp. 2013–2016, 1998.

[171] R. Freeman and I. Willner, "Optical molecular sensing with semiconductor quantum dots (QDs)," *Chemical Society Reviews*, vol. 41, no. 10, pp. 4067–4085, 2012.

[172] X. Shu, A. Royant, M. Z. Lin et al., "Mammalian expression of infrared fluorescent proteins engineered from a bacterial phytochrome," *Science*, vol. 324, no. 5928, pp. 804–807, 2009.

[173] F. V. Subach and V. V. Verkhusha, "Chromophore transformations in red fluorescent proteins," *Chemical Reviews*, vol. 112, no. 7, pp. 4308–4327, 2012.

[174] J.-C. G. Bünzli, "Lanthanide luminescence for biomedical analyses and imaging," *Chemical Reviews*, vol. 110, no. 5, pp. 2729–2755, 2010.

[175] S. V. Eliseeva and J.-C. G. Bunzli, "Lanthanide luminescence for functional materials and bio-sciences," *Chemical Society Reviews*, vol. 39, no. 1, pp. 189–227, 2010.

[176] X. Zhang, S. Wang, C. Zhu et al., "Carbon-dots derived from nanodiamond: photoluminescence tunable nanoparticles for cell imaging," *Journal of Colloid and Interface Science*, vol. 397, pp. 39–44, 2013.

[177] P. Das, M. Bose, S. Ganguly et al., "Green approach to photoluminescent carbon dots for imaging of gram-negative bacteria *Escherichia coli*," *Nanotechnology*, vol. 28, no. 19, article 195501, 2017.

[178] U. Resch-Genger, M. Grabolle, S. Cavaliere-Jaricot, R. Nitschke, and T. Nann, "Quantum dots versus organic dyes as fluorescent labels," *Nature Methods*, vol. 5, no. 9, pp. 763–775, 2008.

[179] W. W. Yu, E. Chang, R. Drezek, and V. L. Colvin, "Water-soluble quantum dots for biomedical applications," *Biochemical and Biophysical Research Communications*, vol. 348, no. 3, pp. 781–786, 2006.

[180] S. F. Lee and M. A. Osborne, "Brightening, blinking, bluing and bleaching in the life of a quantum dot: friend or foe?," *ChemPhysChem*, vol. 10, no. 13, pp. 2174–2191, 2009.

[181] M. M. Barroso, "Quantum dots in cell biology," *Journal of Histochemistry & Cytochemistry*, vol. 59, no. 3, pp. 237–251, 2011.

[182] X. Le Guével, "Recent advances on the synthesis of metal quantum nanoclusters and their application for bioimaging," *IEEE Journal of Selected Topics in Quantum Electronics*, vol. 20, no. 3, pp. 45–56, 2014.

[183] L. Ma, V. Andoh, H. Liu, J. Song, G. Wu, and L. Li, "Biological effects of gold nanoclusters are evaluated by using silkworm as a model animal," *Journal of Materials Science*, vol. 54, no. 6, pp. 4997–5007, 2019.

[184] G. Zuber, E. Weiss, and M. Chiper, "Biocompatible gold nanoclusters: synthetic strategies and biomedical prospects," *Nanotechnology*, vol. 30, no. 35, article 352001, 2019.

[185] K. Zheng, X. Yuan, N. Goswami, Q. Zhang, and J. Xie, "Recent advances in the synthesis, characterization, and biomedical applications of ultrasmall thiolated silver nanoclusters," *RSC Advances*, vol. 4, no. 105, pp. 60581–60596, 2014.

[186] X. Chen, J. Zhou, X. Yue et al., "Selective bio-labeling and induced apoptosis of hematopoietic cancer cells using dual-functional polyethylenimine-caged platinum nanoclusters," *Biochemical and Biophysical Research Communications*, vol. 503, no. 3, pp. 1465–1470, 2018.

[187] Y. Xin, X. Huang, Z. Li et al., "Versatile Pt NCs-based chemotherapeutic agents significantly induce the apoptosis of cisplatin-resistant non-small cell lung cancer," *Biochemical and Biophysical Research Communications*, vol. 512, no. 2, pp. 218–223, 2019.

[188] X. Huang, H. Ishitobi, and Y. Inouye, "Formation of fluorescent platinum nanoclusters using hyper-branched polyethylenimine and their conjugation to antibodies for bioimaging," *RSC Advances*, vol. 6, no. 12, pp. 9709–9716, 2016.

[189] T. Boulikas and M. Vougiouka, "Cisplatin and platinum drugs at the molecular level (review)," *Oncology Reports*, vol. 10, no. 6, pp. 1663–1682, 2003.

[190] K. Barabas, R. Milner, D. Lurie, and C. Adin, "Cisplatin: a review of toxicities and therapeutic applications," *Veterinary and Comparative Oncology*, vol. 6, no. 1, pp. 1–18, 2008.

[191] K. N. Sugahara, T. Teesalu, P. P. Karmali et al., "Tissue-penetrating delivery of compounds and nanoparticles into tumors," *Cancer Cell*, vol. 16, no. 6, pp. 510–520, 2009.

[192] X. Wang, X. Wang, and Z. Guo, "Functionalization of platinum complexes for biomedical applications," *Accounts of Chemical Research*, vol. 48, no. 9, pp. 2622–2631, 2015.

[193] M. A. Fuertes, C. Alonso, and J. M. Pérez, "Biochemical modulation of cisplatin mechanisms of action: enhancement of antitumor activity and circumvention of drug resistance," *Chemical Reviews*, vol. 103, no. 3, pp. 645–662, 2003.

[194] N. C. Schmitt and E. W. Rubel, "Osteopontin does not mitigate cisplatin ototoxicity or nephrotoxicity in adult mice," *Otolaryngology-Head and Neck Surgery*, vol. 149, no. 4, pp. 614–620, 2013.

[195] G. Mandriota, R. Di Corato, M. Benedetti, F. De Castro, F. P. Fanizzi, and R. Rinaldi, "Design and application of cisplatin-loaded magnetic nanoparticle clusters for smart chemotherapy," *ACS Applied Materials & Interfaces*, vol. 11, no. 2, pp. 1864–1875, 2019.

[196] H. M. Kieler-Ferguson, J. M. J. Fréchet, and F. C. Szoka Jr., "Clinical developments of chemotherapeutic nanomedicines: polymers and liposomes for delivery of camptothecins and platinum(II) drugs," *WIREs Nanomedicine and Nanobiotechnology*, vol. 5, no. 2, pp. 130–138, 2013.

[197] H. S. Oberoi, N. V. Nukolova, A. V. Kabanov, and T. K. Bronich, "Nanocarriers for delivery of platinum anticancer drugs," *Advanced Drug Delivery Reviews*, vol. 65, no. 13-14, pp. 1667–1685, 2013.

[198] L. Gatti, G. Cassinelli, N. Zaffaroni, C. Lanzi, and P. Perego, "New mechanisms for old drugs: insights into DNA-unrelated effects of platinum compounds and drug resistance determinants," *Drug Resistance Updates*, vol. 20, pp. 1–11, 2015.

[199] I. J. Majoros, B. B. Ward, K. H. Lee et al., "Chapter 8 - progress in cancer nanotechnology," in *Progress in Molecular Biology and Translational Science*, vol. 95, pp. 193–236, Academic Press, 2010.

[200] S. Dilruba and G. V. Kalayda, "Platinum-based drugs: past, present and future," *Cancer Chemotherapy and Pharmacology*, vol. 77, no. 6, pp. 1103–1124, 2016.

[201] C.-T. Chien, J. Y. Yan, W. C. Chiu, T. H. Wu, C. Y. Liu, and S. Y. Lin, "Caged Pt nanoclusters exhibiting corrodibility to exert tumor-inside activation for anticancer chemotherapeutics," *Advanced Materials*, vol. 25, no. 36, pp. 5067–5073, 2013.

[202] D. Chen, S. Gao, W. Ge, Q. Li, H. Jiang, and X. Wang, "One-step rapid synthesis of fluorescent platinum nanoclusters for cellular imaging and photothermal treatment," *RSC Advances*, vol. 4, no. 76, pp. 40141–40145, 2014.

[203] H. Xia, F. Li, X. Hu et al., "pH-sensitive Pt nanocluster assembly overcomes cisplatin resistance and heterogeneous stemness of hepatocellular carcinoma," *ACS Central Science*, vol. 2, no. 11, pp. 802–811, 2016.

[204] X. Hu, F. Li, N. Noor, and D. Ling, "Platinum drugs: from Pt(II) compounds, Pt(IV) prodrugs, to Pt nanocrystals/nanoclusters," *Science Bulletin*, vol. 62, no. 8, pp. 589–596, 2017.

[205] X. Yuan, M. I. Setyawati, D. T. Leong, and J. Xie, "Ultrasmall Ag^+-rich nanoclusters as highly efficient nanoreservoirs for bacterial killing," *Nano Research*, vol. 7, no. 3, pp. 301–307, 2014.

[206] S. B. Subramaniyan, A. Ramani, V. Ganapathy, and V. Anbazhagan, "Preparation of self-assembled platinum nanoclusters to combat *Salmonella typhi* infection and inhibit biofilm formation," *Colloids and Surfaces B: Biointerfaces*, vol. 171, pp. 75–84, 2018.

Hindawi
Journal of Nanomaterials
Volume 2019, Article ID 2981796, 9 pages
https://doi.org/10.1155/2019/2981796

Research Article

Fabrication of Nanoparticle-Stacked 1,1-Diamino-2,2-Dinitroethylene (FOX-7) Microspheres with Increased Thermal Stability

Yuanping Zhang,[1] Conghua Hou,[1] Xinlei Jia,[2] Jinyu Wang,[1] and Yingxin Tan[1]

[1]*School of Environment and Safety Engineering, North University of China, Taiyuan 030051, China*
[2]*Department of Chemical Engineering and Safety, Binzhou University, Binzhou, Shandong 256600, China*

Correspondence should be addressed to Conghua Hou; houconghua@163.com and Yingxin Tan; 13934240901@163.com

Received 22 January 2019; Revised 15 April 2019; Accepted 24 April 2019; Published 14 May 2019

Guest Editor: Jakub Zdarta

Nanoparticle-stacked 1,1-diamino-2,2-dinitroethylene (FOX-7) microspheres were successfully prepared by spray-drying, and rod-shaped FOX-7 was obtained by the solvent/nonsolvent method for comparison. The microstructure features of samples were characterized using scanning electron microscopy (SEM) and powder X-ray diffraction (XRD), and the thermal properties were also investigated by differential scanning calorimetry (DSC). From the SEM analysis, the particle size of the rod-shaped FOX-7 is about 10 μm, whereas FOX-7 microspheres having a particle size ranging from 1 to 5 μm are formed by stacking nanoparticles with size of 100-250 nm. The crystal form of the samples prepared by the two methods did not change. The thermal performance test results showed that the rd-shaped FOX-7 had no significant change compared with the raw FOX-7, while the nanoparticle-stacked FOX-7 microspheres had higher thermal stability.

1. Introduction

With the development of modern weapons and ammunition, there is an increasing demand for the performance of explosives, from the pursuit of high-energy elemental explosives to the high-energy-insensitive new explosives. Therefore, many researchers are committed to developing more powerful, safer, and more environmentally friendly energy materials. 1,1-Diamino-2,2-dinitroethylene, called FOX-7 or DADNE, is a high-energy-insensitive explosive due to the molecular structure of hydrogen bonds within and between molecules [1]. It has aroused the interest of scientific researchers since it was developed in 1998 [2]. A large number of previous studies have shown that FOX-7 has excellent comprehensive performance such as low impact sensitivity and friction sensitivity, high energy density, and detonation velocity and is considered as a substitute for RDX used in the military industry [3–7].

Since energetic materials are metastable materials, nanocrystallization can effectively improve the mechanical sensitivity and reaction rate, thereby improving the safety, energy output level, and damage capacity of the explosive [8–10]. Therefore, more and more researchers are devoting themselves to the preparation of nanoexplosives such as 2,4,6,8,10,12-hexanitro-2,4,6,8,10,12-hexaazawurtzitane (CL-20) [11, 12], 1,3,5,7-tetranitro-1,3,5,7-tetrazocane (HMX) [13, 14], 1,3,5-trinitro-1,3,5-triazinane (RDX) [15], 3-nitro-1,2,4-triazol-3-one (NTO) [16], and 2,6-diamino-3,5-dinitropyrazine-1-oxide (LLM-105) [17] by various methods. Of course, nanosized FOX-7 was also included. In 2010, FOX-7 quasi-three-dimensional (3D) grids of one-dimensional nanostructures were synthesized via a spray-freeze-drying technique by Huang et al. [18]. The results showed that the reduction in the average particle size of the FOX-7 grid structure leads to lower decomposition temperature and higher decomposition rate. Cai et al. [19] prepared a novel FOX-7 nanocrystal by embedding it in mesoporous carbon FDU-15, which demonstrated that FOX-7 nanocrystal sensitivity was closely related to the thermal stability and mechanical stability of FDU-15. Gao et al. [20] successfully

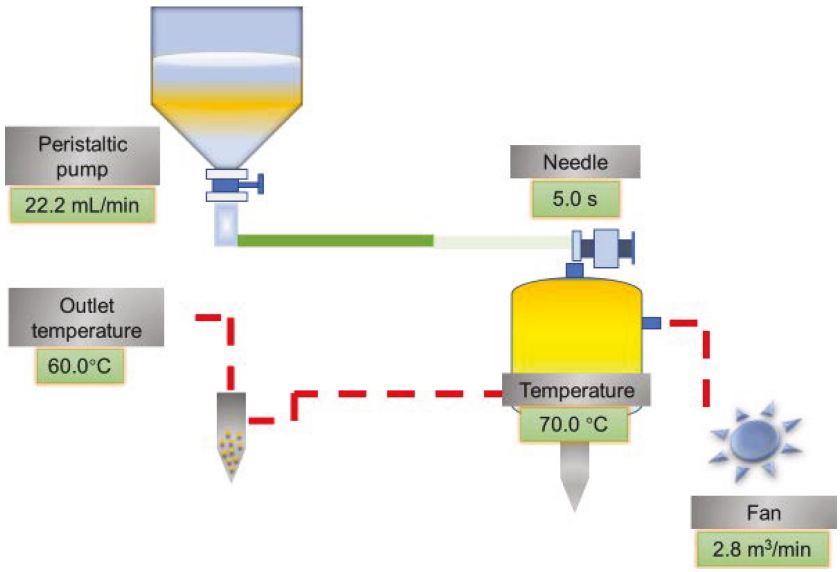

Figure 1: Schematic diagram of the spray-drying device.

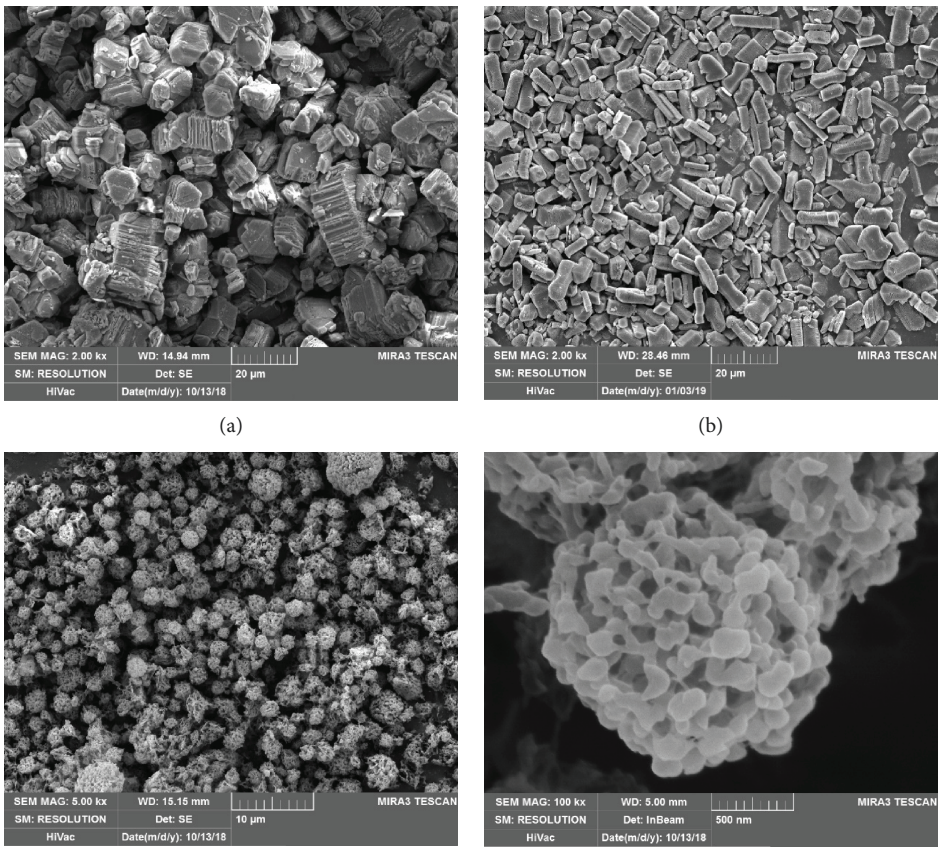

Figure 2: SEM image of raw FOX-7 (a), sample 1 (b), and sample 2 (c, d).

prepared nano-FOX-7 explosive particles by an ultrasonic spray-assisted electrostatic adsorption method in 2014, which has fewer lattice defects and lower internal stress. These explorations implied that the performance of ultrafine FOX-7 has been improved. Therefore, it is of great significance to study the nanosized FOX-7.

Spray-drying is a facile, inexpensive, and scalable technique that has been extensively used in the preparation of microsized spherical material [21]. In this paper, we have prepared nanoparticle-stacked FOX-7 microspheres by spray-drying for the first time. Meanwhile, rod-shaped FOX-7 was obtained by the solvent/nonsolvent method for comparison.

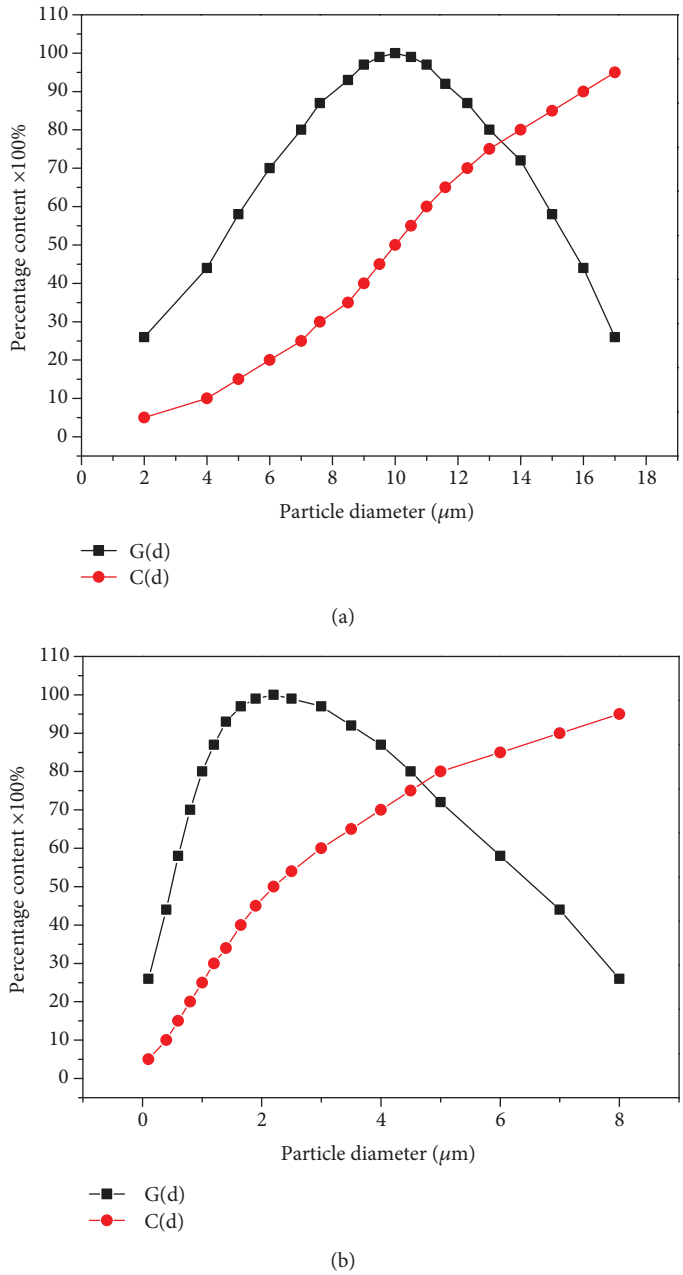

Figure 3: Particle size and size distribution of sample 1 (a) and sample 2 (b).

The crystal morphology, structure, and thermal properties of samples were systematically investigated in detail.

2. Materials and Methods

2.1. Materials. FOX-7, provided by Xi'an Institute of Modern Chemistry, and the purity was higher than 99.5%. Acetone was obtained by Tianjin Tianda Chemical Co. Ltd. (Tianjin city, P.R. China). Pure water was provided by pure water supply of Taiyuan Iron and Steel Co. Ltd.

2.2. Sample Preparation

2.2.1. Preparation of FOX-7 Particles by the Solvent/Nonsolvent Method. About 0.5 g of raw FOX-7 was dissolved completely in 80 mL of acetone (solvent) under ultrasonic dispersion at 40°C and sprayed to 1000 mL water (nonsolvent) under stirring at a certain speed using a spraying device to recrystallize the FOX-7 crystal. After suction filtration and freeze-drying, the target sample is obtained, marked as sample 1.

2.2.2. Preparation of Nanoparticle-Stacked FOX-7 Microspheres by Spray-Dying. In a typical experiment, 0.5 g FOX-7 and 80 mL acetone were added to a 100 mL beaker together. Then, the mixture system was placed in a 45°C water bath and stirred until completely dissolved. Next, the solution was pumped into a small spray-drying chamber at a flow rate of 80 mL/min. The temperatures of inlet and outlet dry gas (N_2) were set as 70°C and 60°C, respectively. The spray gas

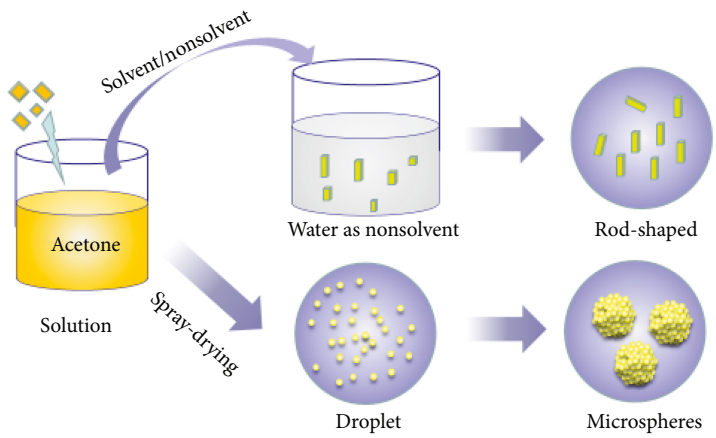

Figure 4: Schematic illustration of the formation of sample 1 and sample 2.

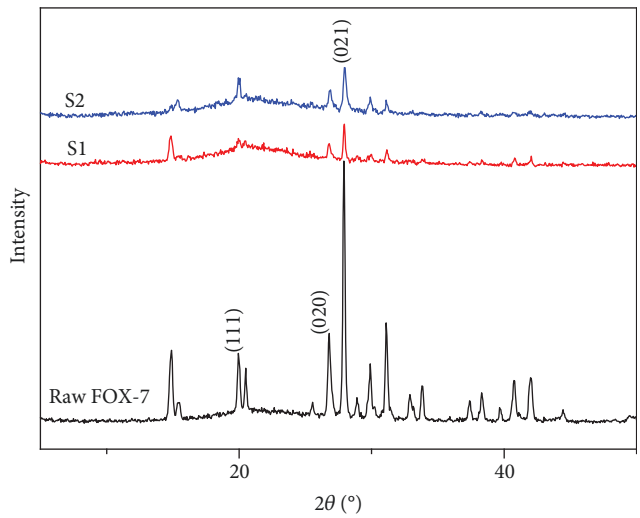

Figure 5: XRD patterns of raw FOX-7, sample 1, and sample 2.

flow rate was 2.8 m^3/min. Finally, the products were separated from the drying gas with a cyclone separator and collected in an electrically grounded glass collection vessel. This product is marked as sample 2. The schematic diagram of the spray-drying device is shown in Figure 1.

2.3. Characterization. The morphology and size distribution of raw FOX-7 and as-prepared FOX-7 particles were examined using a MIRA3 LMH scanning electron microscope (Tescan, Czech Republic). The as-obtained samples were dispersed on conductive carbon adhesive tape to attach to a SEM stub and then gold-coated for SEM investigation. Power X-ray diffraction (Dandong Haoyuan Corporation, Liaoning, China) was used to visualize the changes in the crystal structure of the samples. PXRD patterns were recorded using a Bruker D8 Advance diffractometer at a voltage of 40 kV and a current of 30 mA using Cu Kα radiation at $\lambda = 1.5418$ Å. The thermal properties were characterized by DSC Q20P (TA Instruments). The DSC conditions used are as follows: sample mass: 0.7 mg; heating rate: 5, 10, 15, and 20 K/min; and nitrogen atmosphere under the pressure of 0.1 MPa. The sample size was tested by a QICPIC dynamic particle analyzer (Sympatec Co. Ltd., Germany), and its working environment is 5~35°C, the relative humidity is less than 85%, the light source type is He-Ne laser, the power is 2.0 mW, and the wavelength is 0.6328 μm.

3. Results and Discussion

3.1. Morphologies of the FOX-7 Typical Microspheres. The morphology of raw FOX-7 and as-prepared FOX-7 particles was observed by SEM, as shown in Figure 2. From Figure 2(a), we can see that the raw FOX-7 has an irregular block and has a distinct layered structure, which is consistent with that described in ref. [1]. The particle size distribution is approximately 20 μm, and there are cracks on the surface of the crystal. The FOX-7 samples modified by two methods have obviously improved compared with raw materials. It can be seen from Figure 2(b) that the sample 1 prepared by the solvent/nonsolvent method had a rod-like structure and a large particle size of about 10 μm and the surface defects of the crystal decrease. The microscopic morphology of FOX-7 prepared by the spray-drying method was the submicrosphere having a significantly reduced particle with the

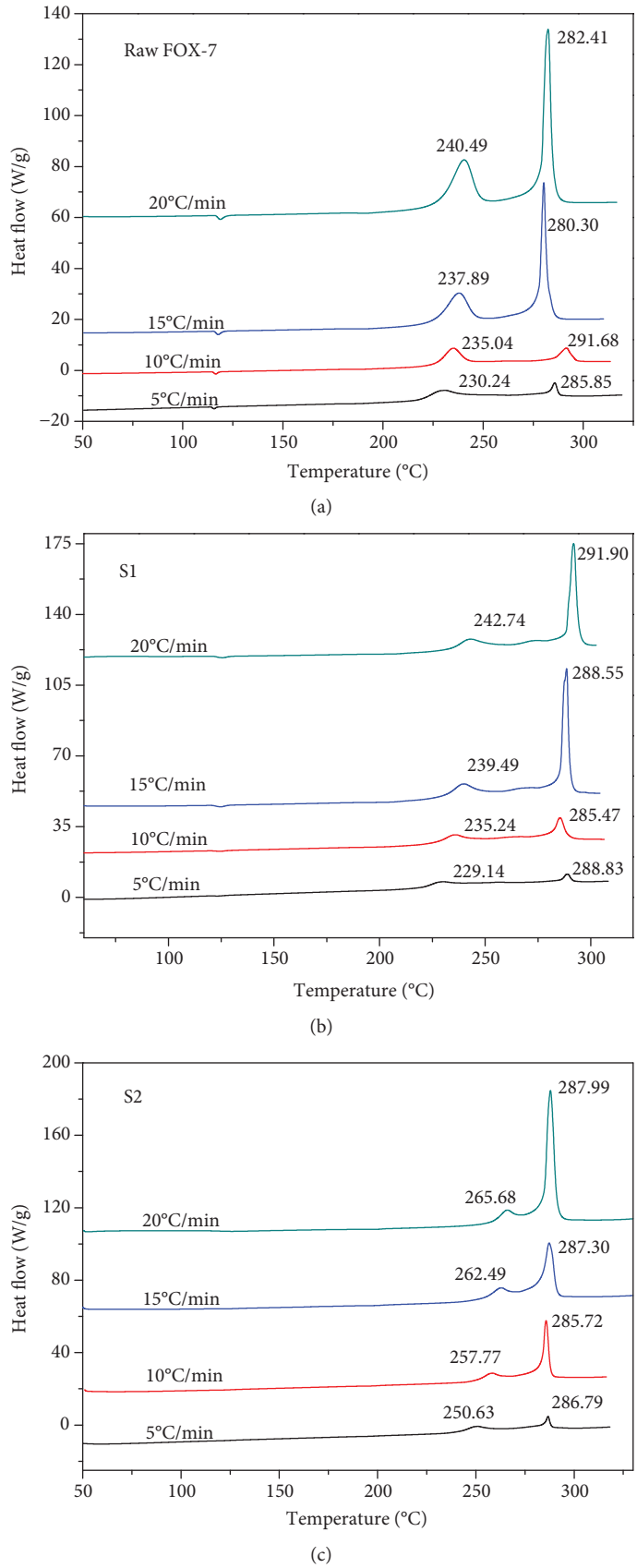

Figure 6: DSC curves of raw FOX-7 (a), sample 1 (b), and sample 2 (c).

Table 1: Thermal decomposition kinetic parameters of samples.

	Kissinger		Ozawa	Starink	Mean activation
	Ea (kJ/mol)	lgA (s^{-1})	Ea (kJ/mol)	Ea (kJ/mol)	energy (kJ/mol)
FOX-7	285.47	29.46	293.92	286.32	288.57
Sample 1	211.14	18.67	219.60	211.99	214.24
Sample 2	206.67	17.27	215.50	207.56	209.91

Table 2: Thermodynamic property data of the samples.

	T_b (°C)	T_p (°C)	$\Delta S^{\neq}$ (J/mol)	$\Delta H^{\neq}$ (kJ/mol)	$\Delta G^{\neq}$ (kJ/mol)
FOX-7	223.24	221.79	306.53	281.36	129.64
Sample 1	221.77	220.34	100.00	207.04	157.69
Sample 2	241.88	240.18	72.87	202.40	165.00

grain diameter ranging from 1 μm to 5 μm. The particle distribution curves of the samples are shown in Figure 3. It is clear that the median particle size of sample 1 and sample 2 are 10 and 2 μm, respectively, confirming the results of the SEM test.

It can be clearly observed from Figure 2(d) that the FOX-7 microspheres are solid microspheres which are formed by stacking small nanoparticles with the grain diameter ranging from 100 nm to 250 nm. It was found that large crystals were obtained after rapid self-assembly. The formation process is explained as follows: the FOX-7 solution is formed into a mist-like droplet by an atomizer and then enters into a drying chamber of a low-pressure hot nitrogen gas, and the droplets are moved to the collecting device under hot air and pressure conditions. As the solvent evaporates rapidly, the tiny droplets become a supersaturated solution. Then, the nanoparticles are formed by rapid nucleation and agglomeration to form microspheres. The schematic illustration of the formation process of sample 1 and sample 2 are shown in Figure 4.

3.2. Crystal Structure of Samples. XRD measurements were carried out to identify the crystalline phase. Figure 5 shows the XRD patterns of raw FOX-7 and samples prepared. The characteristic diffraction peaks (1 1 1), (0 2 0), and (0 2 1) of raw FOX-7 appeared at 2θ of 19.846°, 26.604°, and 27.74°, respectively, as marked in Figure 5. It can be also seen that the characteristic diffraction peaks of sample 1 and sample 2 are consistent with those of the raw FOX-7, indicating that during the two processes of solvent/nonsolvent and spray-drying, the crystal structure did not change and good crystallinity was maintained. The peak intensity of the refined samples becomes weaker due to the decrease in grain size and serious X-ray dispersion.

Based on the Debye-Scherrer equation and diffraction peak at $2\theta = 26.604°$, the average crystalline size was calculated as 26.55 nm.

$$D = \frac{k\lambda}{\beta \cos \theta}, \quad (1)$$

where D is the grain diameter perpendicular to the crystal plane (nm), k is the Scherrer constant (usually 0.89), λ is the incident X-ray wavelength ($\lambda(\mathrm{Cu}) = 0.154059$ nm), β is the peak width of the diffraction peak at half max (rad), and θ is the angle of the diffraction peak.

3.3. Thermal Performance. Thermal stability is a key performance in the field of energetic materials. The thermal performance of raw FOX-7, sample 1, and sample 2 as-prepared were tested using differential scanning calorimetry. The DSC curves of raw FOX-7, sample 1, and sample 2 with the linear heating rate of 5, 10, 15, and 20°C/min were recorded in a nitrogen atmosphere (Figure 6). As can be seen from Figure 6, there are two decomposition exothermic peaks in the DSC curves of raw FOX-7 and FOX-7 as-obtained, indicating that the decomposition process can be divided into two stages. The first stage is the low-temperature decomposition stage, in which two amino hydrogens and one nitro oxygen are removed from the adjacent FOX-7 molecule to form a water molecule, accompanied by the condensation reaction of carbon-carbon double bonds. The second stage is the high-temperature decomposition stage, mainly due to the fracture of carbon skeleton in the FOX-7 molecule [7]. Under the same heating rate, the first decomposition peak temperature of the sample prepared by the solvent/nonsolvent method was delayed by 1-2°C from the peak temperature of the raw material, and that of sample 2 obtained via spray-drying was postponed at about 20°C. It shows that as the particle size decreases, the peak temperature of the low-temperature decomposition is postponed, which is similar to the literature research results [18–20]. This is because the FOX-7 particles are small and the internal stress is also small, and the internal stress generated by the resulting product is insufficient to cause the FOX-7 particles to rupture to form smaller particles [22]. Therefore, the particles begin to decompose when the temperature rises to a certain extent, resulting in a delay in the exothermic peak of the first stage. At different heating rates, the exothermic peak of sample 2 was 285~288°C, and the high-low-temperature liberation heat range was significantly smaller than that of sample 1 and raw materials, indicating that sample 2 was more concentrated in heat release and had higher energy release efficiency. The second decomposition peak temperature of FOX-7 at different heating rates did not move regularly, which was related to the specific thermal decomposition characteristics of FOX-7. It may be due to

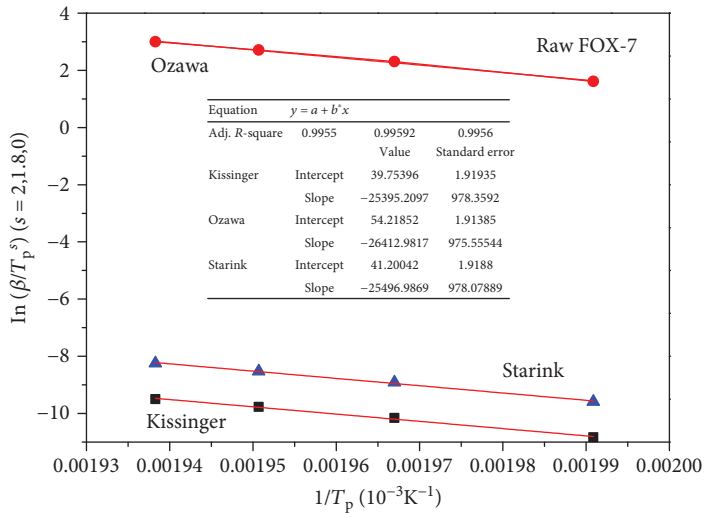

(a)

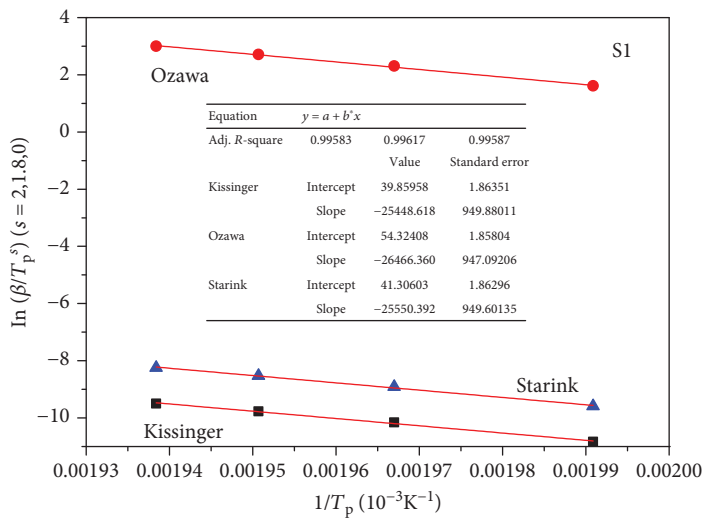

(b)

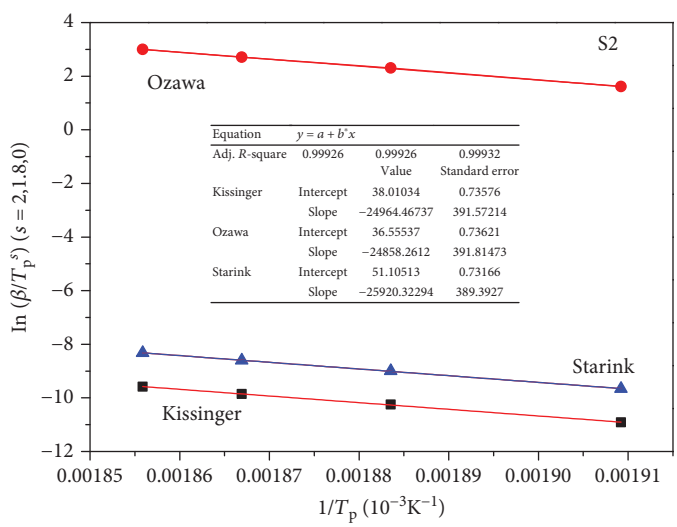

(c)

Figure 7: Reaction kinetics fit curve of the raw material FOX-7 (a) and samples 1 (b) and 2 (c) by the Kissinger method, Ozawa method, and Starink method.

mechanical changes related to thermal redistribution from the second peak to the first peak, or to the thermal runaway, where the sample temperature was much higher than the measured temperature.

Furthermore, in order to evaluate its thermal performance, the kinetic and thermodynamic parameters were further performed. Kissinger's method [23], Flynn-Wall-Ozawa's method [24], and Starink's method [25] were enlisted to calculate the apparent activation energy (E_a) and preexponential factor (A). The calculation process is consistent with that in ref. [26]. The data are shown in Table 1. The critical temperature of thermal explosion (T_b), the value of the peak temperature corresponding to $\beta \to 0$ (T_{p0}), entropy of activation ($\Delta S^{\neq}$), enthalpy of activation ($\Delta H^{\neq}$), and free energy of activation ($\Delta G^{\neq}$) of the samples were then calculated based on formulas 2–6 [27] and are listed in Table 2.

$$T_p = T_{p0} + b\beta_i + c\beta_i^2 + d\beta_i^3, \tag{2}$$

$$T_b = \frac{E_a - \sqrt{E_a^2 - 4RE_aT_{p0}}}{2R}, \tag{3}$$

$$\Delta H^{\neq} = E_k - RT_{p0,} \tag{4}$$

$$A_k \exp\left(\frac{E_k}{RT}\right) = \frac{k_B T_{p0}}{h} \exp\left(-\frac{\Delta G^{\neq}}{RT_{p0}}\right), \tag{5}$$

$$\Delta G^{\neq} = \Delta H^{\neq} - T_{p0}\Delta S^{\neq}, \tag{6}$$

where β_i is the heating rate in °C/min; T_p is the peak temperature in the DSC trace at β_i in K; R is the universal gas constant (8.318 J K^{-1} mol^{-1}); A is the preexponential factor in s^{-1}; E_a is the apparent activation energy in kJ mol^{-1}; k is the rate constant in s^{-1}; T_{p0} is the peak temperature when β_i is zero in K; b, c, and d are constants; T_b is the critical explosion temperature in °C; k_B is Boltzmann constant (1.381×10^{-23} J K^{-1}), h is the Plank constant (6.626×10^{-34} J•s); $\Delta G^{\neq}$ is the free energy of activation in kJ mol^{-1}; $\Delta H^{\neq}$ is the enthalpy of activation in kJ mol^{-1}; and $\Delta S^{\neq}$ is the entropy of activation in J mol^{-1}.

The apparent activation energies of samples 1 and 2 were reduced by 74.33 and 78.66 kJ/mol, respectively, compared to the raw material FOX-7. Figure 7 shows the reaction kinetic fit curve of the raw material FOX-7 and samples 1 and 2 by three methods. It can be found that the linear correlation coefficients of the fitting straight line are greater than 0.99, implying that the measured data is accurate and reliable. The thermal explosion critical temperature of sample 1 was lowered by 1.47°C, while that of sample 2 was increased by 18.64°C, which can be concluded that microsphere FOX-7 had better thermal stability.

4. Conclusion

Herein, the rod-shaped FOX-7 and microspheres FOX-7 were successfully prepared by the solvent/nonsolvent method and spray-drying method, respectively. Surprisingly, microspheres FOX-7 having a particle size ranging from 1 to 5 μm are formed by stacking nanoparticles with size of 100-250 nm, which is obviously smaller than the raw material. In the two processes of preparing samples, the FOX-7 maintains the α-form. From the results of thermal analysis, the similar decomposition process indicates that sample 2 keeps better thermal stability, which may be highly desirable for microenergetic systems.

Data Availability

The data used to support the findings of this study are available from the corresponding author upon request.

Conflicts of Interest

The authors declare that there is no conflict of interest regarding the publication of this paper.

Acknowledgments

This research work was financially supported by the Graduate Education Innovation Project in Shanxi Province (2018BY089) and the 15th Graduate Science and Technology Project of North University of China (20181568).

References

[1] U. Bemm and H. Östmark, "1,1-Diamino-2,2-dinitroethylene: a novel energetic material with infinite layers in two dimensions," *Acta Crystallographica Section C Crystal Structure Communications*, vol. 54, no. 12, pp. 1997–1999, 1998.

[2] N. V. Latypov, J. Bergman, A. Langlet, U. Wellmar, and U. Bemm, "Synthesis and reactions of 1,1-diamino-2,2-dinitroethylene," *Tetrahedron*, vol. 54, no. 38, pp. 11525–11536, 1998.

[3] H. Bergman, H. Östmark, A. Pettersson, M. L. Pettersson, U. Behm, and M. Hihkio, "Some initial properties and thermal stability of FOX-7," in *Insensitive Munitions and Energetic Materials Symposium*, pp. 346–351, National Defense Industrial Association, Tampa, FL, USA, 1999.

[4] H. Ostmark, H. Bergman, U. Bemm et al., "2,2-dinitro-ethene-1,1-diamine (FOX-7)-properties, analysis and scale-up," in *Energetic materials-Ignition, combustion and detonation*, p. 26-1, Karlsruhe, Germany, 2001.

[5] A. K. Burnham, R. K. Weese, R. Wang, Q. M. Kwok, and D. G. Jones, "Thermal properties of FOX-7," in *36th International Annual Conference of ICT & 32nd International Pyrotechnics Seminar*, Karlsruhe, Germany, 2005.

[6] Q. B. Fu, Y. J. Shu, and Y. G. Huang, "Thermal decomposition mechanism of FOX-7," *Journal of Solid Rocket Technology*, vol. 33, no. 1, pp. 77–80, 2010.

[7] D. E. Taylor, F. Rob, B. M. Rice, R. Podeszwa, and K. Szalewicz, "A molecular dynamics study of 1,1-diamino-2,2-dinitroethylene (FOX-7) crystal using a symmetry adapted perturbation theory-based intermolecular force field," *Physical Chemistry Chemical Physics*, vol. 13, no. 37, pp. 16629–16636, 2011.

[8] J. E. Um, T. Yeo, W. Choi, J. S. Chae, H. S. Kim, and W. J. Kim, "Enhanced energy release from homogeneous carbon nanotube-energetic material composites," *Science of Advanced Materials*, vol. 8, no. 1, pp. 164–170, 2016.

[9] N. Zohari, M. H. Keshavarz, and S. A. Seyedsadjadi, "The advantages and shortcomings of using nano-sized energetic materials," *Central European Journal of Energetic Materials*, vol. 10, no. 1, pp. 135–147, 2013.

[10] S. B. Kim, K. J. Kim, M. H. Cho, J. H. Kim, K. T. Kim, and S. H. Kim, "Micro- and nanoscale energetic materials as effective heat energy sources for enhanced gas generators," *ACS Applied Materials & Interfaces*, vol. 8, no. 14, pp. 9405–9412, 2016.

[11] Y. Bayat, M. Zarandi, M. A. Zarei, R. Soleyman, and V. Zeynali, "A novel approach for preparation of CL-20 nanoparticles by microemulsion method," *Journal of Molecular Liquids*, vol. 193, pp. 83–86, 2014.

[12] D. Wang, B. Gao, G. Yang, F. Nie, and H. Huang, "Preparation of Cl-20 explosive nanoparticles and their thermal decomposition property," *Journal of Nanomaterials*, vol. 2016, Article ID 5462097, 7 pages, 2016.

[13] R. Kumar, P. F. Siril, and P. Soni, "Optimized synthesis of HMX nanoparticles using antisolvent precipitation method," *Journal of Energetic Materials*, vol. 33, no. 4, pp. 277–287, 2015.

[14] X. Jia, J. Wang, C. Hou, and Y. Tan, "Green preparation, spheroidal, and superior property of nano-1,3,5,7-tetranittro-1,3,5,7-tetrazocane," *Journal of Nanomaterials*, vol. 2018, Article ID 5839037, 8 pages, 2018.

[15] F. Pessina, F. Schnell, and D. Spitzer, "Tunable continuous production of RDX from microns to nanoscale using polymeric additives," *Chemical Engineering Journal*, vol. 291, pp. 12–19, 2016.

[16] G. Yang, F. Nie, J. Li, Q. Guo, and Z. Qiao, "Preparation and characterization of nano-NTO explosive," *Journal of Energetic Materials*, vol. 25, no. 1, pp. 35–47, 2007.

[17] C. Huang, J. Liu, L. Ding, D. Wang, Z. Yang, and F. Nie, "Facile fabrication of nanoparticles stacked 2,6-diamino-3,5-dinitropyrazine-1-oxide (LLM-105) sub-microspheres via electrospray deposition," *Propellants, Explosives, Pyrotechnics*, vol. 43, no. 2, pp. 188–193, 2018.

[18] B. Huang, Z. Qiao, F. Nie et al., "Fabrication of FOX-7 quasi-three-dimensional grids of one-dimensional nanostructures via a spray freeze-drying technique and size-dependence of thermal properties," *Journal of Hazardous Materials*, vol. 184, no. 1-3, pp. 561–566, 2010.

[19] H. Cai, L. Tian, B. Huang, G. Yang, D. Guan, and H. Huang, "1,1-Diamino-2,2-dintroethene (FOX-7) nanocrystals embedded in mesoporous carbon FDU-15," *Microporous and Mesoporous Materials*, vol. 170, pp. 20–25, 2013.

[20] B. Gao, P. Wu, B. Huang et al., "Preparation and characterization of nano-1,1-diamino-2,2-dinitroethene (FOX-7) explosive," *New Journal of Chemistry*, vol. 38, no. 6, pp. 2334–2341, 2014.

[21] R. Vehring, "Pharmaceutical particle engineering via spray drying," *Pharmaceutical Research*, vol. 25, no. 5, pp. 999–1022, 2008.

[22] E. A. Prodan, "Localization phenomena of topochemical reactions," *Journal of Thermal Analysis*, vol. 29, no. 5, pp. 941–948, 1984.

[23] H. E. Kissinger, "Reaction kinetics in differential thermal analysis," *Analytical Chemistry*, vol. 29, no. 11, pp. 1702–1706, 1957.

[24] T. Ozawa, "A new method of analyzing thermogravimetric data," *Bulletin of the Chemical Society of Japan*, vol. 38, no. 11, pp. 1881–1886, 1965.

[25] P. G. Boswell, "On the calculation of activation energies using a modified Kissinger method," *Journal of Thermal Analysis and Calorimetry*, vol. 18, no. 2, pp. 353–358, 1980.

[26] X. Li, B. Wu, S. Liu, C. An, and J. Wang, "An insensitive booster explosive: DAAF surface-coated with viton A," *Central European Journal of Energetic Materials*, vol. 15, no. 3, pp. 445–455, 2018.

[27] Y. Wang, X. Song, D. Song, L. Liang, C. An, and J. Wang, "Synthesis, thermolysis, and sensitivities of HMX/NC energetic nanocomposites," *Journal of Hazardous Materials*, vol. 312, pp. 73–83, 2016.

Hindawi
Journal of Nanomaterials
Volume 2019, Article ID 2418785, 8 pages
https://doi.org/10.1155/2019/2418785

Research Article

Safed Musli (*Chlorophytum borivilianum* L.) Callus-Mediated Biosynthesis of Silver Nanoparticles and Evaluation of their Antimicrobial Activity and Cytotoxicity against Human Colon Cancer Cells

Fengchang Huang,[1] Yaxin Long,[2] Qingqing Liang,[3] Boregowda Purushotham,[4] Mallappa Kumara Swamy,[4,5] and Yongqing Duan[6]

[1]*Department of Oncology, The First Affiliated Hospital of Kunming Medical University, Kunming, Yunnan 650032, China*
[2]*Department of General Surgery, The First People's Hospital of Yunnan Province, Kunming, Yunnan 650032, China*
[3]*Innoscience Research Sdn Bhd, Jalan USJ 25/1, 47650 Subang Jaya, Selangor, Malaysia*
[4]*East West First Grade College, Department of Biotechnology, Bengaluru 560091, India*
[5]*Department of Crop Science, Faculty of Agriculture, Universiti Putra Malaysia, 43400 Serdang, Selangor, Malaysia*
[6]*Department of Gastrointestinal Surgery, The Second Affiliated Hospital of Kunming Medical University, Kunming, Yunnan 650101, China*

Correspondence should be addressed to Yongqing Duan; 13888967847m0@sina.cn

Received 27 November 2018; Accepted 30 December 2018; Published 13 February 2019

Guest Editor: Teofil Jesionowski

With the advancement of nanobiotechnology, eco-friendly approaches of plant-mediated silver nanomaterial (AgNP) biosynthesis have become more attractive for biomedical applications. The present study is a report of biosynthesizing AgNPs using *Chlorophytum borivilianum* L. (Safed musli) callus extract as a novel source of reducing agent. $AgNO_3$ solution challenged with the methanolic callus extract displayed a change in color from yellow to brown owing to the bioreduction reaction. Further, AgNPs were characterized by using UV–visible spectrophotometry, X-ray Diffraction (XRD), Atomic Force Microscopy (AFM), and Fourier Transform Infrared Spectroscopy (FTIR). UV–vis spectrum revealed the surface plasmon resonance property of AgNPs at around 450 nm. XRD pattern with typical peaks indicated the face-centered cubic nature of silver. AFM analysis confirmed the existence of spherical-shaped and well-dispersed AgNPs having an average size of 52.0 nm. Further, FTIR analysis confirmed the involvement of different phytoconstituents of the callus extract role in the process of bioreduction to form nanoparticles. The AgNPs were more efficient in inhibiting the tested pathogenic microbes, namely, *Pseudomonas aeruginosa*, *Bacillus subtilis*, Methicillin-resistant *Escherichia coli*, *Staphylococcus aureus*, and *Candida albicans* compared to callus extract. The 3-(4,5-dimethylthiazol-2-yl)-2,5-diphenyltetrazolium bromide (MTT) assay confirmed the cytotoxic property of AgNPs against human colon adenocarcinoma cell line (HT-29) in a dose-dependent manner. At higher concentrations of 500 μg/mL AgNPs, the cell viability was observed to be only 7% after 24 hours with IC_{50} value of 254 μg/mL. Therefore, these AgNPs clearly endorse the manifold potential to be used in various biomedical applications in the near future.

1. Introduction

As an emerging field of science in the modern world, nanotechnology has greatly benefited humans. Nanotechnology is aimed at producing and utilizing nanosized materials measuring between 1 and 100 nm [1]. The unique features of nanosized materials make them more attractive for application in various fields, especially for delivering drug molecules, image analysis, as a biomarker, biodetection of macromolecules or pathogens, etc. [2]. Several types of metals are being

used for the synthesis of nanomaterials for specific biomedical applications. They include silver (Ag), gold (Au), titanium dioxide (TiO_2), zinc oxide (ZnO), copper oxide (CuO), magnesium oxide (MgO), calcium oxide (CaO), and silica (Si). These nanostructures exhibit unique physicochemical and biological properties, including strength, plasticity, durability, and functions. Thus, they are widely applied in different areas, including electronics, biomedicine, and bioengineering [3]. As silver possess antimicrobial activity, it is being widely used in the preparation of various antimicrobial agents for the past few years [4, 5]. Today, silver is used to synthesize silver nanoparticles (AgNPs) for different applications in the fields of medicine, food, health care, etc. This is due to the fact that AgNPs with a larger surface area-to-volume ratio possess unique biological, electrical, thermal, and optical properties [6–8].

There are several approaches to synthesize AgNPs, including chemical, physical, and biological methods [3, 9–11]. However, the preferred method is by using the biological route that involves plant compounds or plant extracts, microbes, or their products. This is mainly because of safety, cost-effectiveness, and environment-friendly aspects. On the other hand, chemical and physical methods involve toxic chemicals, a lot of energy, great pressure, and high temperature [6, 9, 12]. AgNPs were successively produced using different plant extracts, such as *Leptadenia reticulata* [9], *Cassia didymobotrya* [10], *Andrographis paniculata* [12], *Prunus japonica* [13], *Talinum triangulare* [14], *Euphorbia antiquorum* [15], *Thymbra spicata* [16], and *Cleome viscosa* [17]. Recently, AgNPs are being synthesized from the plant callus as a novel source. For instance, the callus induced from *Catharanthus roseus*, *Sesuvium portulacastrum*, *Taxus yunnanensis*, *Centella asiatica*, *Cucurbita maxima*, etc., are used for the biosynthesis of AgNPs [4, 18–21]. Advantageously, callus cultures mitigate the problems of wild plant source scarcity. In addition, callus extracts are more efficient in producing more distinct and scattered AgNPs compared to those biosynthesized using leaf extracts with higher bioactivities [4, 21].

Chlorophytum borivilianum L. (Safed musli) is a valued medicinal plant, having copious bioactive components, such as phenols, saponins, flavonoids, alkaloids, tannins, steroids, triterpenoids, and vitamins. The plant is effective in curing chronic leucorrhoea, diabetes, arthritis, high blood pressure, and delayed menopause [22, 23]. To overcome the problems of Safed musli cultivation in the field, plant tissue culture approaches have been adopted to obtain its bioactive compounds. Safed musli callus culture as a reliable source for plant secondary metabolites has been proven previously by Charl et al. [24]. Further, they have also reported the antimicrobial and antioxidant activities of Safed musli callus extract. However, to date there is no report on the biosynthesis of AgNP using Safed musli plant or its callus. Therefore, the present study reports a biological method of synthesizing AgNPs using Safed musli callus extracts to evaluate their biological properties.

2. Materials and Methods

2.1. Preparation of Callus Extracts of Safed Musli. To initiate the callus cultures of Safed musli, the method explained by Nakasha et al. [23] was followed. Briefly, shoot buds of Safed musli were inoculated on solid Murashige and Skoog medium containing 5 mg/L 2,4-dichlorophenoxy acetic acid and cultured for 4 weeks and then harvested. To prepare the callus extract, 20 g fresh weight callus was grinded along with 100 mL of methanol and boiled for about 5 min. By using the Whatman no. 1 filter paper, the extract was filtered and kept at 4°C. The extract was used for AgNP preparation within 1 week.

2.2. Biosynthesis of AgNPs. About 10 mL of callus extracts was challenged with 90 mL of 1 mM $AgNO_3$ (silver nitrate) solution contained in an Erlenmeyer flask (250 mL). The reaction mixture was kept at room temperature on a shaker (150 rpm) without light. The change in color was recorded periodically up to 5 hours, and the AgNPs were stored at room temperature for 3 months to check the stability. The reaction mixture was centrifuged at 20,000 rpm for 15 min to concentrate the biogenically synthesized AgNPs for further characterization.

2.3. Characterization of AgNPs

2.3.1. UV-Visible Spectral Analysis. The change in color formation in the reaction mixture was visually monitored. About 2 mL of the solution was periodically collected after 1, 3, and 5 hours of incubation, and the reduction of silver ions was measured at 300–600 nm UV-visible spectrum using a spectrophotometer (ELICO, India).

2.3.2. X-Ray Diffraction (XRD) Analysis. On the glass slide, a single drop of AgNP solution was added and coated. It was later analyzed to record the crystalline nature of the biosynthesized nanoparticles by using an X-ray diffractometer (XRD), model XRD-6000, Shimadzu, Japan, with 40 kV and 30 mA with Cu ka radiation at 2θ angel.

2.3.3. Atomic Force Microscopy (AFM). Using AFM (A.P.E. Research A100, Italy), AgNPs were characterized to observe their morphological features. At first, the solution containing AgNPs was sonicated at room temperature for 15 min by using an ultrasonicator. Later, the AgNP solution was dried to form a thin layer on a mica-based glass slide, and this was used for observing under AFM.

2.3.4. Fourier Transform Infrared Spectroscopy (FTIR) Analysis. FTIR analysis of biogenically synthesized AgNPs was performed by using a Perkin Elmer FTIR spectrum-using KBr pellet using a Shimazdu IR Prestige-21 FTIR instrument with a diffuse reflecting mode (DRS-8000). All the measurements were carried out in the range of 400–4000 cm^{-1}.

2.4. Antibacterial Activity Evaluation. The biosynthesized AgNPs were assessed for their antimicrobial activity using a disc diffusion method against common human pathogenic Gram-positive bacterial strains, *Bacillus subtilis* B29 (ATCC 29737), Methicillin-resistant *Staphylococcus aureus* (MRSA) (ATCC700698) (Gram-positive), *Pseudomonas aeruginosa* (ATCC 15442), and *Escherichia coli* E266 (Gram-negative), and one fungal species, *Candida albicans*

90028. All microbial strains were procured from the Laboratory of Molecular Biomedicine, Institute of Bioscience, UPM, Serdang, Malaysia. All bacterial strains were maintained on the Mueller-Hinton Agar (MHA) media, while *C. albicans* 90028 was cultured on the potato dextrose agar (PDA) medium. To evaluate antibacterial activities, the disc diffusion assay method was employed with little modifications [24]. Briefly, the pure culture of each microbe was evenly swabbed onto the separate petri plates using sterile cotton swabs. The culture medium was placed with sterile discs (6 mm in diameter) precoated with different concentrations (100, 200, and 300 μg/mL) of AgNPs and the methanolic leaf extract. Dimethyl sulfoxide (DMSO) (10 μg/μL) and gentamycin (10 μg/disc) were used as negative and positive controls, respectively, against all the tested microbes. Each treatment was replicated 5 times, and the experiment was repeated twice. All plates were incubated at 37°C for 24 hours, and the appearance of the zone of inhibition (mm) was recorded with the help of a ruler.

2.5. Evaluation of Cytotoxicity against Colon Cancer Cell Line HT-29. We evaluated the cytotoxic effect of mycogenic AgNPs on colon cancer cell line HT-29 as reported earlier [9]. In brief, the cells were grown on the Dulbecco's Modified Eagle's Medium (DMEM) contained with penicillin (100 U/mL), streptomycin (100 g/mL), L-glutamine (2 mM), and fetal bovine serum (10%). Approximately 5×10^4 cells were used for the inoculation in a well of 96-well plates. A CO_2 incubator adjusted to 37°C was used to incubate the cells for 48 hours. To study the cytotoxicity, the cells were treated with biosynthesized AgNPs (10, 20, 40, 80, 120, and 160 μg/mL) and incubated for 48 hours to evaluate cell survivability using the 3-(4,5-dimethylthiazol-2-yl)-2,5-diphenyltetrazolium bromide (MTT) test. Firstly, fresh MTT solution (5 mg/mL) was prepared and about 10 mL of it was dispensed to each well. Further, it was kept for the incubation up to 4 hours under the same conditions. Using a multiwell ELISA plate reader, the absorbance was documented at 570 nm. The obtained absorbance was transformed into cell viability percentage using the given formula below:

$$\%\ \text{cell viability} = \frac{\text{Values of optical density in the experimental samples}}{\text{Values of optical density in the control samples}} \times 100. \quad (1)$$

2.6. Statistical Analysis. All the experiments were replicated three times and repeated thrice. The data obtained from each experiment was represented as mean ± standard deviation (SD).

3. Results and Discussion

3.1. Callus Formation and Synthesis of AgNPs. Synthesizing AgNPs through the biological route has gained more importance in recent times because of the fact that the biological method yields stable and uniform AgNPs with superior pharmacological significance [8, 10]. The present study involved the use of Safed musli callus extract as a substrate to synthesize AgNPs at room temperature. In this study, yellow-colored friable calli formed after 2 months were harvested (Figure 1).

Apparently, Safed musli calli at this stage are considered as matured and well developed to secrete plant secondary metabolites. Hence, calli harvested after 2 months were utilized in the process of synthesizing AgNPs [23, 24]. In general, the production and features of nanoparticles vary depending on the bioactive compounds occurring in solvent extracts of a plant species [9]. When the $AgNO_3$ solution was challenged with the methanolic callus extract of Safed musli, there was a change in the color from yellow to light brown due to bioreduction reaction (Figure 2). This clearly suggests the biosynthesis of AgNPs, which is correlated to the excitation of surface plasmon resonance vibrations in AgNPs [9, 18, 25]. The color change was immediately observed within an hour, and the intensity of the color increased with the incubation time up to 5 hours. However, more than 5 hours of incubation showed no observable change in the color. The color intensity increased gradually with an increase of incubation time and remained the highest after 5 hours of incubation. Till now, the exact mechanisms involved in the biosynthesis of AgNPs from plant extracts are not clearly understood. However, some possible mechanisms which might be involved in the biosynthesis are being proposed. Accordingly, the cellular enzymes along with the occurrence of diverse classes of phytocompounds, such as phenolics, flavonoids, phytosterols, terpenoids, organic acids, alkaloids, and alcohols, occurring in plant extracts might efficiently reduce forming AgNPs from silver ions [26, 27]. Previously, researchers have reported that the incubation duration for completing the bioreduction of silver ions to form AgNPs varies from one plant species to another due to differences in the occurrence of phytoconstituents in the plant extracts [9, 10].

3.2. Characterization of AgNPs

3.2.1. UV-Visible Spectroscopy Analysis. The use of UV-visible spectroscopy, XRD, AFM, and FTIR analysis has provided the information related to the size, shape, dispersion, and surface area of callus extract-mediated AgNPs. The UV spectrum showed the presence of a sharp absorbance peak at around 450 nm, suggesting the occurrence of AgNPs (Figure 3). According to previous reports, the UV-visible absorption band in between 425 and 460 nm indicates surface plasmon resonance (SPR) of AgNPs [8, 18, 28]. This SPR peak along with the bioreducing agents of the callus extract may possibly be involved in capping to form and stabilize AgNPs [9]. The

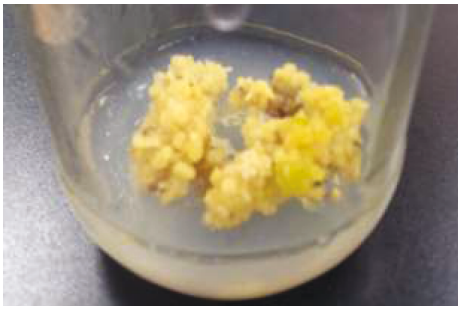

Figure 1: Showing the callus formation on MS medium supplemented with 2,4-D (5 mg/L) after 2 months.

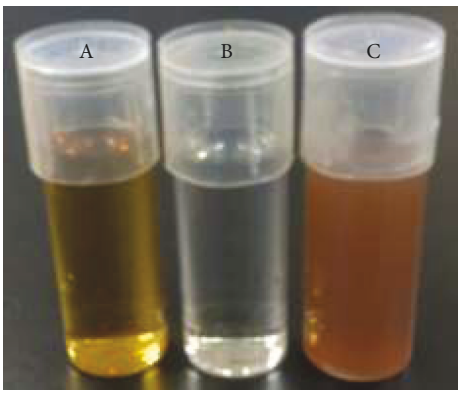

Figure 2: Yellow color of the Safed musli callus extract (A); transparent color of $AgNO_3$ solution (B), and brown color of the reaction mixture after 48 hours of exposure to $AgNO_3$ indicating the formation of AgNPs (C).

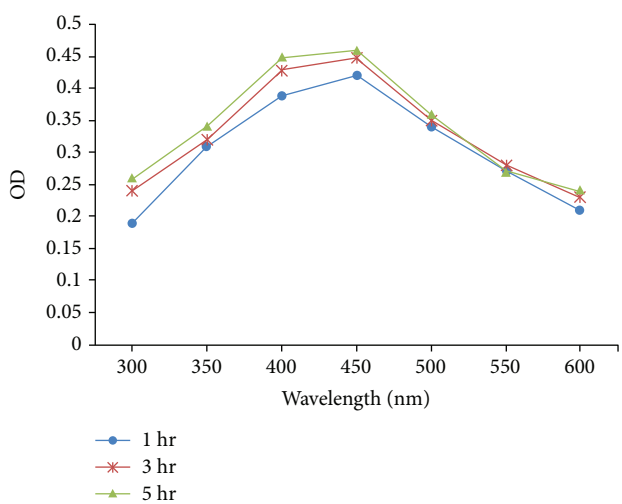

Figure 3: UV–visible absorption spectroscopy showing the characteristic SPR peak of AgNPs.

presence of a broad peak could be correlated to the polydispersal nature of AgNPs with spherical shape [29].

3.2.2. XRD Analysis. The observation of diffraction peaks of XRD analysis provides the details on crystalline nature and

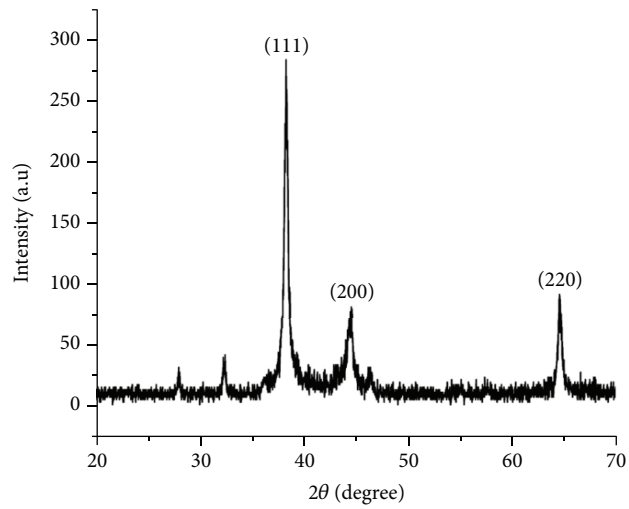

Figure 4: XRD pattern of biosynthesized AgNPs using callus extract of Safed musli.

chemical composition of the biosynthesized AgNPs. The result of the XRD pattern of AgNPs synthesized using Safed musli callus extract is illustrated in Figure 4. The diffracted intensities from 20° to 70° were recorded. The observed peaks at 2θ of 38.34°, 44.54°, and 64.6° correspond to (111), (200), and (220) planes, respectively, of face-centered cubic structure of silver. These results are similar to the record of the Joint Committee on Powder Diffraction Standards (JCPDS no. 04-0783). Likewise, other minor peaks observed might be correlated to the crystalline organic compounds that are adsorbed on the AgNP surface. Similar diffraction patterns were also observed by previous findings related to AgNPs synthesized from plant sources [10, 18, 27].

3.2.3. AFM Analysis. AFM analysis was carried out to record the topological features of biosynthesized AgNPs from callus extract of Safed musli. The result evidently disclosed that the existence of spherically shaped AgNPs is evenly dispersed (Figure 5). The size of the AgNPs ranged between 35.1 and 168.0 nm with an average size of 52.0 nm. The biosynthesized AgNPs were found with a roughness of 7.9 nm and root mean square roughness of 14.6 nm (Figures 5(a) and 5(b)). These observations are in confirmation with the previously reported nanoregime and spherically shaped AgNPs biosynthesized from different plant species, including *Leptadenia reticulata*, *Murraya koenigii*, *Centella asiatica*, *Cleome viscosa*, and *Coptidis rhizoma* [8, 17, 18, 27, 30].

3.2.4. FTIR Analysis. The likely interaction of biosynthesized AgNPs and different phytocompounds occurring in Safed musli callus extract was determined by FTIR analysis. These phytoconstituents are accredited to function as reducing and stabilizing agents during their AgNP biosynthesis [10, 29]. Figure 6 demonstrates the FTIR spectral data of biosynthesized AgNPs with 14 distinct peaks in the range of the 4000–500 cm^{-1} region. A broad peak at 3437.86 cm^{-1} corresponds to the stretching vibrations of –O-H and –N-H groups. Likewise, the peak at 2920.59 cm^{-1} is the result of –

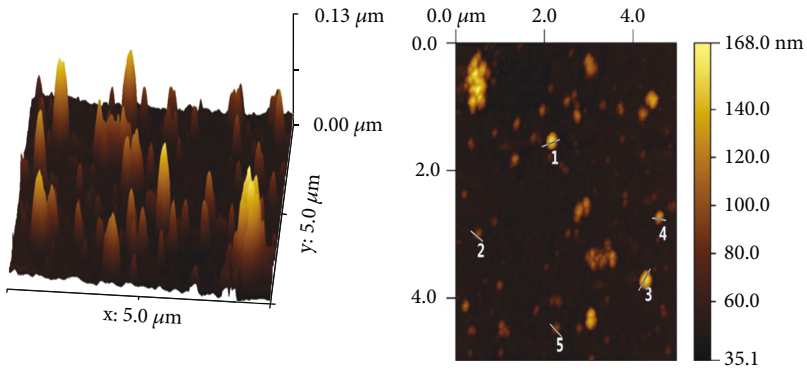

(a) (b)

Figure 5: AFM images of AgNPs biosynthesized by callus extract of Safed musli.

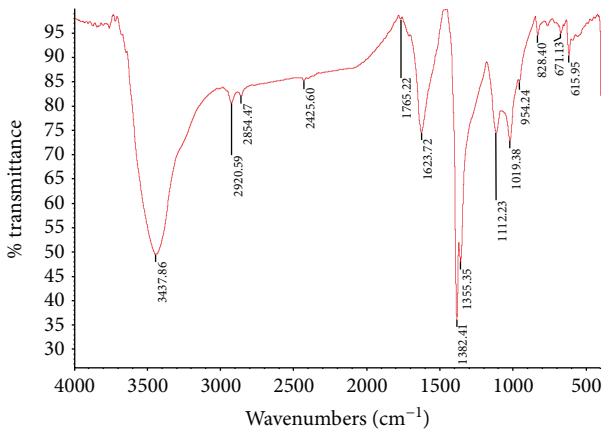

Figure 6: FTIR spectral data of AgNPs produced by callus extract of Safed musli.

C-H groups. The bands at 1623.72 cm^{-1} and 1376 cm^{-1} might be because of the stretching vibrations of C=C groups and the presence of C-N-like amine or C-O-like phenol groups, respectively. The wave number 1382.41 could be assigned to the $-CH_2$ group. The peak at 1019.38 is due to stretching of C=O groups. Three weak bands at 828.4, 671.13, and 615.95 cm^{-1} correspond to bending vibrations of –O-H and C-H groups. Similar observations were made by earlier researchers on other plant-based AgNPs [10, 27, 31]. Further, these absorbance peaks may be endorsed to numerous phytochemical compounds present in the callus extract of Safed musli. In support of this, a previous study by Charl et al. [24] has confirmed the occurrence of different phytoconstituents using gas chromatography–mass spectrometry analysis. Overall, FTIR data shows the multifunctionality of Safed musli callus extract in the process of bioreduction as well as to stabilize AgNPs.

3.3. Assessment of Antibacterial Activity. AgNPs exhibit a broad spectrum antimicrobial activity and, hence, are widely used in clinical applications [5, 7–9]. Nevertheless, their use as antimicrobials will be effective and can be applied only after addressing the problems of their adverse side effects [3]. Hence, we assessed antimicrobial activities of the biosynthesized AgNPs from Safed musli callus extract against human pathogens. It was observed that AgNPs efficiently inhibited all the tested bacterial strains in dose-dependent ways (Table 1). Interestingly, AgNPs exhibited a higher zone of inhibition when compared to the callus extract. The highest inhibition of AgNPs was observed against *C. albicans* (15.83 ± 1.08 mm) followed by *B. subtilis* (14.83 ± 1.60 mm) and *E. coli* (12.60 ± 0.52 mm) at 300 μg/mL concentration. However, all microbes were inhibited by AgNPs at the 300 μg/mL concentration. The maximum inhibitory activity was observed against *B. subtilis* (16.0 ± 1.7) followed by *C. albicans* (15.3 ± 0.5) and *E. coli* (14.3 ± 1.6) at 300 mg/mL concentration of AgNPs. Earlier, investigators have suggested few possible mechanisms of antimicrobial action by plant-based AgNPs. Accordingly, AgNPs denature the cell wall of microbes, destabilize the outer membrane, block cellular respiration, inhibit biosynthesis, and disrupt proton motive force. Also, higher surface area-to-volume ratio of AgNPs is responsible for the antimicrobial activity [3, 7, 8, 14]. The results of the current study clearly indicate that AgNPs synthesized from Safed musli callus extract could be used as antibacterial agents to treat many human diseases.

3.4. AgNPs against Cancer Cells. Additionally, the activity of AgNPs against cancer cell line HT-29 was carried out using the MTT assay. The results of the study are represented in Figure 7. The percentage of cell viability decreased with increased concentrations of AgNPs from 0 to 500 μg/mL. It evidently suggests that AgNPs exhibit dose-dependent cell inhibitory activities. Further, increase in the exposure time from 24 hours to 48 hours decreased the cell viability percentage. After 24 hours, the control treatments recorded 100% cell viability, while only 7% of cells survived at 500 μg/mL of AgNPs, which further decreased to 2% after 72 hours of incubation time. This signifies a high toxicity effect of AgNPs. Although biosynthesized AgNPs exhibit less toxicity at a lower dose, they induce very high lethal effect at higher doses. Similarly, earlier researchers have documented the potential cell inhibitory action of plant-based AgNPs in a dose-dependent manner [3, 8, 32]. The IC_{50} value of AgNPs was calculated to be 254, 216, and 174 μg/mL after 24 hours, 48 hours, and 72 hours, respectively, of treatment.

Table 1: Antimicrobial activities of Safed musli callus extract and its biosynthesized AgNPs against human pathogens.

Concentration (μg/mL)	Zone of inhibition (mm)				
	Bacillus subtilis B29	*Staphylococcus aureus (MRSA)*	*Pseudomonas aeruginosa ATCC 15442*	*Escherichia coli E266*	*Candida albicans 90028*
Callus extract					
100	07.33 ± 0.57	04.66 ± 2.08	04.66 ± 1.52	05.33 ± 0.57	08.00 ± 1.00
200	08.66 ± 0.57	06.00 ± 1.00	08.00 ± 1.15	06.33 ± 0.57	12.00 ± 1.73
300	10.66 ± 1.15	08.66 ± 1.15	09.65 ± 1.52	10.30 ± 1.52	12.66 ± 0.57
AgNPs					
100	09.66 ± 1.15	06.33 ± 0.57	08.16 ± 1.08	07.83 ± 0.76	12.00 ± 2.64
200	12.33 ± 1.57	09.50 ± 1.50	10.00 ± 1.00	12.30 ± 1.53	14.33 ± 1.52
300	14.83 ± 1.60	10.50 ± 1.50	12.00 ± 0.00	12.60 ± 0.52	15.83 ± 1.08

The experiment included DMSO (20 μL) as the negative control, while streptomycin (100 mg/mL) for bacteria and nystatin (100 mg/mL) for yeast served as the positive control. Each value represents the mean ± standard deviation (SD) of 3 replicates per treatment in 3 repeated experiments. Note: "-" represents no activity observed, while "MR" represents Methicillin-resistant.

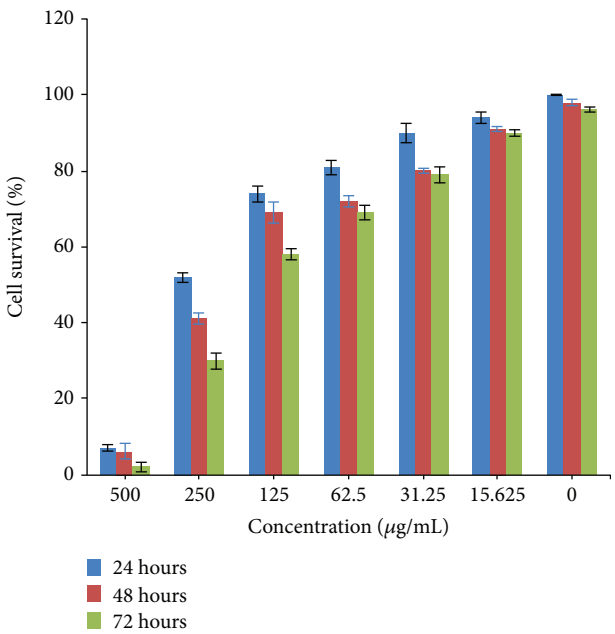

Figure 7: Cytotoxicity results of biosynthesized AgNPs using callus extracts of Safed musli.

In a previous report, it is stated that the Safed musli callus extract possesses various classes of phytochemicals [24]. Thus, phytocompound reactive functional groups, such as hydroxyl, carboxyl, and amino groups, couple with silver ions to exhibit a higher cytotoxicity. Likewise, it is proven that silver ions along with reactive functional groups interact vigorously with the cellular architecture to cause cellular damage [3, 9, 32].

In addition, silver ions possess strong affinity towards sulfhydryl groups of essential enzymes and phosphorus-comprising bases. Hence, AgNPs interact effectively with nucleic acids and cause DNA damage via disrupting the mitochondrial respiratory chain, encouraging reactive oxygen species formation, inhibiting DNA replication and cell division, promoting apoptosis, etc. [3, 32, 33]. Moreover, other characteristics of AgNPs, such as nanoregime nature, spherical shape, and particle surface, also contribute to anticancer properties. Similarly, it has been reported that nanomaterials prepared by using diverse bulk materials have elucidated their cell inhibitory activities against colon cancer cells. Specifically, the anticancer activity was mainly attributed to the chemical composition of the plant extracts and characteristics of nanoparticles, including size and morphological features of AgNPs [9, 33, 34].

4. Conclusion

In conclusion, this study describes an efficient, cost-effective, and environment-friendly approach for biosynthesizing AgNPs using the Safed musli callus extract. The biofabricated AgNPs possess spherical shape with a particle size ranging between 35.1 and 168.0 nm. The XRD pattern established that AgNPs occur in the form of nanocrystals, while AFM observation confirmed the spherical shapes of AgNPs. The FTIR spectrum revealed the occurrence of phytochemicals in the callus extracts and are attributed in the biosynthesis and stabilization of AgNPs. Further, the exhibition of antimicrobial and anticancer activity by the biosynthesized AgNPs suggests that they could be utilized in the fabrication of nanodrugs for therapeutical applications, such as antimicrobial agents, and for the treatment of colon cancers. In total, these findings clearly endorse the manifold potential of these phytofabricated AgNPs.

Data Availability

The data used to support the findings of this study are included within the article.

Conflicts of Interest

The authors declare that there is no conflict of interest regarding the publication of this paper.

References

[1] K. Jemal, B. Sandeep, and S. Pola, "Synthesis, characterization, and evaluation of the antibacterial activity of Allophylus serratus leaf and leaf derived callus extracts mediated silver nanoparticles," *Journal of Nanomaterials*, vol. 2017, Article ID 4213275, 11 pages, 2014.

[2] O. V. Salata, "Applications of nanoparticles in biology and medicine," *Journal of Nanobiotechnology*, vol. 2, no. 1, p. 3, 2004.

[3] G. R. Rudramurthy and M. K. Swamy, "Potential applications of engineered nanoparticles in medicine and biology: an update," *Journal of Biological Inorganic Chemistry*, vol. 23, no. 8, pp. 1185–1204, 2018.

[4] Q. H. Xia, Y. J. Ma, and J. W. Wang, "Biosynthesis of silver nanoparticles using *Taxus yunnanensis* callus and their antibacterial activity and cytotoxicity in human cancer cells," *Nanomaterials*, vol. 6, no. 9, p. 160, 2016.

[5] Ł. Klapiszewski, T. Rzemieniecki, M. Krawczyk et al., "Kraft lignin/silica–AgNPs as a functional material with antibacterial activity," *Colloids and Surfaces B: Biointerfaces*, vol. 134, pp. 220–228, 2015.

[6] X. F. Zhang, Z. G. Liu, W. Shen, and S. Gurunathan, "Silver nanoparticles: synthesis, characterization, properties, applications, and therapeutic approaches," *International Journal of Molecular Sciences*, vol. 17, no. 9, article 1534, 2016.

[7] G. R. Rudramurthy, M. K. Swamy, U. R. Sinniah, and A. Ghasemzadeh, "Nanoparticles: alternatives against drug-resistant pathogenic microbes," *Molecules*, vol. 21, no. 7, p. 836, 2016.

[8] M. K. Swamy, M. S. Akhtar, S. K. Mohanty, and U. R. Sinniah, "Synthesis and characterization of silver nanoparticles using fruit extract of Momordica cymbalaria and assessment of their in vitro antimicrobial, antioxidant and cytotoxicity activities," *Spectrochimica Acta Part A: Molecular and Biomolecular Spectroscopy*, vol. 151, pp. 939–944, 2015.

[9] M. K. Swamy, K. M. Sudipta, K. Jayanta, and S. Balasubramanya, "The green synthesis, characterization, and evaluation of the biological activities of silver nanoparticles synthesized from Leptadenia reticulata leaf extract," *Applied Nanoscience*, vol. 5, no. 1, pp. 73–81, 2015.

[10] M. S. Akhtar, M. K. Swamy, A. Umar, A. Sahli, and A. Abdullah, "Biosynthesis and characterization of silver nanoparticles from methanol leaf extract of Cassia didymobotyra and assessment of their antioxidant and antibacterial activities," *Journal of Nanoscience and Nanotechnology*, vol. 15, no. 12, pp. 9818–9823, 2015.

[11] G. Milczarek, M. Motylenko, A. Modrzejewska-Sikorska et al., "Deposition of silver nanoparticles on organically-modified silica in the presence of lignosulfonate," *RSC Advances*, vol. 4, no. 94, pp. 52476–52484, 2014.

[12] V. S. Kotakadi, S. A. Gaddam, Y. S. Rao, T. Prasad, A. V. Reddy, and D. S. Gopal, "Biofabrication of silver nanoparticles using *Andrographis paniculata*," *European Journal of Medicinal Chemistry*, vol. 73, pp. 135–140, 2014.

[13] A. Saravanakumar, M. M. Peng, M. Ganesh, J. Jayaprakash, M. Mohankumar, and H. T. Jang, "Low-cost and eco-friendly green synthesis of silver nanoparticles using Prunus japonica (Rosaceae) leaf extract and their antibacterial, antioxidant properties," *Artificial Cells, Nanomedicine, and Biotechnology*, vol. 45, no. 6, pp. 1165–1171, 2017.

[14] O. A. Ojo, B. E. Oyinloye, A. B. Ojo et al., "Green synthesis of silver nanoparticles (AgNPs) using Talinum triangulare (Jacq.) Willd. leaf extract and monitoring their antimicrobial activity," *Journal of Bionanoscience*, vol. 11, no. 4, pp. 292–296, 2017.

[15] C. Rajkuberan, S. Prabukumar, G. Sathishkumar, A. Wilson, K. Ravindran, and S. Sivaramakrishnan, "Facile synthesis of silver nanoparticles using Euphorbia antiquorum L. latex extract and evaluation of their biomedical perspectives as anticancer agents," *Journal of Saudi Chemical Society*, vol. 21, no. 8, pp. 911–919, 2017.

[16] H. Veisi, S. Azizi, and P. Mohammadi, "Green synthesis of the silver nanoparticles mediated by Thymbra spicata extract and its application as a heterogeneous and recyclable nanocatalyst for catalytic reduction of a variety of dyes in water," *Journal of Cleaner Production*, vol. 170, pp. 1536–1543, 2018.

[17] G. Lakshmanan, A. Sathiyaseelan, P. Kalaichelvan, and K. Murugesan, "Plant-mediated synthesis of silver nanoparticles using fruit extract of *Cleome viscosa* L.: assessment of their antibacterial and anticancer activity," *Karbala International Journal of Modern Science*, vol. 4, no. 1, pp. 61–68, 2018.

[18] V. R. Netala, V. S. Kotakadi, V. Nagam, P. Bobbu, S. B. Ghosh, and V. Tartte, "First report of biomimetic synthesis of silver nanoparticles using aqueous callus extract of Centella asiatica and their antimicrobial activity," *Applied Nanoscience*, vol. 5, no. 7, pp. 801–807, 2015.

[19] R. I. Iyer and T. Panda, "Biosynthesis of gold and silver nanoparticles using extracts of callus cultures of pumpkin (Cucurbita maxima)," *Journal of Nanoscience and Nanotechnology*, vol. 18, no. 8, pp. 5341–5353, 2018.

[20] D. A. Osibe, N. V. Chiejina, K. Ogawa, and H. Aoyagi, "Stable antibacterial silver nanoparticles produced with seed-derived callus extract of *Catharanthus roseus*," *Artificial Cells, Nanomedicine, and Biotechnology*, vol. 46, no. 6, pp. 1266–1273, 2018.

[21] M. A. Barkat, M. Mujeeb, M. Samim, and S. Verma, "Biosynthesis of silver nanoparticles using callus extract of *Catharanthus roseus* var. alba and assessment of its antimicrobial activity," *British Journal of Pharmaceutical Research*, vol. 4, no. 13, article 1591, 1603 pages, 2014.

[22] J. J. Nakasha, U. R. Sinniah, A. B. Puteh, and M. Kumara Swamy, "Influence of tuber weight and cutting on growth and yield of safed musli (*Chlorophytum borivilianum*)," *Archives of Agronomy and Soil Science*, vol. 63, no. 5, pp. 619–625, 2017.

[23] J. J. Nakasha, U. R. Sinniah, N. Kemat, and K. S. Mallappa, "Induction, subculture cycle, and regeneration of callus in safed musli (*Chlorophytum borivilianum*) using different types of phytohormones," *Pharmacognosy Magazine*, vol. 12, no. 47, Supplement 4, pp. 460–S464, 2016.

[24] R. K. Charl, M. K. Swamy, and U. R. Sinniah, "Antimicrobial properties of safed musli (*Chlorophytum borivilianum*) callus extract and GC-MS based chemical profiling," *Bangladesh Journal of Botany*, vol. 46, no. 1, pp. 205–310, 2017.

[25] J. M. Ashraf, M. A. Ansari, H. M. Khan, M. A. Alzohairy, and I. Choi, "Green synthesis of silver nanoparticles and characterization of their inhibitory effects on AGEs formation using biophysical techniques," *Scientific Reports*, vol. 6, no. 1, article 20414, 2016.

[26] S. Iravani, H. Korbekandi, S. V. Mirmohammadi, and B. Zolfaghari, "Synthesis of silver nanoparticles: chemical,

physical and biological methods," *Research in Pharmaceutical Sciences*, vol. 9, no. 6, p. 385, 2014.

[27] G. Sharma, J.-S. Nam, A. Sharma, and S.-S. Lee, "Antimicrobial potential of silver nanoparticles synthesized using medicinal herb *Coptidis rhizome*," *Molecules*, vol. 23, no. 9, article 2268, 2018.

[28] K. Mallikarjuna, G. Narasimha, G. Dillip et al., "Green synthesis of silver nanoparticles using *Ocimum* leaf extract and their characterization," *Digest Journal of Nanomaterials and Biostructures*, vol. 6, no. 1, pp. 181–186, 2011.

[29] K. Jyoti, M. Baunthiyal, and A. Singh, "Characterization of silver nanoparticles synthesized using Urtica dioica Linn. leaves and their synergistic effects with antibiotics," *Journal of Radiation Research and Applied Sciences*, vol. 9, no. 3, pp. 217–227, 2016.

[30] S. Bonde, D. Rathod, A. Ingle, R. Ade, A. Gade, and M. Rai, "Murraya koenigii-mediated synthesis of silver nanoparticles and its activity against three human pathogenic bacteria," *Nanoscience Methods*, vol. 1, no. 1, pp. 25–36, 2012.

[31] K. Niraimathi, V. Sudha, R. Lavanya, and P. Brindha, "Biosynthesis of silver nanoparticles using *Alternanthera sessilis* (Linn.) extract and their antimicrobial, antioxidant activities," *Colloids and Surfaces B: Biointerfaces*, vol. 102, pp. 288–291, 2013.

[32] S. Salehi, S. A. S. Shandiz, F. Ghanbar, M. R. Darvish, A. Mirzaie, and M. Jafari, "Phytosynthesis of silver nanoparticles using *Artemisia marschalliana* Sprengel aerial part extract and assessment of their antioxidant, anticancer, and antibacterial properties," *International Journal of Nanomedicine*, vol. 11, pp. 1835–1846, 2016.

[33] I.-M. Chung, I. Park, K. Seung-Hyun, M. Thiruvengadam, and G. Rajakumar, "Plant-mediated synthesis of silver nanoparticles: their characteristic properties and therapeutic applications," *Nanoscale Research Letters*, vol. 11, no. 1, p. 40, 2016.

[34] M. S. AlSalhi, S. Devanesan, A. A. Alfuraydi et al., "Green synthesis of silver nanoparticles using *Pimpinella anisum* seeds: antimicrobial activity and cytotoxicity on human neonatal skin stromal cells and colon cancer cells," *International Journal of Nanomedicine*, vol. 11, pp. 4439–4449, 2016.